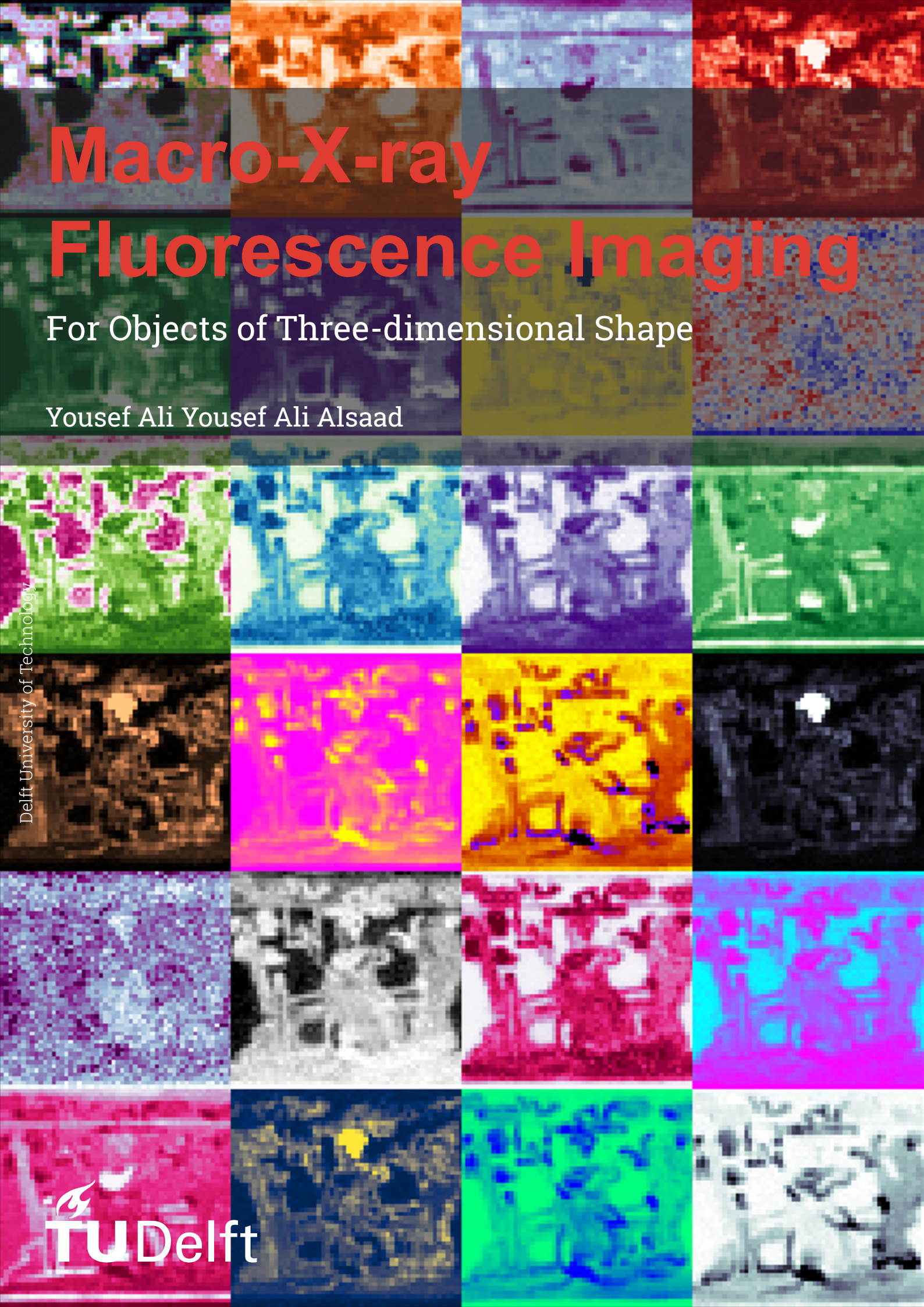

Macro-X-ray Fluorescence Imaging

For Objects of Three-dimensional Shape

Yousef Ali Yousef Ali Alsaad

Delft University of Technology

TU Delft

Macro-X-ray Fluorescence Imaging

For Objects of Three-dimensional Shape

by

Yousef Ali Yousef Ali Alsaad

"Macro X-ray fluorescence (MA-XRF) is widely used for investigations in cultural heritage, yet measurements of curved objects remain prone to geometric artefacts. This thesis investigates the effects of working distance and surface tilt on MA-XRF imaging and evaluates different scan strategies of a curved object. A custom instrument was assembled using motorised linear stages to scan a cylindrical-shaped decorative mug using four modes: 2D, 2D with a fixed offset, 3D utilising three degrees of freedom, and 3D using a rotating stage and one motorised stage. Processing and fitting of data produced spectral and elemental maps, allowing for the qualitative comparison of the scanning modes. Scans of the same areas differed in spectral fidelity and count behaviour, showcasing the influence of detection geometry on the MA-XRF acquisitions. Overall, scans adhering to the object curvature have substantially improved spatial fidelity and signal robustness in the imaging, showcasing the practicality of the solution."

Supervisor:	Dr. Alfeld, M
Project Duration:	March 2025 – October 2025
Faculty:	Mechanical Engineering
Department:	Materials Science and Engineering

TU Delft

Contents

1

Introduction

X-ray fluorescence spectrometry (XRF) has been established as a rapid, non-invasive, and versatile atomic technique for qualitative and quantitative elemental analysis of materials. XRF can be used to characterise the thickness and composition of samples in various forms, including solids, liquids, and powders. Not only is this technique fast and accurate, but it is also non-destructive and requires little to no sample preparation. XRF is used in various industries and fields, including geology [1], mineralogy [2], environmental analysis [3], medicine [4], and material research [5].

In recent years, Macro XRF (MA-XRF) has become a vital tool in cultural heritage studies; the technique has been used in studies of cultural objects such as paintings [6], manuscripts [7] and ceramics [8]. Modern MA-XRF techniques have enabled the creation of detailed elemental distributions across surfaces of cultural objects. These spectral images can reveal hidden features, showcase material compositions, and support conservation efforts for heritage items. Despite the successes of MA-XRF, the influence of sample geometry on MA-XRF measurements remains generally unaccounted for, especially when performing two-dimensional imaging. A sample's curved surface yields variations in signal intensities due to inconsistent working distances and tilt, which can complicate both qualitative and quantitative analysis. Previous studies have addressed this issue using a variety of experimental approaches.

The proposed solutions to the geometric problem in MA-XRF imaging vary in applicability, with some requiring a thorough understanding of the detection parameters in one's instrument to perform fundamental simulations, and others being prohibitively costly. A relatively cheap and straightforward working solution is demonstrated in this thesis in the form of three linear stage motors, whose purpose is to follow an object's curvature during MA-XRF scanning, maintaining a fixed working distance. The effect of surface tilt is addressed by rotating the curved objects during the scanning process. Tasks in this project involve developing the instrument, testing its capability to acquire MA-XRF scans of curved objects, and evaluating its effectiveness in mitigating geometric spectral artefacts.

2

Literature Review

The literature review will cover the topic of Macro X-ray Fluorescence (MA-XRF) applications for three-dimensional objects within the scope of cultural heritage. The review aims to establish an understanding of the theoretical principles, standard instrumentation, and data processing methods used in this technique, demonstrating the working pipeline from acquiring surface scans to converting spectral data into interpretable maps of elemental distribution. Elemental studies of cultural objects are showcased, with an emphasis on the effect of sample geometry on MA-XRF measurements and spectral maps. Finally, the current efforts in research to develop scanning methods for three-dimensional objects are highlighted. The purpose of this review is to review current knowledge in the field and identify the research opportunities for improving methods of MA-XRF imaging for 3D objects.

2.1. X-Ray Fluorescence (XRF) Theory

2.1.1. Characteristic Fluorescent Radiation

The principle of XRF relies on the underlying interactions of X-rays with matter. When X-rays strike matter, three main interactions occur: The photoelectric effect, Compton Scatter, and Rayleigh Scatter. When X-ray photons in a beam are directed towards a slab of material, a fraction of Xray is transmitted through, a fraction is absorbed (producing fluorescent radiation), and a fraction scatters back. Compton scatter refers to the scatter occurring with energy loss, and Rayliegh scatter refers to the scatter occurring without energy loss. The photoelectric effect and scatter are directly dependent on the material's thickness, density, and composition, as well as on the energy of incoming X-rays. In a classical atomic model, the nucleus is surrounded by electrons grouped in distinct shells or orbitals. The inner shells are called K-shells, then moving outwards, L-shells, M-shells, etc. Shell may contain subshells; for example, L-shells contain three sub-shells (L_1, L_2, and L_3), and M-shells contain five sub-shells (M_1, M_2, M_3, M_4, M_5). Each shell contains a known number of electrons, and the energy of each electron depends on the shell it occupies and the element it belongs to. Therefore, when an atom

is irradiated with X-ray photons at sufficient energies, the electron can be expelled from the atom, as shown in Figure 2.a, where an X-ray photon expels an electron from the K-shell. In this instance, a 'hole' in the shell is produced, leaving the atom in an unstable, excited state. Due to a higher energy state, the atom restores the original configuration by transferring an electron from an outer shell to the hole in the K-shell. Since outer shells contain less binding energy and are at higher energy when transferred to an inner shell, they emit the energy surplus as an X-ray photon with a distinct energy. In an XRF spectrum, this is seen as an energy line.

The energy of the emitted X-ray depends on the shell-transfer difference in energy and the energy of the electron that fills the hole. Since each element's atoms have specific energy level configurations, the emitted radiation is characteristic of that atom. An atom may emit more than a single energy (or lines) due to the possibility of different holes and different electrons filling these holes. The collection of emitted energies (or lines) from an element can be defined as its fingerprint, allowing its determination by looking at the acquired X-ray spectrum. The energy of the incoming X-ray is detrimental to the expelling process; if an electron is expelled, the incoming radiation is absorbed, and higher absorption produces higher fluorescence. However, if the energy level is too high, the X-ray photons will transmit through the atom, and only a few electrons will be expelled. Figure 2.b showcases the relation between the energy of the incoming X-ray particles and the consequent absorption. For higher X-ray energies, less absorption occurs, and less fluorescence is created. For instance, lower energies close to the binding energy of the K-shell electrons lead to more radiation absorbed, indicated by higher fluorescence, the closer the energy is to the K-edge. Once the X-ray energy is lower than the binding energy of the K-shell, an edge can be seen where the energy is too low to expel electrons from the K-shell and too high to interact with lower energetic shells, such as the L-shell.

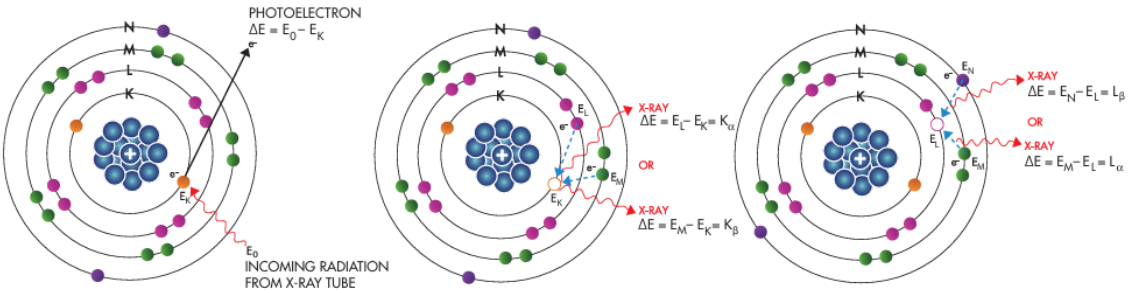

Figure 2.a: Diagram of the XRF process. Left: incoming X-rays remove an electron from the inner shell, creating a hole. Centre: L- and M-shell electrons fill the hole in the K-shell. Excess energies emit characteristic fluorescent X-rays. Holes are made in L and M shells. Right: M- or N-shell electrons fill the holes in the L shell, leading to L-fluorescent emission lines [9].

The naming of characteristic lines in XRF is related to the many transition pathways that occur when an element is irradiated. In an example where a hole is created in the K-shell, the L-shell electron filling it leaves behind a hole, which an M-shell electron may then fill. For each instance of electron transition, an X-ray photon is emitted, and several emission lines are detected. The Siegbahn notation is used to track and describe the nature of the emission for

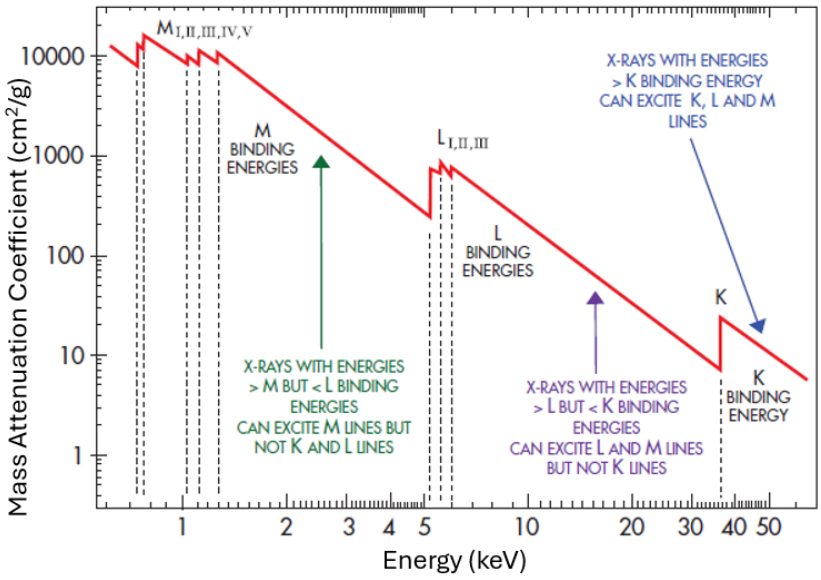

Figure 2.b: Mass attenuation coefficient (MAC) graph for Barium (B=56) [9].

each electron. The primary designation of an X-ray line is the shell being filled (e.g K, L, M) is, followed by the secondary designation (e.g α, β) referring to the specific transition. A transition from an L-shell electron to fill a K-shell hole produces line K_α, while a transition of an M-shell electron to fill a K-shell hole. Due to the sub-orbitals in L and M shells, the notation is not as straightforward as for K series lines. Table 2.a describes the notation corresponding to K, L, and M series emission lines. Due to quantum mechanics, not all transitions are possible, such as the transition from the L_1 orbital to the K-shell. Since a series of lines represents multiple possible transitions to fill a hole in a given shell, all lines will occur if any emission line occurs.

K Series		**L Series**		**M Series**	
Siegbahn	Transition	Siegbahn	Transition	Siegbahn	Transition
$K_{\alpha_{1,2}}$	$L_{2,3}$-K	L_{α_1}	M_5-L_3	$M_{\alpha_{1,2}}$	$N_{6,7}$-M_5
K_{α_1}	L_3-K	L_{α_2}	M_4-L_3	M_β	N_6-M_4
K_{α_2}	L_2-K	L_{β_1}	M_4-L_2		
K_{β_1}	M_3-K	L_{β_2}	N_5-L_3		
$K_{\beta_{1,3}}$	$M_{2,3}$-K	L_{γ_1}	N_4-L_2		
$K_{\beta_{2,4}}$	$N_{2,3}$-K	L_η	M_1-L_2		
		L_ℓ	M_1-L_3		

Table 2.a: X-ray Emission Lines labelling and their Siegbahn Notation [10]

It is important to note that not all transitions produce X-rays of the same intensity; the K series lines usually make the strongest intensities, with subsequent shells producing weaker intensities. Many other factors influence the intensity of an XRF line. For instance, an alternative de-excitation mechanism, referred to as the Auger electron process, may occur. In this case, the electron filling the hole does not emit a corresponding X-ray photon but instead trans-

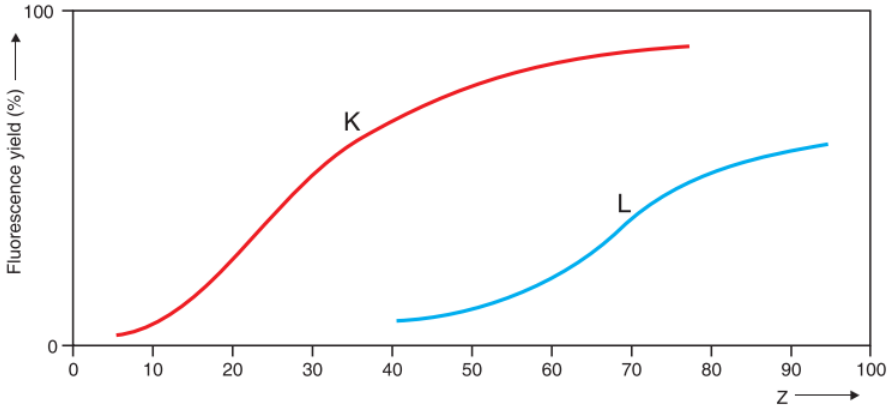

Figure 2.c: Fluorescence yield as a function of atomic number Z. Lighter elements are more susceptible to the Auger effect due to low binding energies. Therefore, fewer X-rays are emitted [11].

fers the excess energy to another electron from the same or a higher shell, which is then itself ejected from the atom. These secondary electrons are known as Auger electrons and do not emit radiation. This process is more relevant for elements with low atomic numbers (Low-Z), where the Auger process is more likely than X-ray emission due to lower binding energies and higher probability of energy transfer to electrons than X-ray photon emission. As a result, less characteristic X-rays are emitted and detected for lighter elements, as shown on Figure 2.c. Characteristic lines appear stronger with increasing atomic number Z, as shown in Figure 2.d. The Figure showcases the most intense line from each series, but generally, it can be seen that energy levels are directly correlated with atomic numbers. For instance, Kα for As (Z=33) appears at 10.543 keV, almost equal to the Lα line of Pb (Z=82) at 10.549 keV.

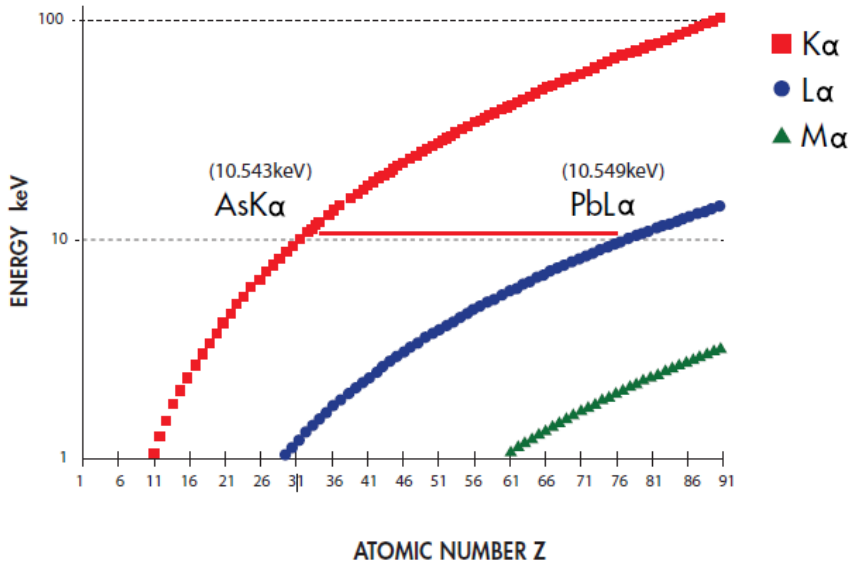

Figure 2.d: Graph of highest K, L, and M energies as a function of atomic number Z. A notable line is As's Kα, which overlap with Pb's Lα line at nearly the same energy [9].

2.1.2. Material Effects

Absorption & Enhancement

X-rays are absorbed in a sample during the XRF process in several ways. As mentioned previously, the atoms absorb part of the incoming X-rays and eject electrons, initiating the fluorescence emission process. These produced fluorescent X-rays may also be absorbed by neighbouring atoms, initiating the photoelectric process. Thus, as fluorescent X-rays pass through the sample to reach the detector, some are absorbed in their path. Therefore, the amount of secondary absorption is related to the material's properties through which the X-rays are passing. The absorption can be described mathematically by the following relationship:

$$I = I_0 e^{-\mu \cdot \rho \cdot t} \tag{2.1.1}$$

Where I is the measured intensity, I_0 is the incident intensity, μ/ρ is the mass attenuation coefficient in cm^2/g, and ρ is the density of the absorbing material in g/cm^3, and t is the thickness in cm. μ/ρ, the mass attenuation coefficient or the mass absorption coefficient, is a crucial paramater to describe the absorption of X-rays by atoms. MAC is directly related to the density of the atom (i.e the atomic number Z) and the energy of the absorbed X-rays; n increase in X-ray energy leads to a decrease in μ/ρ (or the subsequent absorption) for any element. Another specific example is shown in Figure 2.b, where the μ/ρ of barium (Ba, Z=56) is plotted against X-ray energy. The sharp discontinuities, referred to as absorption edges, are abrupt as they define the separation in energy levels of the electron shells. The K-shell edge is at the highest energy since K-shell electrons are the most tightly bound to the atom and require more energy to remove than L- and M-shell electrons. In the case of Ba, 37.4 keV is needed to unbind K-shell electrons, 6.0 keV for L-shell electrons, and 1.2 keV for M-shells. Therefore, characteristic fluorescent X-rays of the element should ideally be produced with X-rays containing energies higher than the absorption edge for each shell of the analyte. The most efficient approach is to use X-rays, which have energies slightly higher than the absorption edges. Although it is theoretically possible to determine the ideal energy to excite each specific shell of an element, typical X-ray tubes produce a wide range of energies to excite all possible shells.

Absorption edges aid in understanding and predicting inter-element matrix effects; if the energy of the primary fluorescence produced by an element in the sample is higher than the absorption edge of the second element present in the matrix, then the second element's electrons are excited. An example of this is shown in Figure 2.e, where a stainless steel sample contains Cr, Fe, and Ni. The K-shell absorption edges are at 6.0, 7.1, and 8.3 keV, respectively, and each element produces characteristic peaks corresponding to their Kα at 5.4, 6.4, and 7.5 keV. When excited, Ni Kα 's X-ray photon may be absorbed by the Fe-atom since its energy is higher than Fe's K-shell absorption edge. This leads to secondary fluorescence from X-rays produced internally, and the detector then measures more Fe Kα photons than usual. Consequently, the measured peak corresponding to Ni Kα will appear smaller than expected. Due to this matrix effect, the measured intensities of X-ray peaks will not accurately reflect the rel-

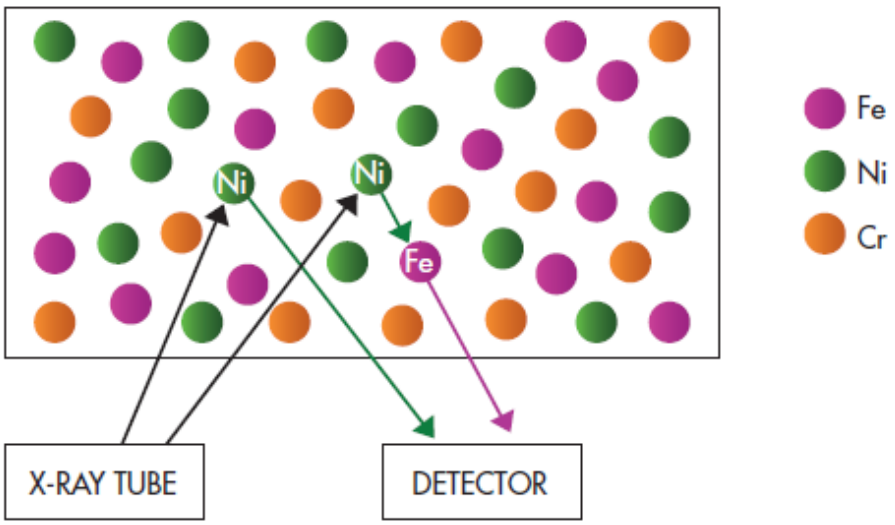

Figure 2.e: Diagram illustrating matrix effect during XRF process. Fluorescent radiation from Ni contains any energy higher than Fe's K edge, leading to excitation in Fe, characterised by secondary fluorescent radiation [9].

ative elemental quantities in the sample, since secondary fluorescence 'enhances' the signal of some elements. These matrix effects can be accounted for when predicting and correcting obtained XRF spectra [12]. In any case, they are of concern only if quantifying the amount of elements is of interest.

Sample Layering & Thickness

An important consideration when studying non-homogenous samples is the effect of layer thickness and depth distribution of materials. While XRF generally gathers surface information of samples (due to the low energy of characteristic radiation), methods have been established to examine complex layer compositions to determine the homogeneity (or non-homogeneity) of samples. One method involves tilting the sample to the X-ray beam axis and measuring at different angles. As the tilt increases, beam penetration becomes deeper, and the volume of excitation encompasses a greater portion of the bulk material. In layered samples, the ratio of responses from the individual layers changes, allowing for the analysis of layer thickness, composition, or contamination [13]. The simplicity of this method is only suitable for straightforward layered structures, providing qualitative analysis. Without modelling the XRF system, exact depth profiles cannot be obtained. Another method relies on the use of the Kα/Kβ (or Lα/Lβ) ratio to obtain depth information [14]; for instance, lower-energy lines (Kα) are more attenuated than higher-energy lines (Kβ) in deeper layers, affecting the Kα/Kβ ratio. This method works well for elements in district layers and is heavily influenced by the matrix effect & self-absorption.

A more robust depth-resolved analysis method is Confocal XRF. In this case, the focused X-ray optics isolate a small, defined volume inside the sample. The confocal volume (shown in Fig 2.f is comprised of the overlap of the incident X-ray beam and the fluorescence detection beam, guided by the optics from the X-ray source and detector. Since only X-rays from the confocal volume are detected, the confocal point can be moved deeper to obtain measure-

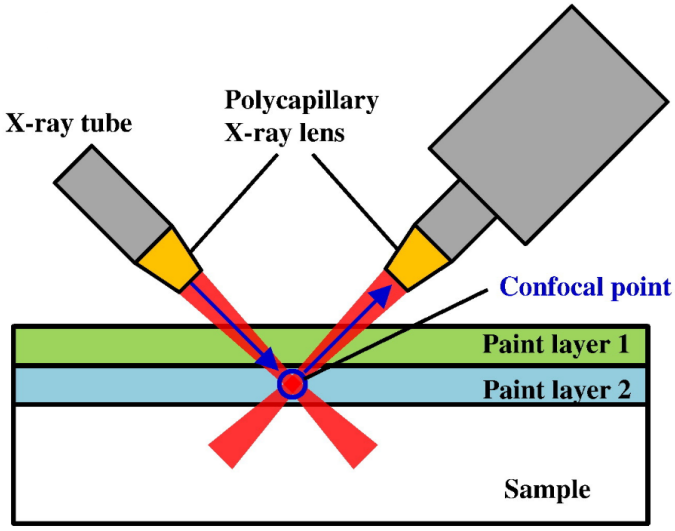

Figure 2.f: Diagram illustrating confocal volume in confocal XRF [15].

ments of deeper layers. Confocal XRF has been used to obtain depth-resolved information on the elemental distribution of painting layers [16] [15] [17].

2.1.3. Compton & Rayleigh Scattering

Scattering is another significant X-ray interaction when performing XRF. Scattering occurs when an incoming X-ray photon encounters a shell electron and scatters off; if it does not lose any of its energy, the scattering is referred to as Rayleigh or elastic, and the X-ray photon emerges in a new direction. Alternatively, if the x-ray transfers some of its energy and ejects the electron, the scattering is called Compton or inelastic scattering. No resulting fluorescence photon is produced since no higher orbital transitions are possible. Scattering is more prominent in low-Z elements, due to fewer protons strongly binding outer electrons. The intensity of Compton scatter is directly proportional to the material's density and average atomic number in its matrix, which is reflected in the mass attenuation coefficient. In experimental measurements, it is possible to correct for this effect using known Compton and Rayleigh ratios from a reference sample [18]. Scattering can occur for X-rays from tubes and X-rays generated in the sample. Since the former often appears in the measured XRF spectrum, it is more significant when analysing acquired data. This is due to broad continuum radiation with superimposed characteristic lines emitted from the anode (further explanation of X-ray tubes is found in section 2.2.2). Although scattering can occur from continuum radiation, it is more prominent in the characteristic lines. Since the amount of energy lost during scattering is not fixed, Compton peaks appear broader, to the left (low-energy) side of corresponding Rayleigh lines. This is clearly seen in Figure 2.g, where Rayleigh and Compton scattering of Rh K lines is measured from a Rh anode X-ray tube. It is also noted that the lower Z sample ("Teflon") experiences more scattering than the higher Z sample (iron). Scattering in general is undesirable when performing XRF spectroscopy; however, it can be useful in investigating the output of an X-ray tube. This is achieved by using a low atomic material like polyethene foam to induce scattering

of incoming X-rays without introducing significant characteristic peaks [19]. Low Z elements exhibit stronger scattering due to a large ratio of electron cloud per atom weight, and lack of prominent characteristic fluorescence lines in typical XRF ranges. This setup allows for studying the X-rays produced by tubes, and evaluating their configurations in terms of voltage, current, and material build without interference from X-rays from the sample's fluorescence.

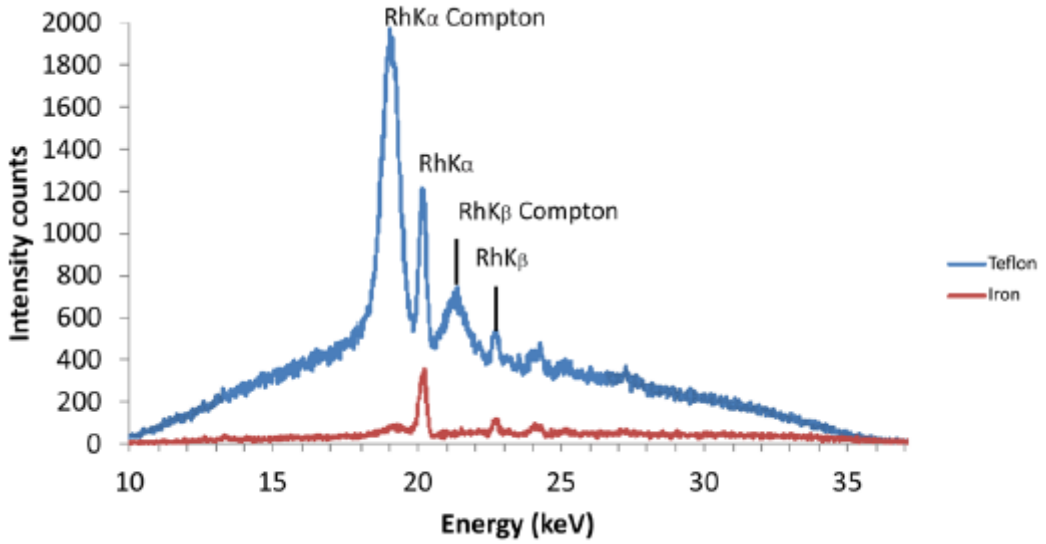

Figure 2.g: Graph comparing an X-ray spectrum of an Rh anode obtained from Teflon and Fe samples. Compton peaks of Rh-Kα and K-β appear broader than their respective Rayleigh peaks. Iron exhibits less scattering due to its higher atomic Z number than Teflon's average atomic Z number [9].

2.2. X-Ray Fluorescence Spectrometers

2.2.1. XRF Setups

XRF spectrometers, handheld or laboratory-based, contain the same primary components: an X-ray source, beam modifiers (or filters), a detector, signal processors, and a device to record the data. A basic illustration of an XRF spectrometer process is shown in Figure 2.h; the experiment begins with an X-ray tube (further discussed in Section 2.2), which generates X-rays that pass through a window and, in some cases, beam filters. Once the X-rays strike the sample, Fluorescent radiation is produced and then detected. The signals are preamplified and processed in a digital processor or multichannel analyser (MCA). Finally, the data is compiled and stored in a device as an XRF spectrum. HDF5 is a standard, versatile file format capable of storing multidimensional arrays. There are two primary types of XRF spectrometers: energy-dispersive systems (EDXRF) and wavelength-dispersive systems (WDXRF). The main difference lies in the detection system. EDXRF spectrometers use detectors that directly distinguish the radiation coming from the sample. Although the dispersion process is more straightforward, the system suffers from the resulting background profile, making it challenging to detect elements at low concentrations. This is due to the scatter tube radiation, which interferes with fluorescent radiation. WDXRF, on the other hand, uses a diffraction crystal to separate incoming X-rays by wavelength (similar to the working principle of a prism dispersing light). Each element's fluorescence is isolated one at a time by scanning through angles. A notable drawback, however, is the high cost and power requirements. All XRF components and their processes will be discussed in the following sections.

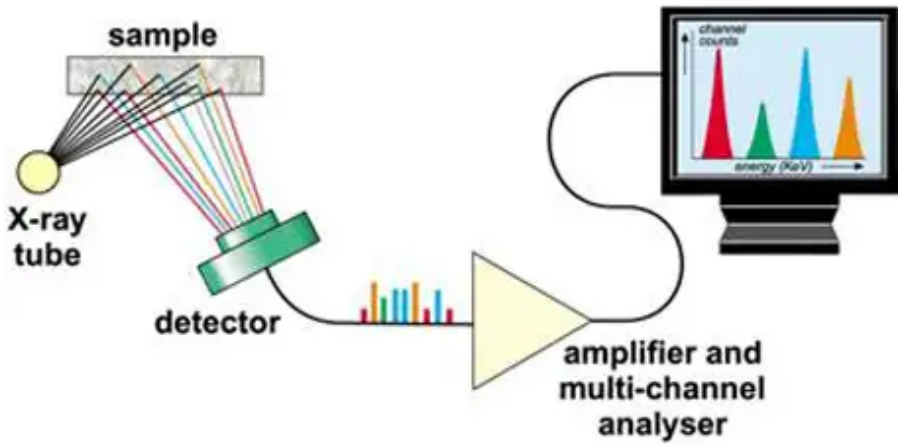

Figure 2.h: An illustration of a common XRF setup.

2.2.2. Excitation Sources

X-Ray Tubes

The basic principle of X-ray tubes begins with electrons emitted from a cathode, which are accelerated towards the anode under an electric field created by the positive potential of the

anode relative to the cathode. As electrons strike the anode material, they interact with the present atoms and lose their energy through several processes. Firstly, Incident electrons may undergo elastic or inelastic scattering on the target nuclei and can be backscattered in the opposite direction. Since elastic scattering is independent of energy loss, it is more dominant than inelastic scattering. The small number of incident electrons undergoing inelastic scattering decelerate continuously in a strong Columb field of nuclei, gradually losing their energy. Such an effect gives rise to the continuous spectrum, known as Bremsstrahlung (a German term for ”braking radiation”). Secondly, incident electrons interact with target electrons, leading to an energy transfer. This is the dominant process, consisting of many collisions with outermost electrons, resulting in small energy losses at each collision. Occasionally, an inner electron is removed from its position in the orbit due to a collision, causing the atom to ionise. Then, as another orbital electron fills the vacancy, it radiates an X-ray quantum. Such a process is the basis for characteristic lines in X-ray emission spectra.

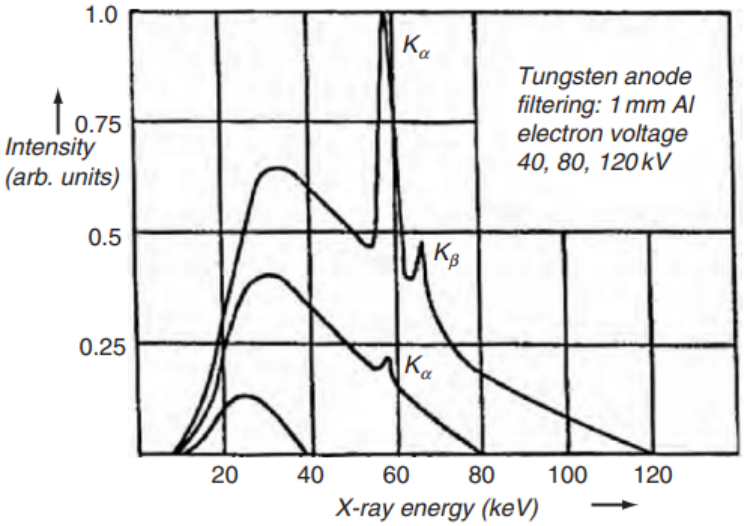

Figure 2.i: Obtained spectra from an X-ray tube with a tungsten anode [20]

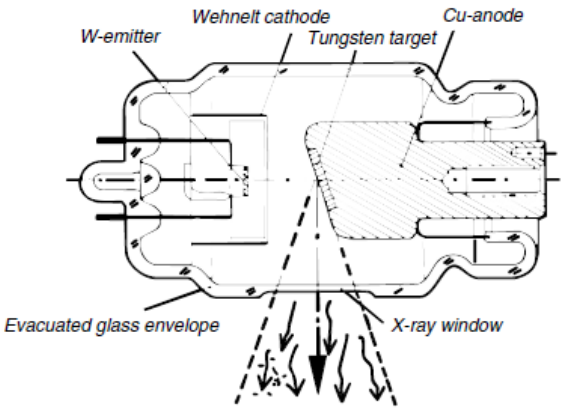

Figure 2.j: Design of an X-ray tube with a side-window geometry. Typically used in dental applications [10]

Figure 2.i showcases an example of typical X-ray tube spectra obtained using a tungsten anode for different anode voltages [20]. Each spectrum is a 'superposition' of the continuous part and characteristic lines, which are seen as peaks on the spectra. The intensity, form, and maximum energy of each distinct line depend on the high voltage value U. The position of the discrete line is characteristic of the anode material. It should be noted that for every line, there is an excitation threshold, meaning a minimum energy is required to excite an electron from a lower energy level to a higher energy level. This threshold corresponds to a specific absorption edge, where a sharp increase in X-ray absorption occurs. A characteristic line will not be emitted unless the acceleration voltage exceeds such a threshold. It can be observed that the intensity of a line increases with an increase in accelerating voltage. The leftmost fallout is due to X-ray absorption in the exit window (and thus in the air) [10] [21].

The general design of a modern X-ray tube consists of a cathode and an anode mounted in a high vacuum ($< 10^{-6}$ Torr) chamber, where the tube is either sealed or perpetually pumped. The cathode is a contained, heated filament, usually tungsten, which is the basis for controlling the emission current. The anode is typically an elemental metal, such as chromium, copper, molybdenum, or tungsten. Figure 2.j illustrates a standard X-ray tube design. A tungsten-based electron emitter is directly heated and focused onto an anode. The target consists of a thin tungsten disk embedded in a copper block, allowing heat dissipation away from the target. Emitted electrons accelerate using an electric field (applying a negative potential to the cathode while the anode is grounded). The tube is sealed in a vacuum via the glass housing. Although X-rays are emitted in all directions, they emerge from the device through an exit window. In other designs, specifically for spectroscopy applications, a thin beryllium film is used as an exit window to minimise X-ray absorption at the low ends. The distance between the exit window and the anode can dictate the beam's intensity; bringing the anode closer to the window intensifies the beam. However, a design concern is the exit window heating due to scattered anode electrons, which is imminent when both the anode and the window are grounded. Other tube designs include end-window tubes, which make use of shorter anode-window distances for better low-energy outputs. Another device type, shown on Figure 2.k is the transmission-anode that makes use of thin targets on the window with intrinsic filtrations of continuum at low power.

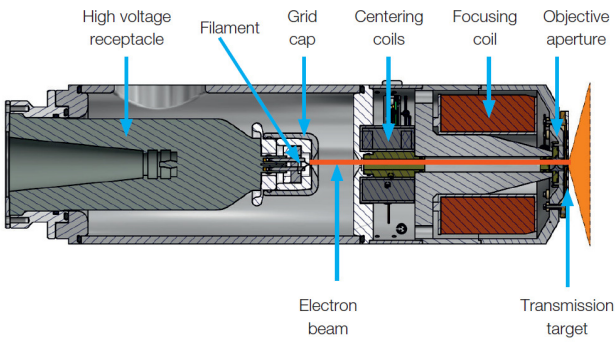

Figure 2.k: Diagram of a Micro-focus transmission X-ray tube, used for high resolution applications [22].

A common challenge when using X-ray tubes is the presence of secondary (or off-focal) radiation originating from electrons that backscatter off the target and interact with the tube housing. This effect has been shown to have a non-negligible contribution to the X-ray spectrum [23]. Figure 2.I showcases an X-ray spectrum of a modelled transmission tube with and without the inner molybdenum structures, highlighting the contribution of secondary radiation on the total spectrum. Many hardware and software corrections have been proposed to tackle this effect, including using a collimator to shape or focus the X-ray beam and software corrections aided by behavioural models of secondary radiation created using Monte Carlo simulations [24].

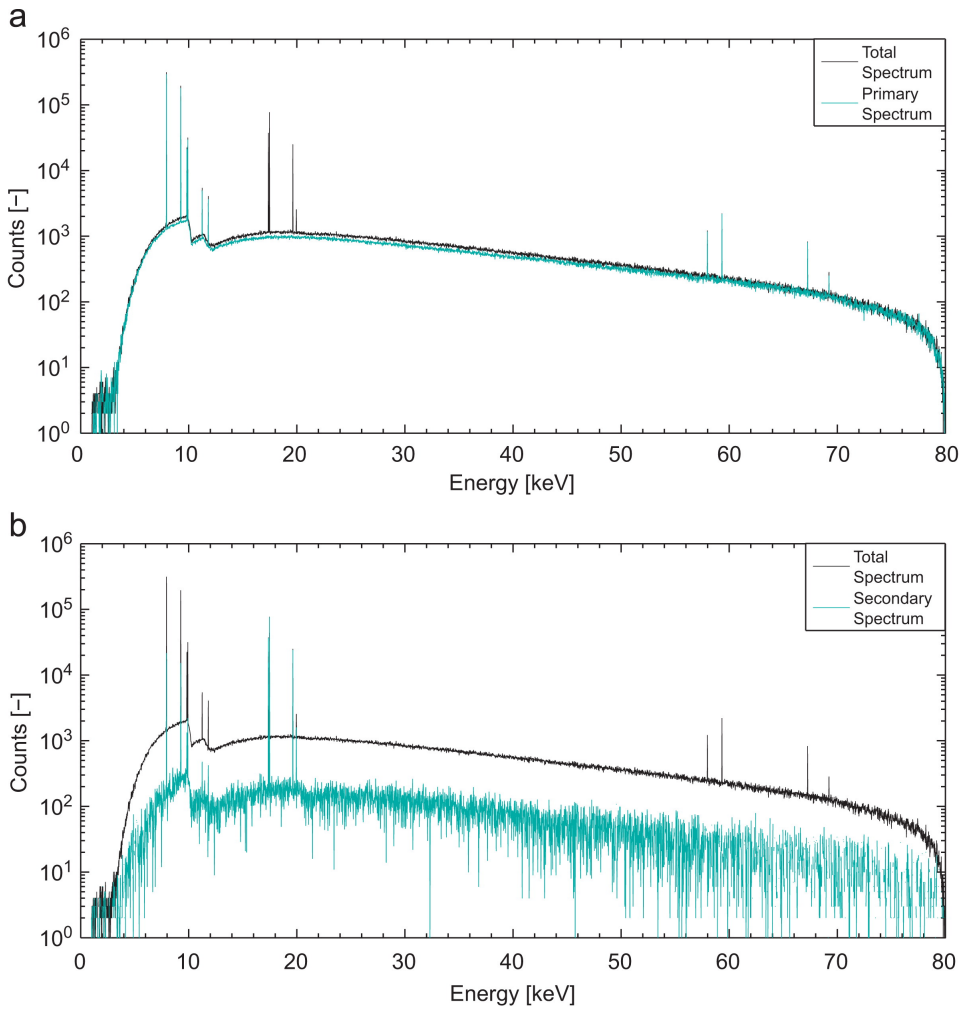

Figure 2.I: (a) Simulated X-ray Spectrum of a tube system without inner molybdenum structure (b) Simulated X-ray spectrum of the tube system with the inner structures and the difference between the total spectrum and primary spectrum, showcasing the spectrum of secondary radiation [24]

X-ray fluorescence included by the anode in X-ray tubes produces characteristic lines (as shown previously in Figure 2.i) which may interfere with detecting the elements in the samples. Although choosing between standard anode materials (Rhodium, Silver, or Tungsten) is a good approach to address this challenge, it is not always possible, and other strategies are needed to deal with the anode's emission peaks. The primary strategy is shaping the output of the X-ray beam to reduce potential interferences. One method of controlling the tube output is

the choice of voltage. The voltage in X-ray tubes directly determines the maximum energy of the X-ray continuum: providing sufficient energy (greater than the absorption edge of the anode) leads to the removal of core electrons from the anode material. The voltage needed to supply this energy is called the 'excitation' potential (in kV). Any element's most significant excitation potential value corresponds with the energy needed to remove an innermost (K-shell) electron. It is then possible to operate at a voltage that selectively excites a specific shell and the corresponding outer shells. For instance, operating tungsten (W) at 40-50 kV (standard maximum for handheld XRF spectrometers) will not result in the excitation of K-shell electrons, which require a 69.5 kV potential to remove. In this case, only L- and M-shell electrons will be excited. On the other hand, using a Rhodium anode, with a K-shell excitation potential V_K = 22.2 kV, its K-shell electrons will be excited, and Rh K lines will appear in the obtained spectrum. The intensity of these lines also correlates with the voltage applied, due to more electrons produced (up to a certain maximum E_{max}). The effect of voltage can be observed in Figure 2.m, showcasing the spectra of CuZn50 obtained with an Rh tube at 40 kV and 15 kV and a constant current of 5 mA. It can be seen that higher voltage facilitates more excitation. Similarly, the quantity of electrons flowing through the filament wire, i.e, the current, affects the intensity of X-rays and the continuum, influencing the XRF spectrum. The output of an X-ray tube can be understood as a combination of the continuum and the characteristic lines; therefore, the applied current and voltage directly influence the range of energies produced and distinct lines. More specifically, the intensity of the continuum is generally proportional to the square of the tube's operating voltage (V) and directly proportional to the applied current (A).

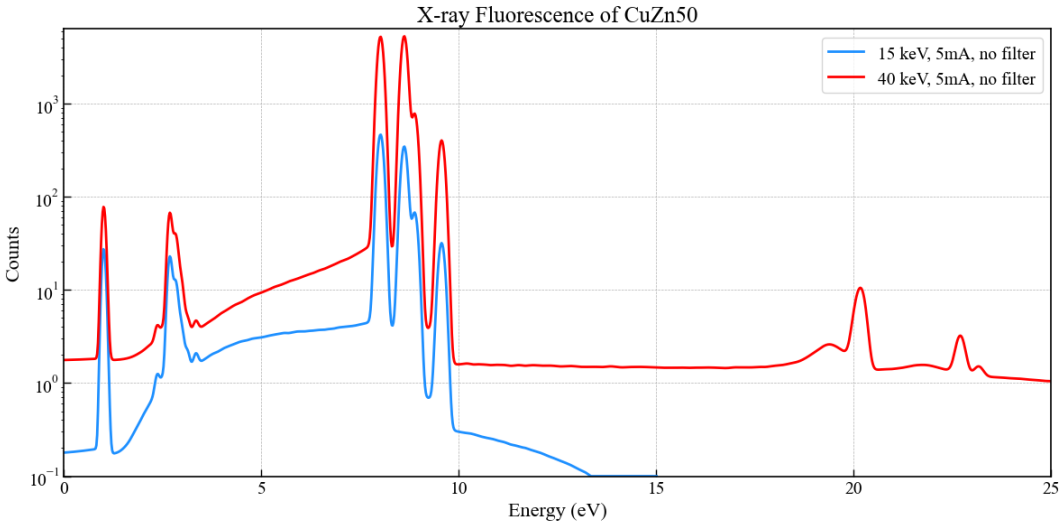

Figure 2.m: CuZn XRF Spectra obtained using XMIM-SIM. The spectra are simulated using different voltage values on the Rh tube.

In summary, the X-ray tube's output shape is essential for producing a desired range of energies and intensity in the acquired XRF spectra. While continuum determines the range of excited elements, only energetic parts, i.e energies above the absorption edge, aid in the excitation of an element. On the other hand, the characteristic anode lines contribute additional

excitations of elements with absorption edges just below the characteristic lines.

Radioisotope X-ray sources

Radioactive X-ray sources use sealed isotopes that emit radiation through natural decay. Their main advantage is stable emission despite temperature, pressure, and other environmental factors. These sources are compact, cost-effective, and require no external power, making them suitable for portable and handheld instruments. The main drawbacks of radioactive sources are their fixed energy ranges and intensities. Additionally, radiation safety regulations and procedures restrict their use further. The radiation can be emitted as discrete lines from nuclear decay (gamma or characteristic X-rays) or as a continuous spectrum from bremsstrahlung, when beta particles interact with matter. The choice of a radioactive source is made based on the binding energy of the targeted atoms, where the binding energy must be exceeded. However, if the excitation energy is too high above the binding energy, the photoelectric effect becomes inefficient.

The emitted spectrum from such a source is affected by source size, shape, and coating. High-Z coatings, for instance, can absorb low-energy photons [25]. Background contributions from scattering (Coherent and Compton) can also reduce sensitivity for weak signals. Different isotopes are chosen depending on the element range of interest. Beta-based sources cover wider energy ranges but suffer from high background noise. Photon-excited sources, where the isotope excites a target material, allow control of the output energy; however, their photon yield is relatively low. Their most common use is calibration, as in the case of ^{241}Am exciting Cu, Rb, Mo, Ag, Ba, and Tb to produce multiple characteristic lines, as shown in Figure 2.n.

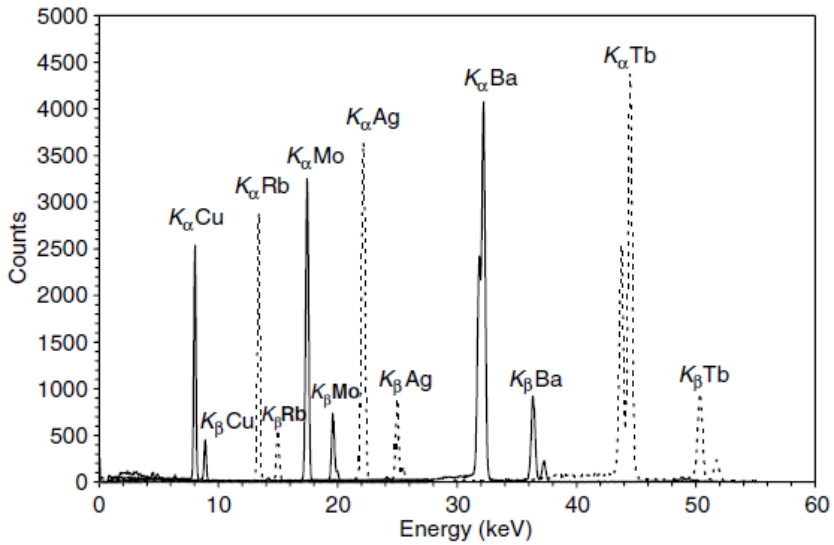

Figure 2.n: Emission spectrum of ^{241}Am [10]

2.2.3. Synchrotron X-ray sources

Synchrotrons are exceptionally bright, high-energy radiation sources useful for analysis techniques such as absorption and phase contrast imaging, diffraction and spectroscopy. They are

often used for cutting-edge research in material science [26], biology [27], and chemistry [28]. In synchrotrons, electrons are produced and injected into a booster ring and accelerated to nearly the speed of light. Then, they are transferred to a large circular storage ring, where they travel in a continuous loop. Powerful electromagnets bend the electrons to follow the curved path, leading them to emit intense synchrotron radiation. Other devices, such as Wigglers and Undulators, can be used to enhance the intensity and brightness (respectively), providing highly collimated synchrotron X-rays [29]. Figure 2.o showcases the photon flux against photon energy for different X-ray sources, showcasing the superior flux provided by synchotron components compared to conventional X-ray tubes. The graph also highlights the differences between the various magnetic components of a synchrotron, since they operate based on distinct physical principles and provide different radiation characteristics. Wigglers provide high-flux X-ray beams via large electron oscillations with a broad and continuous spectrum. These radiation characteristics are used for hard X-ray imaging. Conversely, through small controlled oscillations, undulators provide bright and coherent radiation with narrow spectral bandwidths. These extremely bright and monochromatic X-ray beams are used for phase-contrast imaging and high-resolution X-ray diffraction. Magnetics beams are relatively cheaper components, providing moderate intensity and brightness, and are useful for general-purpose X-ray spectroscopy, imaging, and absorption studies.

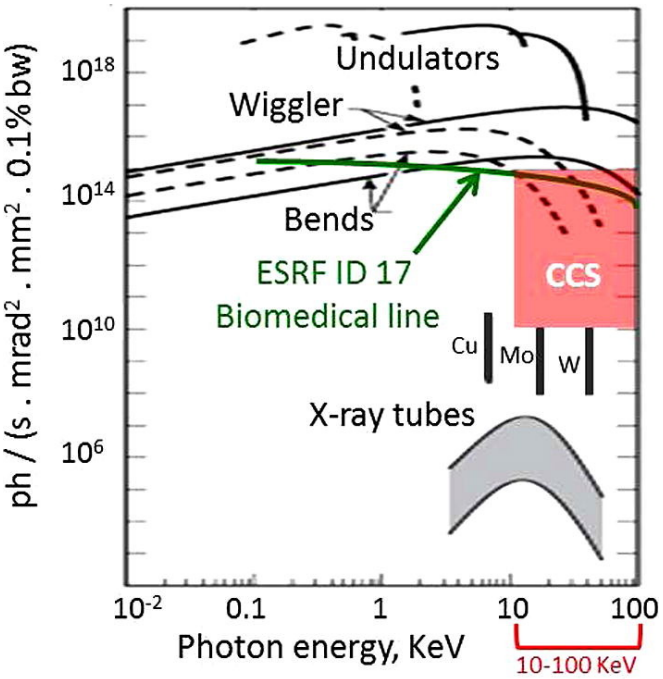

Figure 2.o: Brightnesses of Synchrotrons of conventional lab sources and of compact compton sources projects. [30]

Advantages of using Synchtoron as an X-ray source include High brightness, precise tunability, and elevated spatial resolution. The drawbacks of such technology include its high costs and complexity, which make it impractical for routine laboratory XRF. Nonetheless, they offer unparalleled brightness and resolution for advanced material analysis.

2.2.4. Detectors

X-ray detectors are devices that convert X-ray photons into electrical signals in the form of pulses. Semiconductor-based detectors commonly use Silicon (Si) and Germanium (Ge) as detector materials. When an incoming X-ray strikes the detector material, the three main interactions are the Photoelectric effect, Compton scattering, and Rayleigh scattering. In semiconductor materials, the photoelectric effect is dominant up to 100 keV. Compton scattering is relevant above 100 keV, while Rayleigh scattering becomes more prominent below 50 keV [10]. The contribution of these effects is shown in Figure 2.p for Silicon (Si) and Germanium (Ge), where the mass attenuation coefficient of each effect is plotted against the energy of the collected photons [31].

The 'generation' time of carriers in detectors can range from a few ps in semiconductors to a few µs in some inorganic scintillators. In gas-filled or semiconductor detectors, carriers 'collection' time depends on their mobility, the applied electric field, and the travel distance, which can range from nanoseconds in conventional silicon detectors to microseconds for gas-filled detectors. Consequently, the generated signal shape at the output of the detector is typically represented as a current pulse; the integral of the pulse is equal to charge Q, and the width is equal to collection time (while assuming negligible generation time). An important consideration about detector parameters is the maximum count rate (per second) that the detector may record. When multiple X-rays strike the detector, it may reach its maximum count rate, which momentarily 'saturates' the detector and cannot collect or process spectra reliably. In this case, lowering the current and collecting spectra data over an extended period is needed to avoid saturating the detector.

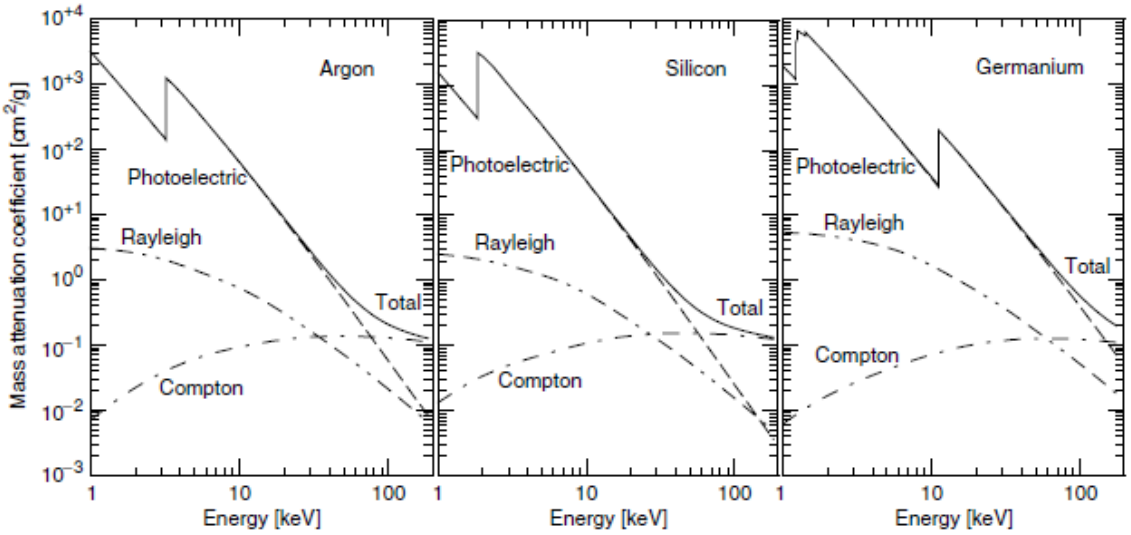

Figure 2.p: Mass Attenuation Coefficient for Argon, Silicon, and Germanium with photoelectric, Rayleigh, and Compton components separated and shown across the 100 keV energy range [31].

Finally, the signal pulses are typically processed through a multichannel analyser (MCA), which determines the X-ray's energy. During XRF acquisition, the MCA counts the instances of X-ray energies, recording them into 'bins' of a certain width. The detector's resolution is directly

related to the width of the bins, with narrower bins resulting in a higher spectral resolution. The digital process then builds up a spectrum, consisting of count rates associated with each energy channel. Developments in detector technology have enabled improved resolutions and high effective count ranges, especially for portable devices. For instance, silicon-drift detectors (SSDs) and silicon PIN diodes (SiPINs) use Peltier or electronic cooling [32]. In the case that a detector struggles to separate two close-by peaks effectively due to insufficient spectral resolution, software can assist in resolving spectral line overlaps. This may be done in the process of deconvolution to differentiate close-by peaks.

2.2.5. Optics

Optics in XRF XRF measurements often demand high spatial resolution, which can be achieved by shaping the X-ray beam. Many devices, such as optics and collimators, are used to achieve desired beam shapes and features. A traditional method for defining a small aperture utilises pinhole collimators. They are used to produce precise spots of sizes less than 50 µm. This method, however, reduces beam intensity, necessitating longer acquisition times [33]. This can be partly compensated for by using high-power X-ray sources. That said, a more modern approach relies on polycapillary optics. Polycapillary optics are bundles of thousands of glass tubes, called capillaries, which are gently curved to reflect X-rays, as sketched on Figre 2.q. They can focus, collimate, or redirect the beam, providing much higher intensity than pinhole or crystal-based optics. Polycapillary optics can increase flux by one or two orders of magnitude when compared to monocapillary systems. [34]. Their performance depends strongly on photon energy. X-rays with low energy transmit efficiently, while higher energies may be lost due to critical-angle limits within the polycapillary. [35]. This feature behaves as a natural low-pass filter in pollycapillaries, allowing them to reduce high-order harmonics [36]. Optics, especially polycapillaries, are essential tools for achieving high-intensity X-ray beams with high resolutions in some modern XRF systems.

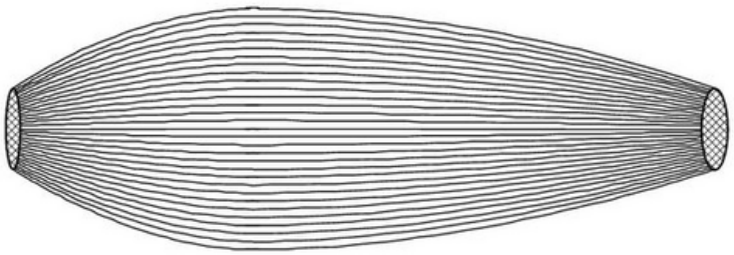

Figure 2.q: Sketch of the inner channels of a polycapillary optics. Features include short input and long output focal lengths [36].

2.3. Spectrum Evaluation

Spectrum evaluation is an essential step in X-ray Fluorescence Spectroscopy (XRF). Spectrometers rely on mathematical procedures to extract relevant information from the acquired X-ray spectra. Methods such as graph smoothing and peak search aid the human observer in interpreting the spectra and identifying elements in the sample. Further analysis of the fluorescence lines' net peak areas can be achieved using various methods, ranging from simple summations to sophisticated least-square-fitting. That said, extracting analytically relevant information from experimental spectral data is never straightforward due to expected measurement noise, such as energy and electronic noise [10]. Experimental conditions should, therefore, be optimised (as much as possible) to reduce noise; this can be done using a stronger primary beam, good-quality detectors and electronics, and enhanced X-ray shielding with longer acquisition times. One should not rely on mathematical procedures alone without optimising experimental conditions. In addition, inevitable spectral artefacts appearing in the spectrum must be accounted for when processing the information present in the spectrum.

2.3.1. Components of an X-ray Spectrum

Understanding all the components and phenomena contributing to the acquired final spectrum shape is crucial for evaluating any XRF spectrum correctly. A typical spectrum includes two main features: characteristic fluorescence lines and a continuum, as well as a variety of spectral artefacts. Characteristic fluorescence lines arise from electronic transitions within the atom and are the most prominent feature in the XRF spectra. The transitions yield discrete, well-known peaks, such as Kα and Lα lines, specific to each element. The natural emission shape is Lorentzian; however, due to the energy resolution characteristics of some detectors, the shape is broadened and becomes more Gaussian in nature. For practical purposes, the Gaussian approximation is often sufficient with mid to low-Z elements; Lorentzian contribution is more pronounced for heavier elements [37]. A continuum background is also present in the spectra. In XRF applications where the sample is excited by primary X-ray beams, the continuum results from scattered coherent (Rayleigh) and incoherent (Compton) radiation. The presence of absorption edges due to materials in the sample or detector also contributes to the background; additionally, self-absorption further complicates the background. Consequently, the shape and magnitude of the background are strongly influenced by the excitation source (in this case, X-rays) and the sample's composition.

Various spectral artefacts are expected in a realistic X-ray spectrum, which complicates data interpretation, especially during trace element analysis studies [37]. For instance, the interaction of X-ray fluorescence with the detector can result in absorption within the detector itself, generating artefacts such as escape peaks. Escape peak probabilities are related to the detector angle, type of present elements, and count rate [38]. For example, the absorption of some of the photon energy by a Si atom in the detector reduces the apparent energy of the acquired peak by 1.74 keV (equal to Si-Kα's energy line). This is shown in Figure 2.r of Fe escape peaks using a silicon-based detector, which appears 1.74 keV below the Fe K-lines. Another common artefact is sum peaks, which occur when two or more photons ar-

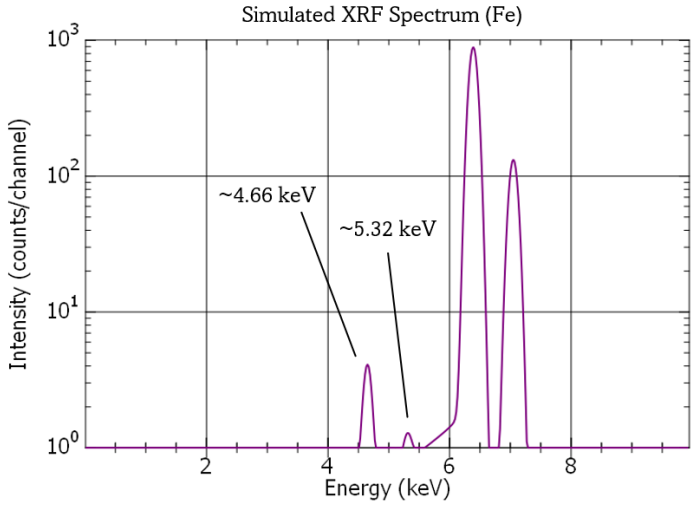

Figure 2.r: Fe XRF Spectrum simulated using XMI-MSIM. Simulation includes escape peak support, yielding escape peaks due to absorption within the silicon-based detector.

rive at the detector simultaneously so that their energies are recorded as a single, combined event. This yields a false peak located at two times the energy of the incoming photons. The system's pulse processing time (or dead time) determines the likelihood of photons overlapping. Factors affecting sum peak also include count rate and element concentration, where the possibility of summation increases with high X-ray flux for highly concentrated elements in the sample. The interference of these false peaks with real acquired signals stands in the way of spectrum interpretation. Mitigating such artefacts can be done by modifying the experimental conditions; for instance, strategies such as reducing count rates, restricting beam intensity, and using enhanced detector systems with shorter dead times can mitigate some of the effects of sum peaks [39]. With escape peaks, the choice of detector material and geometry can help reduce such artefacts. Further artefact peaks from the X-ray tube source target, such as Bremsstrahlung backscatter, Compton scattering, and Rayleigh scattering peaks, may appear and should be accounted for.

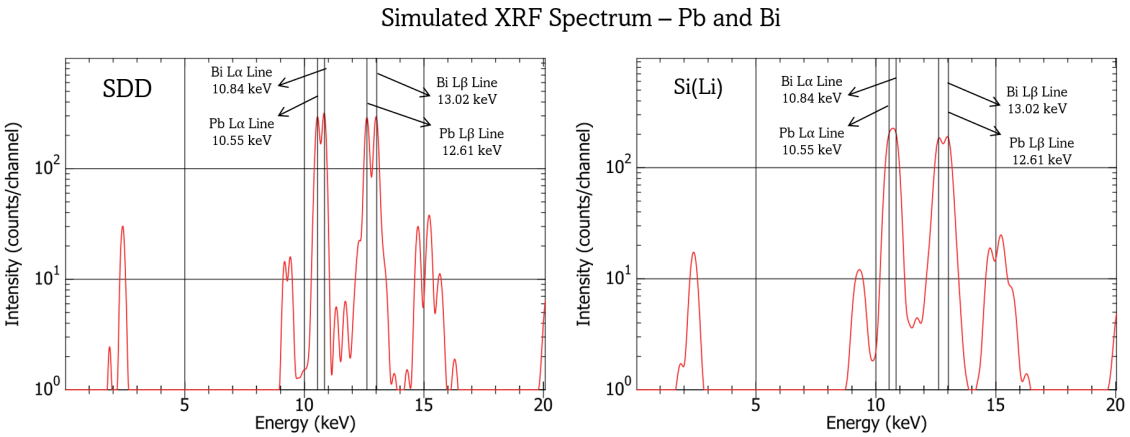

Figure 2.s: XRF Spectra of samples containing Pb and Bi, simulated on XMI-MSIM and using a Silicon Drift Detector SSD (Left), and Lithium-Doped Silicon detector Si(Li) (Right). The SSD detector shows better peak separation of L-lines due to its superior resolution.

Another factor to account for in a multi-element sample is peak overlap, a consequence of limited detector resolution (shown on Figure 2.s). However, other lines from the overlapped elements can help confirm their presence or absence in a more complex XRF spectrum. Therefore, careful spectrum evaluation is necessary when there is a lack of sufficient detector resolution. On the computational side, mathematical corrections in the software should be employed to identify and correct spectral artefacts wherever possible.

2.3.2. Hyperspectral Imaging

XRF has undergone technical advancements in the field of X-ray sources, optics, and detectors. Modern XRF systems can acquire elemental distribution images and data with dwell times of a few milliseconds per pixel [40]. Further developments in full-field [41] imaging have also witnessed significant technical progress, with studies capable of acquiring XRF datasets with several tens of millions of pixels [42].

Hyperspectral imaging has been a common approach for XRF. When using a 'Whisk-Broom' scanning method, the XRF scanner acquires data point-by-point. The detector collects a full spectrum of emitted X-rays at each scanned pixel, resulting in a hyperspectral data cube of many spectra. A hyperspectral data cube is visualised in Figure 2.t. Sampling intervals determine the spatial resolution achieved during measurements, directly dependent on the beam and step size. In some cases, using step sizes smaller than the beam in one or two directions can result in smoother interpolation, improving apparent spatial fidelity without actually improving the data [43]. Dwell time is thus measured as the time of each pixel measurement, allowing for the estimation of the total scanning time of the object; a tradeoff between spectral quality and acquisition time is commonly made to find a good balance.

Once acquired, the XRF data cube can be explored by inspecting the sum and maximum pixel spectra. An example of this is shown in the plot of Figure 2.u, where the sum of the spectra allows for identifying elements present via their signature fluorescence lines; maximum pixel spectra corresponding to the highest intensity of any energy channel allow for identifying locally present elements. For each spectrum in the hypercube, the profile of fluorescence lines with a spectral continuum below them can be combined and linearly expressed. This yields a final representation in the form of qualitative elemental distribution images, with brightness indicating the intensity of the measured fluorescence (Figure 2.u). Quantification is possible in principle, requiring, however, good statistics and knowledge of layer thickness and composition [43].

2.3.3. Processing Large Datasets

As beneficial as hyperspectral imaging can be, evaluating several millions of pixels can be challenging: first, timely data processing is needed to aid the planning of follow-up experiments, and second, the present spectral features and artefacts must be accounted for. For instance, Complex backgrounds due to polychromatic excitation and heterogeneity of samples can complicate the analysis. This is especially relevant for recently developed mobile Macro-XRF instruments investigating paintings in situ at museums or galleries. Small scanning areas of 10

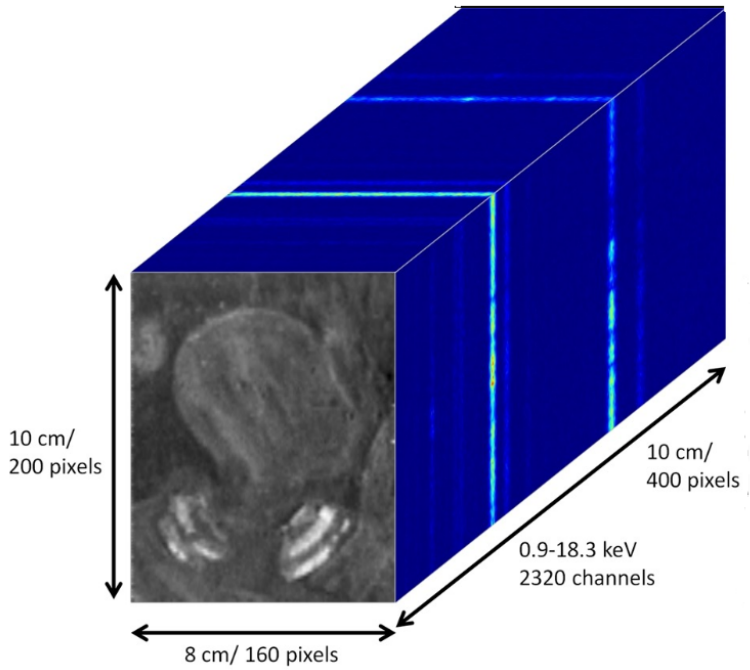

Figure 2.t: A visual representation of a hyperspectral XRF data cube with 200 x 160 x 400 pixels of data. Data acquired at Theban Necropolis in Egypt [43].

x 10 cm^2 with step size 100 µm can produce upwards of 1 million energy dispersive XRF spectra (with 2-49 or 4096 channels) [42], thus a timely processing and data evaluation is critical, especially since full artworks not typically fully scanned, but instead several sub-sections.

Many software packages for data evaluations have been developed to meet the demand for timely data processing that considers potential spectral artefacts and backgrounds. Desired features, such as the fast processing of extensive datasets, production of artefact-free elemental distribution images, and batch job scheduling and automation, have been incorporated in various extents across many software packages. One commonly used software is PyMCA [44], an open-source package developed by the European Synchrotron Radiation Facility (ESRF) for analysing XRF spectra. PyMCA offers a user-friendly interface while maintaining robust spectral fitting tools that support quantitative and qualitative analysis. For instance, it can model L- M- lines using fundamental parameters. It also includes quick data inspection and processing tools, such as region of interest (ROI) imaging, plug-ins for fitting, and background correction. Many other tailored software, such as GeoPIXE [45] and Datamuncher [42], offer similar advantages and more, such as batch processing and dynamic analysis. Overall, there is no single software which meets all needs. In any case, constant improvements to modern XRF software tools are needed so that data analysis matches the progress made in acquisition capabilities.

2.3.4. Spectrum Processing

An XRF spectrum S can be described by a function f (equation 2.3.1), a linear combination of the spectral background B and peak profiles y_e corresponding to elements e included in the

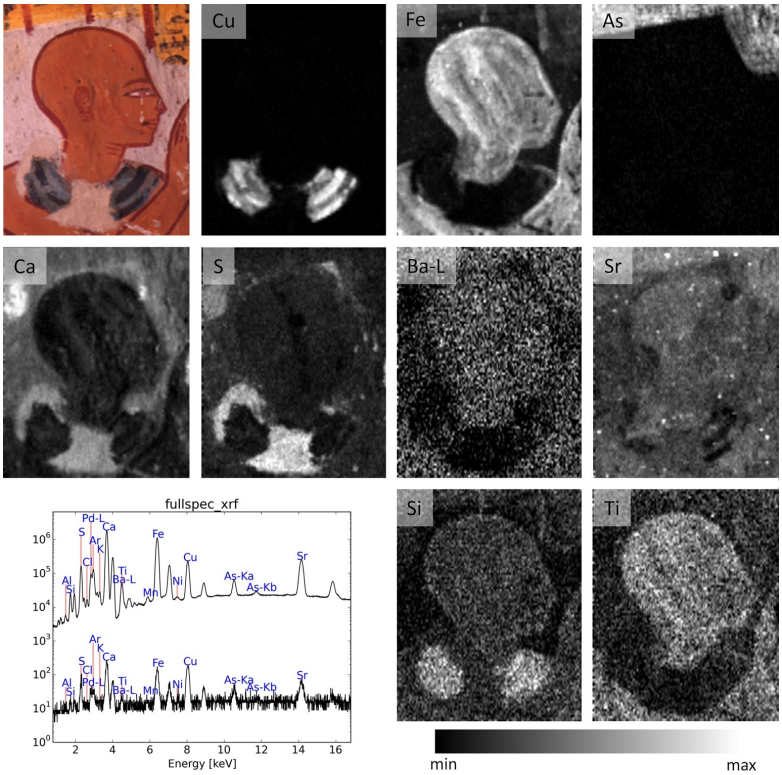

Figure 2.u: Elemental distribution images of the same data presented in Figure 2.t. Bottom left shows a plot of maximum and summed pixel spectra.

fit. y_e depends on non-linear parameters p, such as energy calibration, decor resolution, and peak shape. On the other hand, a_e is comprised of linear factors representing the intensity of the recorded fluorescence lines. The main goal of fitting in qualitative imaging is determining the coefficients a_e (i.e. how much of each element is present for each spectrum).

$$f = B + \sum_{e=0}^{e} a_e y_e(p_0, p_1, \ldots) \tag{2.3.1}$$

Region of interest (ROI) integration is a quick approach to estimating peak intensities and allows for fast visualisation of element distribution. ROI imaging integrates the spectrum S over selected energy ranges. However, this only works well if the target peak dominates in intensity over the sum of all interfering lines k and the spectral background B; this condition for correct ROI estimate from ROI(0) to ROI(1) is shown in equation 2.3.2. Another consideration is the fluctuation of the spectral background B throughout the scanned area, which does not significantly affect the qualitative imaging of element e if it remains relatively uniform. When equation 2.3.2 does not hold, the contribution of interfering lines and the background will lead to misleading ROI images. It is possible to correct for inter-element interference when using ROI imaging if the compositions of the investigated object are well-known, requiring direct user intervention [42].

$$\sum_{i=\mathrm{ROI}(0)}^{\mathrm{ROI}(1)} a_e y_{i,e} \gg \sum_{i=\mathrm{ROI}(0)}^{\mathrm{ROI}(1)} B_i + \sum_{i=\mathrm{ROI}(0)}^{\mathrm{ROI}(1)} \sum_{\substack{k=0 \\ k\neq e}} a_k y_{i,k} \tag{2.3.2}$$

Proper spectra fitting can be done using a least-squares approach to minimise the discrepancy between the measured and modelled spectra; a and p are determined by minimising the value of the reduced weighted squared difference χ_r^2 summed over a user-defined range of channels i (shown on equation 2.3.3. With the n, the number of channels, and m, the number of parameters, the degrees of freedom are defined as $n - m$. Weighting with w_i, the inverse variance, to emphasise (or de-emphasise) parts of the spectrum is typically approximated as w_i = 1/S_i. However, it has been shown that this can be inaccurate at low counts, and w_i = 1/f_i should be taken in such a case [46]. Weighting ensures stronger intensity peaks do not overshadow weaker intensity peaks; when not weighing the data (w_i = 1), the most intense peaks determine the quality of the fit. In this case, a relatively small error in an intense peak contributes a significant error value in the total fit quality, rendering absolute differences dominant.

$$\chi_r^2 = \frac{1}{n-m} \sum_{i=0}^{n} w_i \left(S_i - f_i(a_0, a_1, \ldots, p_0, p_1, \ldots)\right)^2 \tag{2.3.3}$$

Non-linear Least Squares fitting (NL-L) can be realised for the minimisation of chi_r^2 and determining a and p.However, NL-Ls is constrained by two significant limitations, especially when applied to large datasets with low statistics. Firstly, individual spectra with low counts are insufficient for refining non-linear parameters p. Secondly, NL-LS requires intensive computational power and time due to its iterative nature, deeming it impractical for datasets with millions of spectra. The first issue can be addressed by fixing the non-linear parameters at the start of each spectrum's fit, preventing parameter drift during processing [42]. Faster processing to determine non-linear parameters (p) can also be achieved by relying on a high-quality spectrum representative of the entire dataset, which is kept fixed during the processing of the data by Linear Least Squares fitting (L-LS) [44]. An essential aspect of fitting with NL-LS is using constraints to retain physically meaningful results. For instance, linear parameters can be constrained to be positive; a well-defined model to fit an XRF spectrum should not produce significantly negative values for a, and constraints can introduce bias when not used carefully, masking issues with the fit model.

Instead of iterative fitting a model to each spectrum, dynamic analysis (DA) [47] is a proposed computational method for extracting elemental intensity values from spectra using matrix multiplication. Such an approach relies on a mathematically correct yet counter-intuitive pre-defined DA matrix that contains negative values to cancel out overlapping peaks. This method yields speedy analysis of extensive hyperspectral data but with less flexibility due to assumed fixed peak shapes and ratios. Another benefit of DA analysis is its applicability to per-pixel spectra [42].

Accurate background handling is essential in XRF data processing since background B is

not defined in equation 2.3.1. Instead, a few approaches can be used to approximate background signals: Firstly, the background shape can derived from a sum spectrum and fixed during scanning. This method is appropriately fast for homogenous and/or weakly scattering samples. Secondly, the background can estimated through digital filtering and subtracted before deconvolution. A commonly used filter is Statistics-sensitive Non-linear Iterative Peak-clipping (SNIP), which operates on the principle of iteratively removing peaks from the spectrum to isolate the background. The algorithm assumes a background B = S and then compares the average of two neighbouring channels with the channel's current value. If the latter is lower than the average value, it is replaced with such value, effectively 'clipping' peaks away. Such process is governed by a parameter n, which determines how far apart the neighbouring channels are, as is reduced during each iteration; after a limited number of iterations (less than 25 [37], the peaks are eroded, and the background is approximated. Finally, a third method is mathematically modelling the background during the fitting process for every pixel, avoiding iterative computation. For this, polynomial functions are used with either linear or exponential variables. Despite this approach's speed and resistance to low background statistics, it increases the number of parameters in the fit, reducing its stability, especially for higher-degree polynomials. Low-degree polynomials should also be avoided as they do not represent the background data well. Therefore, choosing a polynomial degree is critical to modelling complex, noisy backgrounds without overfitting or creating artefacts.

2.4. X-Ray Fluorescence for Cultural Objects

Development of MA-XRF X-ray fluorescence imaging has been a valuable tool for heritage science for obtaining elemental analysis and distribution of various cultural objects, including historical paintings [48], manuscripts [49], metal artefacts [50], archaeological sites [51], and many others. Its non-destructive nature is appropriate for carefully investigating historical objects, making it useful for restoration and conservation efforts. While the technique is ideal for microscopic samples, it is also employed to examine larger objects by macroscopic XRF imaging (MA-XRF). MA-XRF provides elemental distribution maps of a scanned area on an object, such as a historical painting. Combining produced spectra and images is instrumental in material characterisation and understanding the artist's painting and production techniques.

2.4.1. Past and Present Methods of MA-XRF

Synchotron MA-XRF

Early outcomes of MA-XRF studies began with synchrotron sources. One of the first prominent experiments was conducted at the German Synchrotron DESY in Hamburg, which investigated the surface beneath Vincent Van Gogh's painting "Patch of Grass", characterising a discarded and overpainted layer of a female peasant [48]. The study demonstrates the capabilities of Synchatron MA-XRF in elemental mapping of buried composition in high detail. Using a quasi-monochromatic synchrotron pencil beam of size 0.5 × 0.5 mm^2, a 17.5 × 17.5 cm^2 area was scanned, and elemental maps were created of key elements, such as Pb in white pigment or Hg in vermilion, to identify pigment distribution (Figure 2.v).

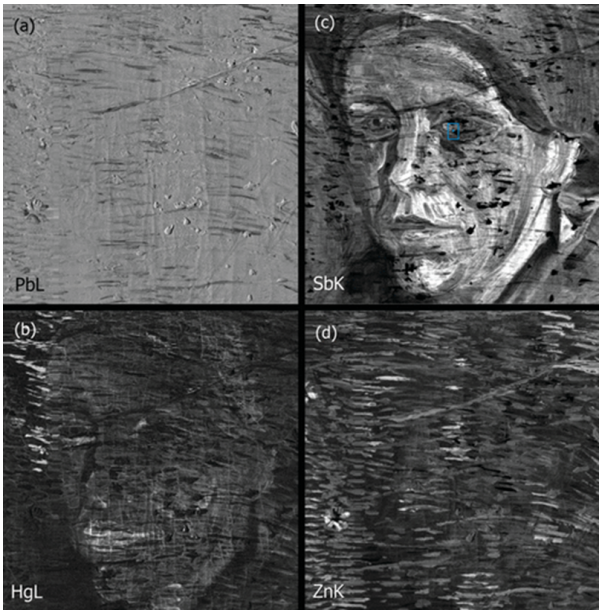

Figure 2.v: a) Distribution of Pb L measured with SR-based XRF (black, low intensity; white, high intensity). (b) Hg L showing distribution of vermillion. (c) Sb K showing distribution of Naples yellow. (d) Zn K showing distribution of zinc white [48].

Such a study showcases a prominent feature of this technique in that the penetrative character of X-rays allows the probing of all paint layers; the heavy elements in the hidden layers produce high-energy fluorescence signals that are not significantly attenuated by surface lay-

ers, therefore allowing the study and visualising of both major and minor components of the painting. That said, the extended acquisition times of this study (2 days with a 2-second per-pixel dwell time) resulted in compromises to the overall scan size. Synchrotron-based sources have proven advantageous in achieving high lateral resolution in MA-XRF, with the straightforward installation of advanced optics [52]. Despite the demonstrated success of synchrotron sources for MA-XRF, the dependence on the infrastructure of synchrotron facilities has brought about logistical challenges related to the transport of artefacts, including insurance, unfavourable climatic conditions, and theft. Moreover, access to a synchrotron source is scarce; therefore, the number of paintings that could be analysed was limited. Finally, it is challenging to incorporate larger-sized paintings without special adjustments to the beam line scanning stages.

Figure 2.w: Bruker M6 JETSTREAM, a mobile XRF scanning system, built to obtain non-invasive high resolution elemental scans of large objects, such as artworks, hertiage pieces, and samples [53].

Mobile MA-XRF

The first MA-XRF experiments using synchrotron sources did not necessarily require the character of the radiation produced by such a source; X-ray tubes were more than capable of exciting heavy elements in paintings. The practical limitations of using Synchatron-based MA-XRF experiments mentioned previously were a driving force in establishing and developing mobile MA-XRF systems. Such mobile instruments benefited from portability, allowing for in

situ investigations of cultural artefacts, such as historical paintings, without the associated risks of transport and inherent limitations related to the size of the artwork. In this case, the artwork would remain stationary, and the measurement head would move relative to it. The convenience of such systems allows them to be easily deployed to museums and galleries, initiating in situ investigations of cultural items. Several mobile MA-XRF instruments have been developed, such as the Bruker M6 Jetstream [53], (Figure 2.w), for the purpose of performing scanning procedures on historical items at the host institute [6] [54]. The versatility and mobility of these instruments have prompted museums to acquire them for their workshops. However, when scanning non-flat objects with irregular geometries, the data obtained suffers from artefacts due to variations in working distances, leading to attenuation in signal intensities. For example, geometric distortion was observed when scanning a Medusa head in the frieze of the Siphnian Treasury in the Sanctuary of Delphi (Greece) [55]. Although not always addressed in modern MA-XRF imaging, the effect of varying geometries (explained later in Section 4.3) leads to artefacts in the acquired data, and unless directly addressed (Showcased later in Section 4.4), can present an obstacle for interpreting imaging results and data analysis.

2.4.2. Effect of Geometry

In X-Ray Fluorescence imaging (XRF), the information obtained is a combination of legitimate signals from the sample and artefacts originating from the scanning setup. Measurement geometry significantly impacts the accuracy of results, and careful understanding of potential artefacts is essential for accurate elemental analysis. There are three relevant components to consider when evaluating the effect of geometry on MA-XRF: the excitation path from the source to the sample surface, the interaction with the sample, and the detection path from the surface to the detector. A spectrometer's design defines an optimised detection geometry, where any deviations affect the recorded signals. Such deviations from the intended detection geometry are relevant when scanning objects with curved or irregular surfaces. Important geometric factors include working distance and surface, which are separate but related effects influencing recorded XRF signals.

Working Distance

Working on working, other distances than the designed working distance impact the excitation and detection paths in an XRF scan setup. For instance, when the distance is larger than intended, part of the main radiation is absorbed in the path from the X-ray source to the sample in the air. Therefore, fewer X-rays are absorbed in the sample, and fewer XRF signals are emitted. Although the scattered Bremsstrahlung X-ray tube continuum contributes to the background noise in XRF spectra, Argon (Ar) is the only excited element in the air with sufficiently high characteristic radiation and quantity to be detected. Figure 2.x showcases the pronounced effect of working distance and solid angle variations in XRF measurements. The measured fluorescence line intensity (in triangle), the solid angle including the collimator (dotted line), and the simulated line intensity (dashed line) of various elements are represented. It

can be noticed that for Zn (main line: 8.63 keV), the acquired intensity matches well throughout. However, the data do not match expected intensities as higher distances are used for Si (main line: 1.74 keV) and Ca (main line: 3.69 keV). This is the pronounced effect of absorption in the air, as less energetic fluorescence radiation is considerably more absorbed by air. For higher energy elements, such as Zr (main line: 15.75 keV), absorption is negligible, and the seen effect is related to the quantum efficiency of the detector [56].

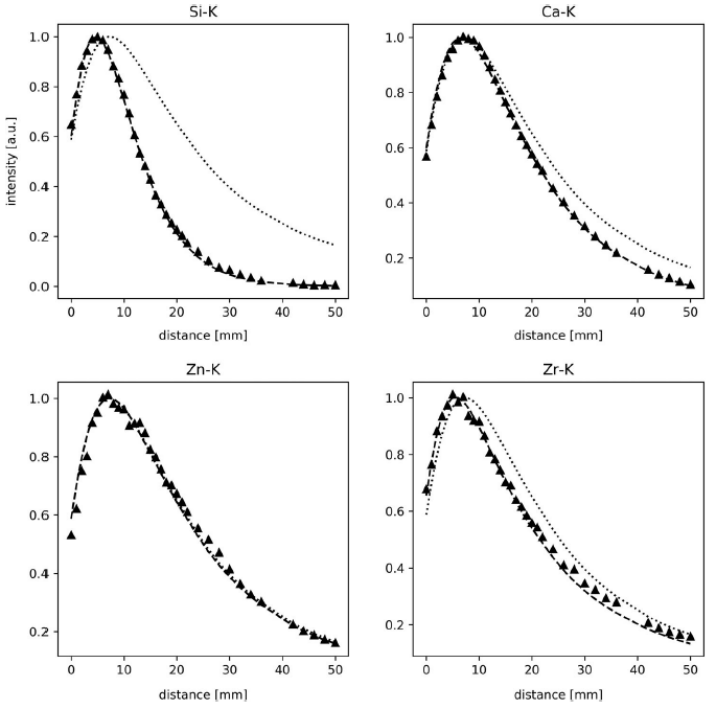

Figure 2.x: The component dependence of fluorescence intensity versus the working distance for several elements. Measured data in spotted lines, simulated model in dashed lines, and the solid angle curve in triangles [56].

In addition to air absorption, working distance impacts the detection side by changing the solid angle. The Solid angles determine the amount of emitted fluorescence the detector ”sees”, thus the amount of photons detected. The solid angle (Ω) of a detector is affected by A_{det}, the active area of the detector, and the distance d from the sample to the detector. With increased working distance, the fraction of emitted radiation reaching the detector decreases, reducing detected signals. This relation is understood as:

$$\Omega(d) = \frac{A_{det}}{d^2} \tag{2.4.1}$$

Figure 2.y illustrates this problem with working distance while considering the effect of absorption and the role of collimation. Detector collimations are used to reduce background noise and partial signals, which often have a fixed or narrow field of view calibrated for a specific design distance. The effect of a closer sample is the blocking of emitted light by the collimator, reducing the apparent solid angle. Although reducing the working distance may seem beneficial for decreasing air absorption, the detector calibration may restrict the field of view for closer objects. Consequently, the solid angle effectively shrinks again.

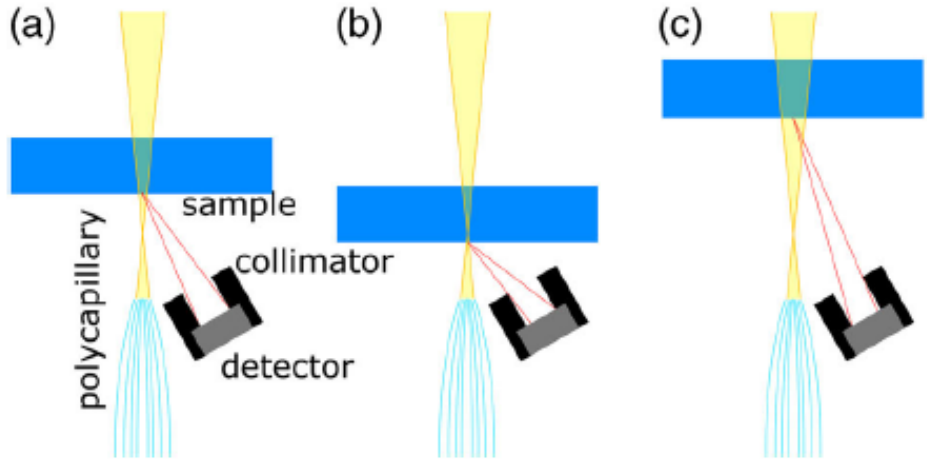

Figure 2.y: Example of Measurement Geometry and variation in working distance. Note: the illustration is exaggerated for demonstration. (a) illustrates the designed working geometry. (b) and (c) show the effect of the detector being too close or too far, respectively. Yellow lines represent the X-ray beam, and red lines represent the detector angle [56].

Surface Tilt

The effect of surface tilt occurs in two ways: in the excitation path, the tilt leads to a longer path for primary radiation, leading to a less accurate ratio of fluorescence line and an overestimated layer thickness. Furthermore, the detection path from the sample to the detector may be larger or smaller (depending on the placement of the detector), influencing the recorded signal strength. The effect of tilt is demonstrated in Figure 2.z. The red and green beams represent the excitation and detection paths. In the upper half of the diagram, A* denotes the desired measurement geometry as per the design of the spectrometer. C shows an increase in working distance. B and D demonstrate the effect of working distance and surface tilt in combination. For B, the surface is tilted away from the detector. Thus, weaker signals are measured compared to D, and the sample surface is aligned with the detector. In the case of E, no data is recorded, as the extreme geometry of the sample blocks any emitted fluorescence from reaching the detector. The lower half of the diagram illustrates the ideal setup for each scenario. The primary beam and detector are adapted to the surface case, maintaining the detection geometry throughout. Case E, however, is unsolvable in the shown experimental setup.

Since X-ray attenuation is energy-dependent, surface tilt can disproportionately affect fluorescence lines. Fluorescence lines with low energy are disproportionately absorbed at shallow detection angles in the sample; high-energy lines, on the other hand, may still escape. The apparent increase in surface thickness, therefore, attenuates elements differently and can result in an inaccurate ratio between different elements, especially in layered samples. An example of the element-dependence tilt effect is shown in Figure 2.aa. In this study by Orsilli & Galli (2024) [58], surface tilt attenuation of element lines is investigated when measuring a 0.8 µm thick layer of gold alloy (Au-Ag) placed on top of a copper substrate. When the detector is shallow (less than 15°), the detector is almost looking sideways across the surface, therefore

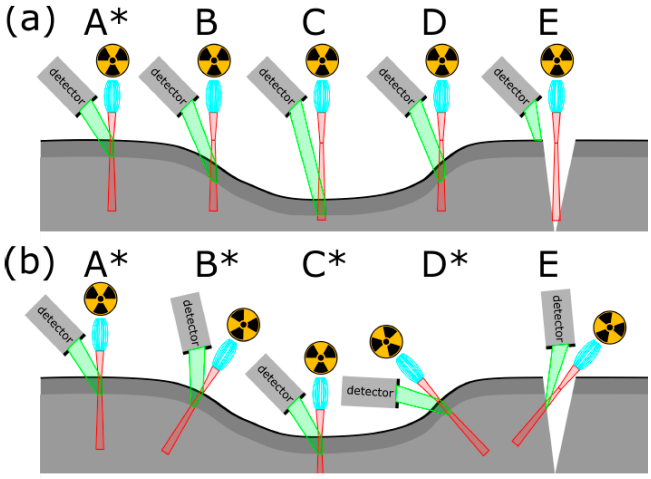

Figure 2.z: diagram illustrating the geometric problem with varying working distances and surface tilts (upper part) and the correct adaptation for each scenario (lower part) to acquire. '*' marks a setup adhering to the working design of the experimental setup. [57].

measuring signals which have to travel longer through the gold before reaching the detector. In this case, copper Kα (8.04 keV) signals are absorbed and barely detected. At 45°, on the other hand, the detector is steeper, and the escape path for copper fluorescence is shorter; thus, they are detected up to ~10 µm.

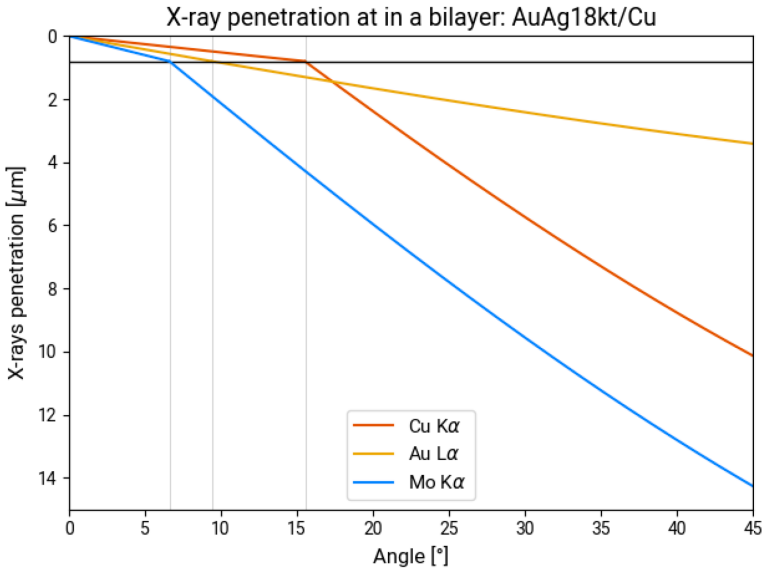

Figure 2.aa: The penetration depth of beams with different energies in a sample of gold alloy (Au and Ag) 0.8 µm thick on top of a substrate of copper [58]

2.4.3. MA-XRF Solutions for 3D Objects

Macroscopic X-ray Fluorescence Imaging (MA-XRF) of historical objects is mostly done using scan heads moving in two dimensions, leading to the aforementioned geometric discrepancies, which significantly affect the quality of the acquired data. The inconsistent excitation and detection of fluorescence signals across a scan manifest as data artefacts, and appear as ac-

quired elemental distribution data; variations of a few millimetres can contribute to observable deviations in sensitivity for [56]. This is especially relevant for curved or irregularly shaped objects, such as ceramics. Even XRF acquisition of historical paintings or manuscripts may suffer due to their slightly curved or uneven surfaces [59].

Several authors in the field have addressed the geometric effect of scanning a 3D object, and various solutions are being developed and proposed, which rely on computational modelling, versatile scanning methods, or a combination of both. Experimental approaches to address geometric effects are highlighted in the following subsections, addressing effects due to variation in working distance, surface tilt, or both.

Data-intrinsic correction

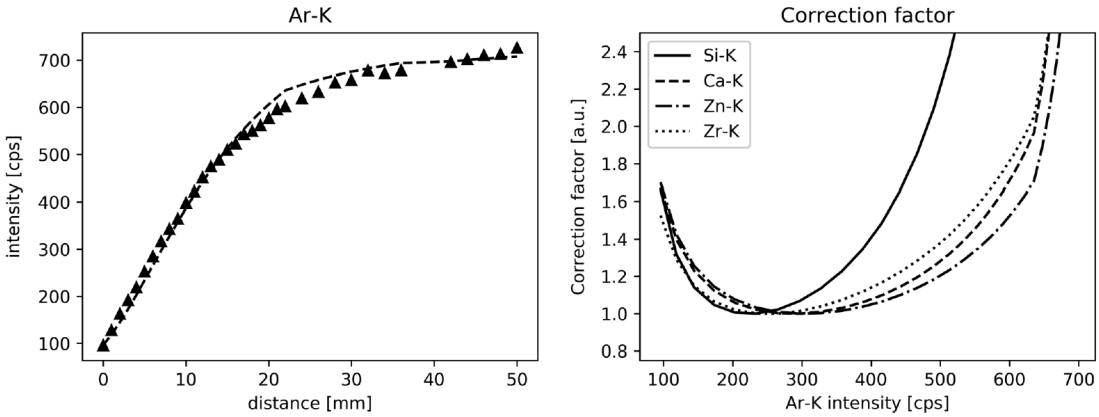

Figure 2.ab: Left: Ar intensity measurements (triangle) and simulated (dashed line) versus working distance. Right: Correction factors for multiple elements derived from the simulation [56]

A significant consequence of variation in working distance is the change in the air path of X-rays, and thus the amount of air absorption during the scan. This manifests in the detected Argon (Ar) signals, where an increase in working distance leads to the generation of more Ar signals and vice versa. Ar, the only element of air with high enough characteristic fluorescence to be detected, can serve as a proxy to estimate variation in distance since its intensity is influenced by path length (therefore, the working distance). One can utilise the variation of the Ar signal across a scanned area to develop signal correction factors for other elements. Alfeld et al. [56] presented this novel approach by leveraging the Ar signal intrinsic to the data. Thus, a model was developed that considers the non-linear relationship between distance and Ar excitation and estimates local variations in the working distance during scanning. The model also finds solid angle calculations for the detector's field of view to achieve accuracy, incorporating detector geometry, collimator shape, and overall alignment. Detector quantum efficiency was also considered during modelling since the angle and working distance influence it. The resulting analytical tool is used to measure the intensity of each element.

Calibration was done using step-wise distance measurements of a NIST 610 reference glass, contacting many elements with known concentrations. The model parameters were then optimised to fit measured data for different elements such as Zn, Ca, Si, and Zr, adjusting for

physical effects like air attenuation and detector response. The Ar signal distance dependence is then characterised, and correction factors are calculated for each pixel in a scan based on the Ar signal present. These correction factors are then applied to other elemental signals to adjust their recorded intensity as if measured at a constant ideal working distance (shown in Figure 2.ab). Noise propagation into the corrected elemental images was prevented by applying a Savitzky–Golay filter, smoothing the Ar maps.

This approach was tested on scans of Rembrandt's "Portrait of Oopjen Coppit." Due to geometric constraints, the painting was imaged in multiple sections, with one section scanned at a shorter relative distance, yielding a visibly reduced calcium signal. Once corrected using the Ar signal, the intensity in the treated section aligned much better, and histograms of signal intensity confirmed improved consistency in overlapping regions, observed in Figure 2.ac. While the model suits the presented case, it has a few limitations. For instance, the model does not consider the self-absorption effect of tilted or thick layers and assumes homogeneous sample layers with perpendicular surfaces. Additionally, the model does not take the impact of beam broadening at different distances, which results in slight residual artefacts due to differences in spatial resolution. Nonetheless, the approach offers a practical solution which requires no additional hardware or external measurements, which may be applied retroactively to existing MA-XRF data in the case of well-characterised instruments.

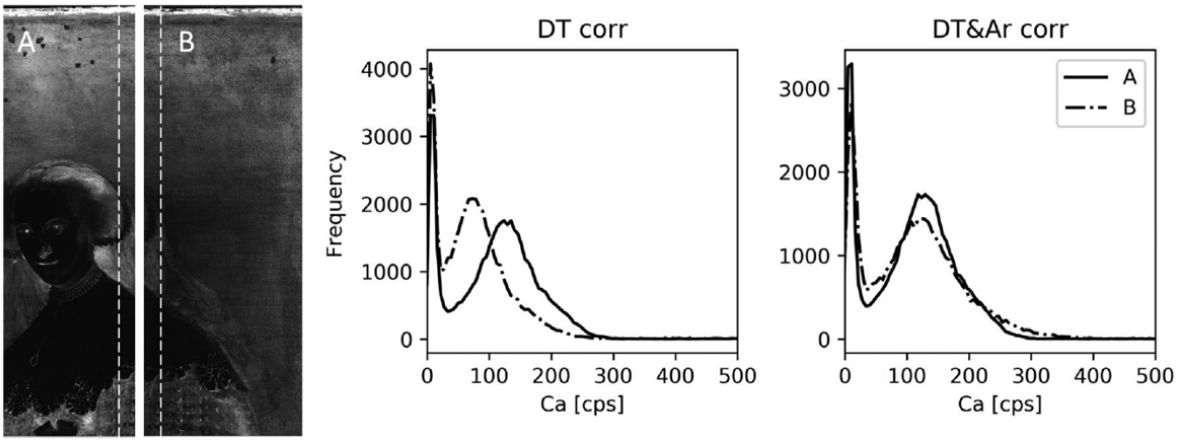

Figure 2.ac: Left: Area of joint histograms, showcasing Ca distribution map. Right: before and after correction of Ca using Ar signal [56]

Robotic repositioning and adaptive scanning

A standard solution to the geometric problem of XRF scanning is the use of adaptive scanning methods to account for the sample's geometry. With this approach, the scan head or the sample is repositioned such that the detector geometry remains consistent throughout the scanning area. This can be typically done using a variety of motorised components, such as robotics arms, stages, and hexapods.

An example of a robotic solution is a cable-driven robot, named CaRISA, which is introduced as an alternative to conventional stacked linear stages for MA-XRF imaging [57]. CaRISA overcomes geometric discrepancies by using eight motorised cables that move a

lightweight platform with five degrees of freedom, maintaining the scan head in the ideal geometry. The system is lightweight, modular, and portable, with a 150 × 100 × 30 cm workspace and ±35° tilt. The mobility of the setup deems it appropriate for in situ heritage object studies. Tests included scanning around a pottery jug, tilting to inspect cracks in a painting, and running resolution patterns at different speeds. The systems showed some drift during large movements due to open-loop control and cable elasticity. Despite this, the use of cables to manoeuvre a scan head allows for flexible and accurate imaging of cultural heritage objects. However, the system is incapable of addressing significant variations in working distance and is not suitable for moving around objects.

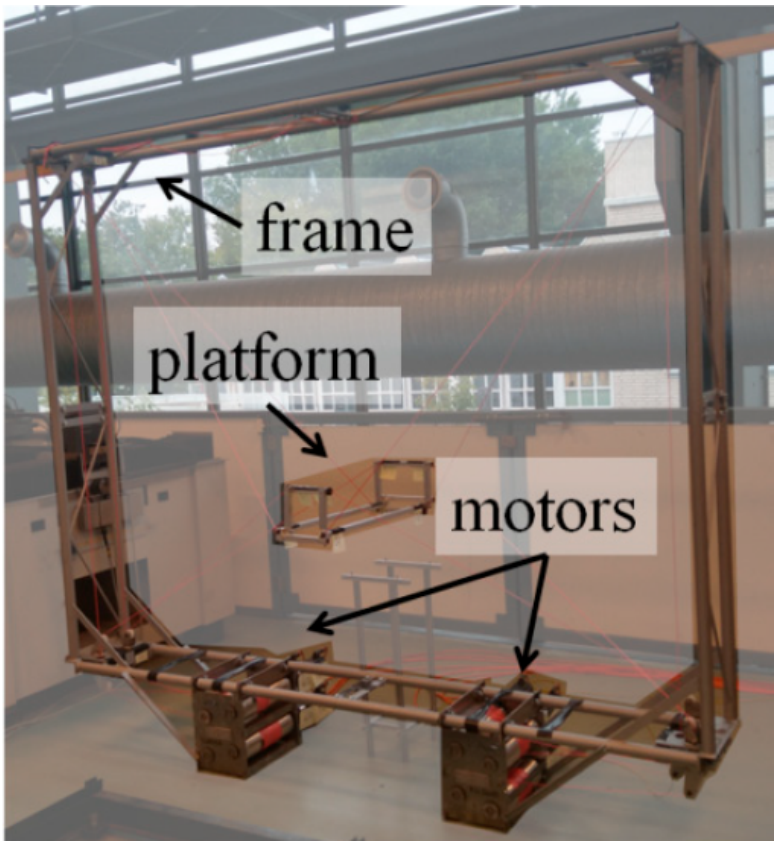

Figure 2.ad: CaRISA fully assembled [57]

Robotic arms are another versatile method of positioning scan heads such that they account for an object's geometry. Typical XYZ motion can be paired with a tilting mechanism, such as a hexapod stage or a robotic joint, to tilt the scan head, can produce accurate surface scans of curved objects. A recent development by Xu et al. [59] showcases the application of this solution: A developed device, shown in Figure 2.ae, consists of a six-axis robotic arm that can maintain a working distance and remain perpendicular to the local surface while acquiring XRF data. The system is equipped with a depth camera, which can produce a 3D point cloud, measuring the required adjustments to working distance and tilt relative during scan. Test scans carried out on heritage objects demonstrated more realistic elemental maps of uneven surfaces. For instance, elements on a convex painted fragment from an ancient building

Figure 2.ae: A surface Adaptive XRF Scanner [59].

were mapped, as shown in Figure 2.af. Overall, robotic solutions offer an effective method for resolving artefacts induced by geometric effects.

Fundamental Parameter and model-based corrections

The use of fundamental modelling can aid in distinguishing elemental data from artefacts due to geometric distortions caused by the sample's irregular surface. When the sample composition is known, it is then possible to simulate accurate XRF signals from complex surfaces. This method was applied to Medusa's head on the Siphnian Treasury frieze, measured using a mobile XRF scanner [55]. In this case, the distortion affects the reliability of elemental maps and can lead to misinterpretation of the presence (or lack thereof) and distribution of pigments. In addition to the previously discussed complications of varying working distances and changes in surface orientation, this study encounters the effects of shadowing and self-absorption, which are caused by curved features blocking and absorbing the emitted fluorescence, thereby skewing measurements. This approach relied on combining 3D photogrammetry with Fundamental Parameter (FP) modelling to correct for geometric effects.

Photogrammetry is a valuable technique for reconstructing 3D models of real objects from a series of 2D photographs. The method relies on the principle of triangulation: Image acquisition is done by capturing multiple overlapping photographs taken from different angles around the object. The photos differ slightly in perspective, allowing them to capture the 3D shape of the target object. In this study, a 24-megapixel camera was used, with natural lighting being sufficient enough for the photos. A companion software was then used to match points, estimating the relative position and orientation of the camera for each shot. A 3D point cloud is generated, and a mesh is processed, forming a continuous surface repressing the object's

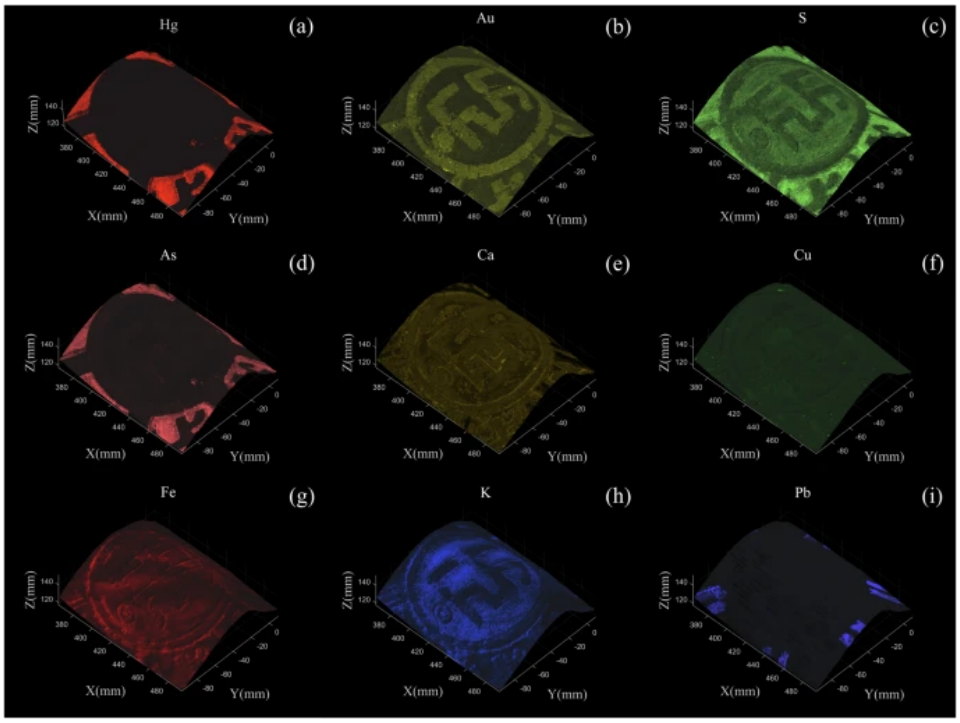

Figure 2.af: Elemental maps of fallen paint, showcasing maps of Hg, Au, S, As, Ca, Cu, Fe, K, and Pb across a curved sample surface. The data was acquired using a surface adaptive device presented by Xu et al. [59]

geometric shape and texture. The resulting lateral resolution of the model was estimated to be 200 µm, much smaller than the pixel size of the obtained XRF (500 µm).

After obtaining the object's model, Fundamental Parameter (FP) simulation was a key component for correcting and interpreting X-ray fluorescence (XRF). The use of FP is relatively straightforward due to the well-characterised instrument under a known geometry. Additionally, the known material composition (e.g., calcium carbonate for marble) aids in calculating the expected elemental signals. Surface geometry, obtained from the 3D photogrammetry model, provides the input for the angle between the detector and the local surface normal, as well as the distance from the X-ray tube.

In the case of Medusa's head, it was difficult to determine whether dark spots on the elemental maps were due to a lack of pigment or just a tilt in the surface. The previously discussed method was therefore applied, simulating the modelled surface as 1) pure marble (for a clean case) and 2) marble coated 10 μm Fe_2O_3 pigment layer (for a painted case). The expected XRF intensities for Ca and Fe were calculated for each pixel based on the geometry and known materials. The simulated pixel data was then compared with measurement data, yielding ratio maps of measured signals divided by simulated signals 2.ag.

The use of FP simulation is demonstrated to be useful in distinguishing between geometry effects and the real elemental composition of historical objects when performing in-situ XRF measurements. This approach enabled researchers to correct for surface curvature and tilt and to determine subtle pigment traces in ancient marble sculptures without the need for complex scanning methods. That said, careful assumptions about material composition are required, in this case, the variability in layer thickness, compositions, or roughness. Another limitation

is the lack of real-time analysis in compact form; the approach requires several specialised software programs for photogrammetry, XRF processing, and custom FP scripts, which are not standardised nor integrated into a single commercial software tool.

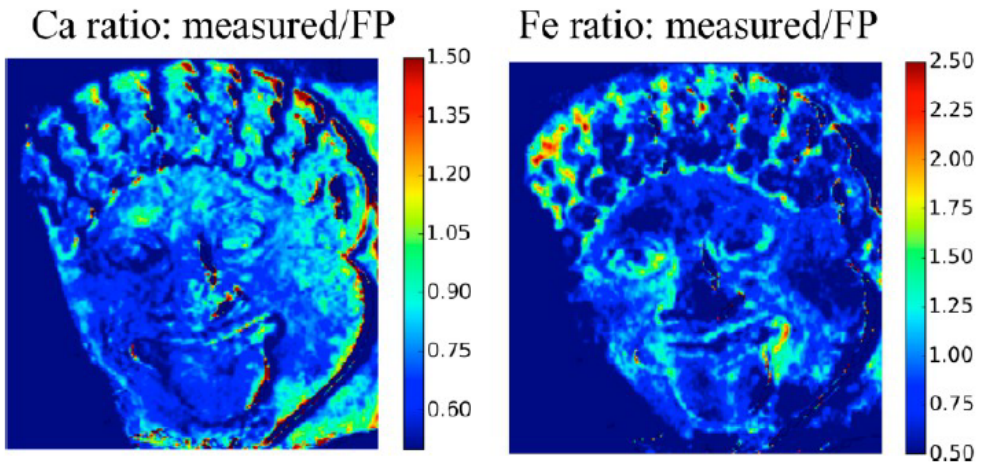

Figure 2.ag: Ratio of experimentally acquired elemental distribution images of Ca and Fe. A value above 1.0 indicates exposed surface marble, and a value below 1.0 indicates an absorbing layer on the surface [55].

2.5. Literature Review Discussion

The literature highlights the advancements in the application of MA-XRF for cultural heritage studies. The developments for this technique have been on two fronts: Firstly, mobile instrumentation setups have been developed and deployed for in-situ measurements, allowing valuable objects to remain in their ideal conditions and avoiding the risks and costs associated with transport. Secondly, data handling software and methods have been significantly improved, enabling the processing of datasets containing thousands of spectra into hyperspectral cubes that contain spatial elemental information of a sample area. While extensive research has been conducted on the use of XRF scanning in two dimensions on flat objects, such as paintings, there exists less research on three-dimensional scanning methods for non-flat objects.

The sample geometry has a pronounced effect on MA-XRF imaging, appearing as artefacts in the spectral data. Traditional methods of XRF imaging do not account for the variation in three-dimensional surfaces, producing data that contains artefacts due to the sample's geometry. Variation in working distance and tilt due to a sample's curved surface can attenuate elemental signals [56]. Methods using intrinsic data corrections, such as corrections based on the Argon profile due to X-ray absorption in the air, have been demonstrated for two-dimensional scanners. That said, this approach requires careful characterisation of the instrument, relying on clearly defined detection geometries and calibration of signals using a reference sample [56]. Additionally, the surface tilt is not accounted for when relying on intrinsic data features. Adaptive scanners utilising robots or motors have been introduced in the field to manoeuvre the scan head, ensuring it accounts for variations in working distance and sample tilt [57] [59]. These acquisition methods add additional degrees of freedom for XRF scanners, yielding more representative elemental data. That said, they tend to be more costly and are challenging to adapt to the existing two-dimensional scanning setup.

The current state of the literature warrants the continuation of research into MA-XRF scanning methods for three-dimensional objects. The use of 3D adaptive scanning methods utilising motorised stage platforms is notably absent from the proposed solutions found in the literature. The use of three platform stages is a straightforward adaptation from a standard two-dimensional axis scanning setup. It is also relatively simple to implement for a standard benchtop XRF scanner. This method of stage platforms is therefore investigated in this thesis, with the methodology being based on developing and testing a custom three-axis linear motorised stage instrument. The aim is to evaluate the solution by comparing 2D and 3D scans of the same target. This research opportunity is relevant for developing simple and more effective scanning solutions for geometrically complex cultural heritage objects.

3

Research Methodology

3.1. Problem Statement

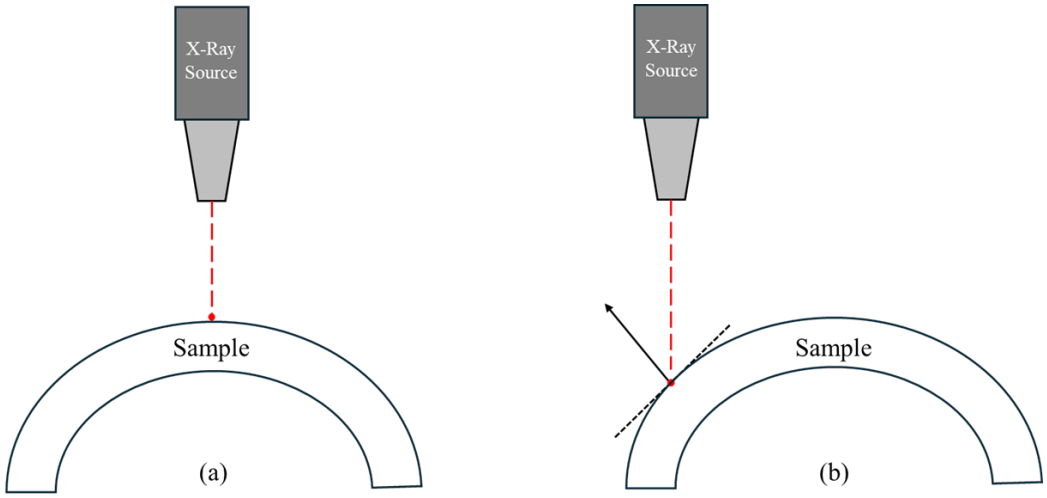

Figure 3.a: (a) Ideal detection geometry of a sample's surface, at the intended working distance. (b) Geometric effect of working distance and surface tilt, due to the sample's curved nature.

An important factor when performing Macro X-ray fluorescence (MA-XRF) analysis is the detection geometry between the sample and the scanning head. When studying objects of irregular geometry and curved surfaces using standard two-dimensional MA-XRF imaging, geometric effects arise due to inconsistencies in the detection geometry, as explained in Chapter 2.4.3. Figure 3.a summarises this problem in the case of a curved object. Situation (a) denotes the ideal detection geometry when scanning the top-most point of the sample surface. In this case, the acquisition is done with the intended working distance and geometry, where no surface tilt is present. When scanning the sample in two-dimensional scanning, situation (b) arises where the effective working distance increases due to a sample's curved surface. This effect attenuates the fluorescence signals and produces unwanted signals from elements

in the air. Another effect here is the surface tilt of the sample in relation to the scanning head, increasing the effective penetration in the sample and thus the escape path of fluorescence in the sample. The effect of geometry can present a challenge for researchers, especially in cases of MA-XRF for three-dimensional objects where scan areas extend across varying surface geometries, or when comparing related surface elements of different geometries.

3.2. Research Approach

Several solutions have been proposed, as outlined in Chapter 2.4.3, of instruments introducing additional degrees of freedom to the typical whisk-broom scanning method used in MA-XRF. Such adaptive scanning allows acquisitions which account for the geometric nature of the sample. Figure 3.b illustrates two scenarios that account for a curved sample. When the working distance is accounted for, as shown in (c), the absorption in the air is minimised; however, the surface tilt is not accounted for. The tilt effect is dealt with in (d), where the scan head tilts to maintain the ideal geometry.

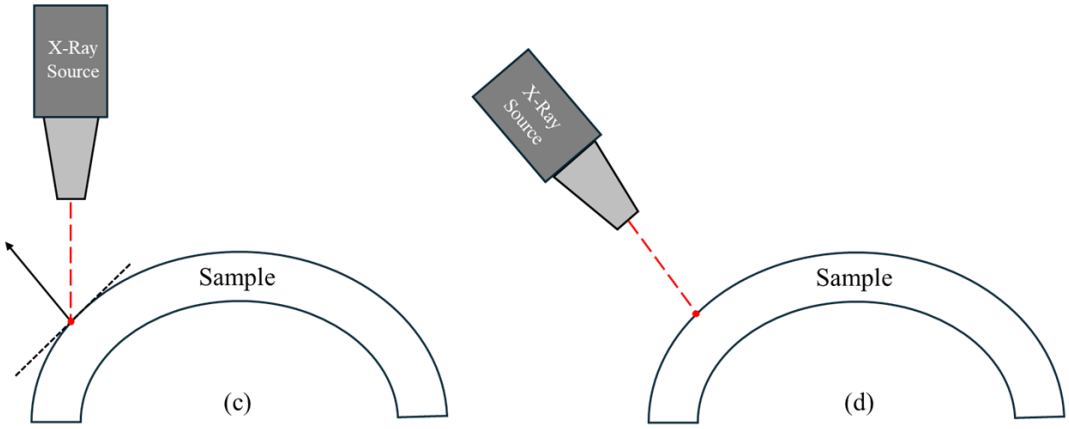

Figure 3.b: (c) A scenario where the working distance is accounted during measurement of a curved surface. (d) A better scenario where the tilt effect is also accounted for.

This project showcases a straightforward, albeit not simple, solution to scanning three-dimensional objects using a three-axis linear motorised stage instrument and a rotating stage. The addition of a third lateral degree of freedom allows for maintaining the working distance between the measurement head throughout the scan. Additionally, a rotating stage will be used during scans, accounting for the tilt effect. A mug was chosen as a test subject due to its cylindrical shape, which facilitates the straightforward generation of scan paths and repeatable scanning experiments. A typical flat scan of a mug surface presents the aforementioned geometric challenges in macro-XRF analysis, while three-dimensional scanning can account for them. To investigate mitigations approach to these effects, three scanning strategies, as seen in the figure 3.c, were performed on one half of the mug's outer surface:

1. **Two-dimensional Scan:** The first scan type serves as a baseline for the other experiments. Engaging only X and Y motors, a conventional two-dimensional scan can be performed across the projected mug surface. The effective working distance varies across

the face of the mug, increasing by the radius of the mug when scanning the edges. The scan path is a ”snake” patterns, following a continious line throughout the scanning procedure.

2. **Three-dimensional Scan:** This scan conforms to the curvature of the mug, following a scan path which maintains a fixed working distance. In this case, the scan path engages the Z motor, which forwards and retracts the scan head such that it follows the cylindrical profile of the object. The scan also follows a snake path.
3. **Rotating Stage Scan:** Utilising a rotating stage, this scan performs scans across each of the mug's columns; the X and Z positions are fixed, while the Y motors execute a linear scan on each column. The use of a motorised stage ensures uniform coverage and a consistent scan geometry when acquiring data, maintaining both the working distance and the surface tilt across the sample.

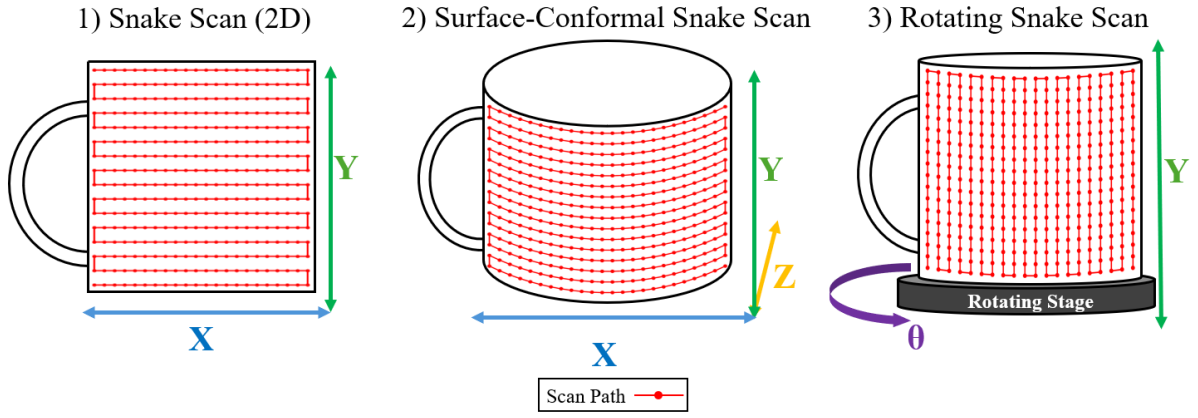

Figure 3.c: Three Scan strategies.From left to right: 2D scan, 3D scan, and a rotating stage scan. The latter two scans account for the geometric nature of the mug.

All scans will be point-scan measurements, where acquisition is performed at each point along the scan path, and the scanner rests during the scan. These scanning strategies aim to demonstrate scan artefacts due to the curved nature of the sample object, and the effect of mitigating them by maintaining a fixed working distance and/or surface tilt. The end goal of these experiments is to assess directly the viability of using a three-axis system in improving spectral clarity, reducing signal attenuation, and providing consistent, repeatable measurements.

4

Methods

4.1. Experimental Setup

To implement the scanning strategies introduced in Chapter 3, a custom three-axis linear motorised stage instrument was designed to achieve surface-adaptive scanning of curved objects. The instrument mounts a scanhead consisting of an X-ray tube and a solid-state detector; additionally, the scanhead mounts a Dinolight microscope camera for image capturing. Accompanying code was written to generate scan paths, control the motors, and trigger the detector acquisition. The software writes the data into HDF5 files, creating hyperspectral data cubes, which are in turn processed and fitted to produce elemental maps. The following section details instrumentation and software developed for this project.

4.1.1. Instrumentation

The three-axis linear motorised stages instrument, named ”BLB MK 2.1”, was designed, constructed, and programmed to acquire Macro X-ray Fluorescence (MA-XRF) measurements along curved surfaces of 3D objects for cultural heritage. BLB MK 2.1, shown in figure 4.a, is a modification of a two-dimensional scanning setup, consisting of two linear stages mounted with a right-angle bracket placed on top of a third linear motorised stage to introduce an additional degree of freedom.This configuration of motors allows for the scan head to move in the Z axis (towards or away from the object surface) during a typical scan loop in the X-Y plane. The instrument carries a scan head consisting of an X-ray tube and a solid-state detector (SSD). A Dino-light microscope holder is also attached to the scanhead plate, allowing for the imaging of the sample’s surface. The instrument is housed in a lead boxed designed for the previous insturment (a two-dimensional XRF scanner), where each wall consists of two aluminium sheets, 1 mm thick, sandwiching a 0.8 mm lead sheet. When closed, the box door triggers a safety interlock directly connected to the X-ray tube’s operation. The designated purpose of the instrument is to carry out investigative MA-XRF measurements of curved objects and demonstrate the effectiveness of mitigating geometric effects.

Motorised Stages

The movement stages used are ThorLabs's LTS300C/M, a 300 mm linear translation stage with an integrated controller and a stepper motor (Shown in Figure 4.c). The travel range of 300mm in each axis covers a reasonable range for moderately sized objects, with the motors allowing a minimum achievable incremental movement of 0.1 µm. Maximum velocities are 50 mm/s for horizontal movement and 3 mm/s for vertical movement. The load capacities and velocity specification for the motors are easily sufficient for this application, since the instrument is intended to perform point-by-point acquisition of XRF spectra at moderate speeds whilst carrying a lightweight (kg) scanner part.

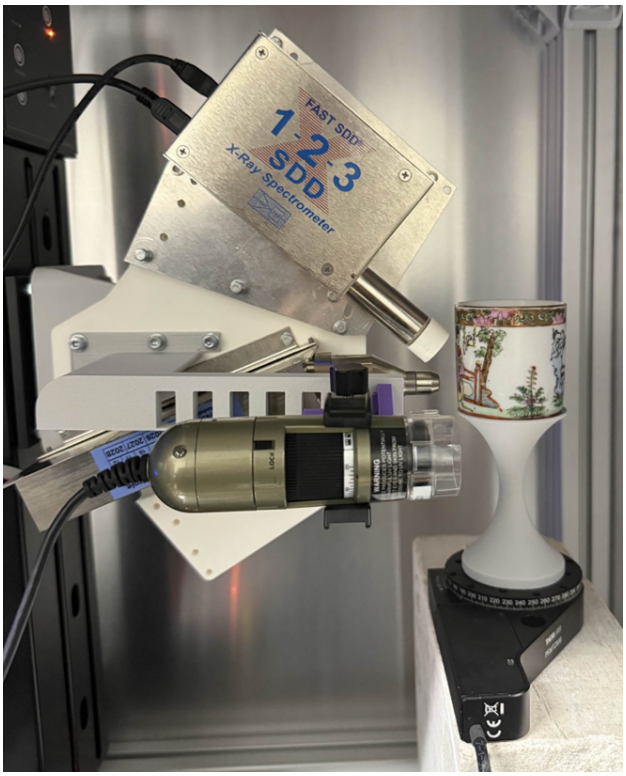

Figure 4.a: Side view of BLB ML2.1 inside the lead box, showcasing the detection head, the offset Dinolight microscope, the rotating stage, and the mug placed on a pillar seat.

The motorised precision rotation stage model from Thorlabs, PRMTZ8/M, is used for rotating scan measurements. Shown in Figure 4.a, the entire experimental setup places the mug on a platformed seat (3D printed with PLA), which is inserted in the top holes of the circular stage. The precision rotation stage, similar to the Thorlab stage motors, can be controlled directly via Kensis or its own code wrapper. Additionally, the stage comes with a KDC101 K-Cube servo motor controller, which enables direct rotation of the stage without the need for software.

Scan head

The scanner part of the instrument consists of a scan head plate which allows for the mounting of an SSD detector, an X-ray tube, and the dinolite microscope. The scanner head configuration and design were taken from the previously built 2D MA-XRF scanner, and modified by incorporating an L-bracket to mount the scan head plate to the Y motor's stage platform. Ad-

ditionally, a Dino Lite microscope holder extension was designed and fitted, allowing for the microscope to be mounted and aligned alongside the X-ray tube's head at a 100 mm offset. The addition of the Dino-Lite microscope enables digital imaging of the scanned object. It can also be used to verify positioning using a fixed-depth-of-focus approach (explained in Section 4.2.1). The detector used the Amptek FAST SDD®, a high-performance silicon drift detector. The throughput is relatively high, handing over 1 million counts per second. The energy resolution is at 123 eV FWHM at Mn Kα (5.9 keV). The provided low-noise and sensitive detection is ideal for a basic benchtop spectroscopy instrument. The X-ray tube used is a 50 kV Mini-X2 Amptek X-ray Tube System consisting of a Rhodium anode and a 125 µm Berreliym (Be) window. The X-ray was operated at a current of 200 µA and a voltage of 30 kV. The X-ray tube is initiated and activated on a separate device, connected to the interlock system in the lead box. The detection geometry is sketched in Figure 4.b, where the detector is positioned above the X-ray tube to record the intensity and energy of the emitted X-rays. The take-off angle between the sample surface and the detector path is at 40° relative to the incident beam.

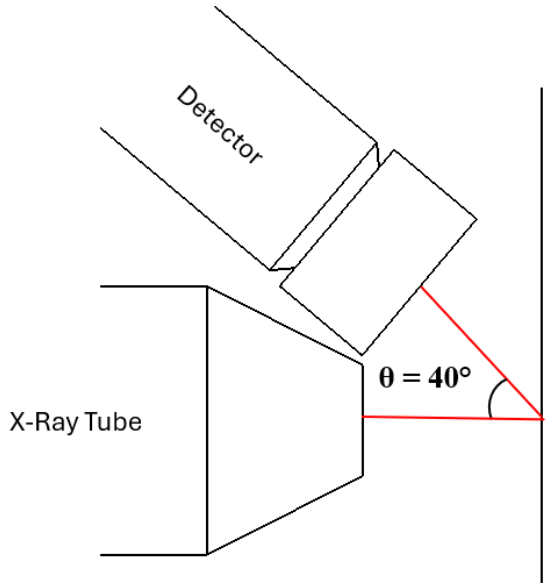

Figure 4.b: Schematic of the XRF detection head setup. The detector is oriented above the X-ray tube, with the take-off angle at θ = 40°.

4.1.2. Software

The control software performs an entire scanning routine of the mug's face. It handles all tasks, including scan path generation, linear stages motor control, spectra acquisition, and logging data. The code compiles the generated spectra and detector statistics into an HDF5 (.h5) file, compiling all the data obtained during the scan. The code was developed in Python and run using the integrated development environment, Spyder.

Reference Point

In the software, the scan trajectories are defined relative to a reference coordinate located on the closest column to the scan head, at the midpoint of the mug's height. Therefore, before

running the scanning script, the position of this reference point was determined in the form of three absolute coordinates of the three-stage motors. Kensis (ThorLabs motor control software) was used to control the motors and the rotating stage at this point, allowing the X-ray tube head to be manually positioned to the reference point measured with callipers.

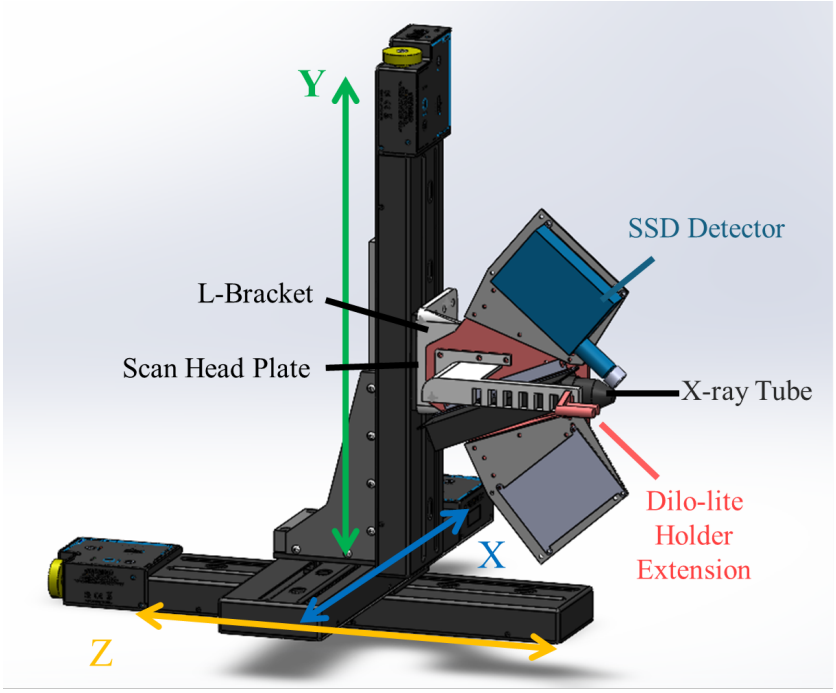

Figure 4.c: 3D Schematic of BLB MK2.1, showcasing the three motors and the scan head, which includes the X-ray tube, SDD detector, and the Dinolight Microscope holder.

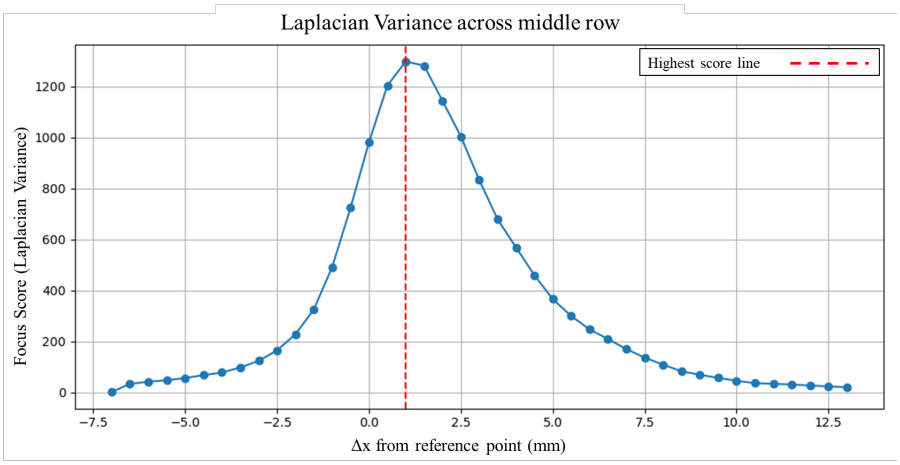

Figure 4.d: Laplacian Variance focus score as a function of horizontal displacement across the central row of the mug. The maximum sharpness x position is determined to be 1.15 mm to the right of the current reference point.

The Dinolight microscope's limited depth of focus was also used to confirm the position of the reference point. Images are captured across several rows of the mug, and a focus score is computed based on the Laplacian operator, a standard method in image processing that determines the sharpness (or blurriness) of an image. The variance of the Laplacian value,

obtained using the OpenCV Python package, was computed during horizontal imaging. The Laplacian score is determined based on the clarity of edges or texture, which produces strong Laplacian responses. Computing the focus score across the mug's surface allows for selecting the most "sharp image," which corresponds to the column closest to the scan head (Figure 4.d).

One must be careful when performing this test, however, since the most "in-focus" position depends on the fixed depth of focus set by the microscope; the focal plane may happen to lie slightly behind the closest point on the mug surface. The depth of focus, therefore, is set such that the plane of focus is in front of the theoretical reference point. Additionally, the middle well-focused region of the mug was broad (2.5 mm) due to the finite but not infinitesimal depth of focus. That said, confirmation of this middle point along the X-axis was validated by hands-on measurements, as well as by the obtained XRF spectra across several rows of the mug, which allowed for the computation of the Argon_k signals and the determination of the point with the minimum signal measured. The reference is finally determined on the XY plane; a slight margin of error is acceptable since the chosen exact scan area in that plane is not too important as long as it covers the entire length of the mug in the spectral image. Finally, a working distance of roughly 9 mm was then measured using a labelled string while adjusting the Z motor. This value of working distance was chosen for the scan head since it uses the same scan head plate configuration as the previous instrument.

Scan Path Generation

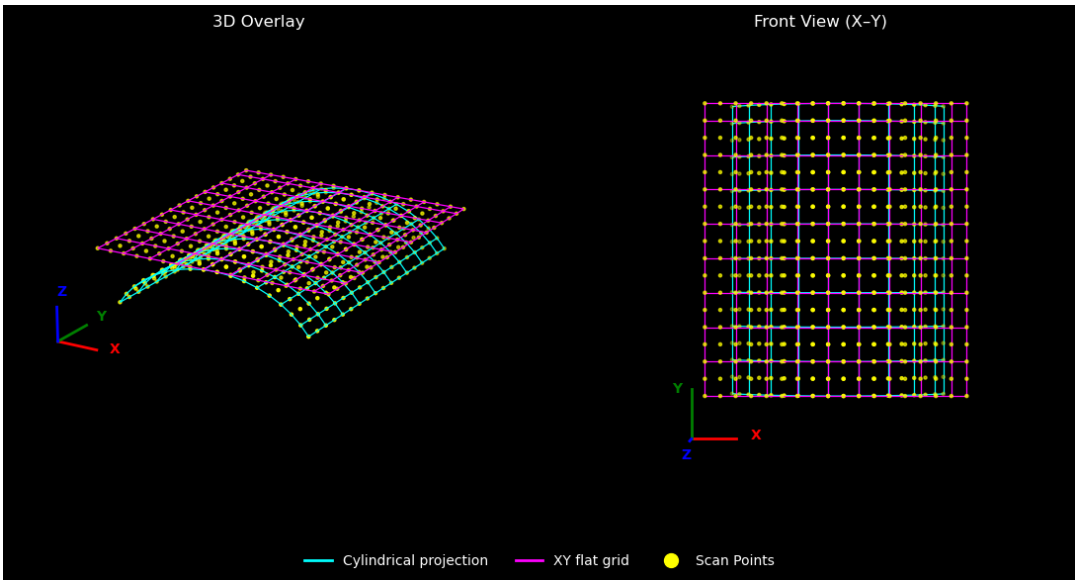

Figure 4.e: 3D sketch illustrating how a flat grid maps onto the curved surface, creating the scan grid.

The code generates a scan path needed to perform each scanning method, and the subsequent motor coordinates that are applied to manoeuvre the scan head along the scan path of a curved mug. This is achieved by projecting a canonical flat grid, where scan points are spaced by 1 mm and the origin point (0, 0) corresponds to the reference point in (u, v), onto a mug's cylindrical surface. (as is shown in Figure 4.e). The step size is defined in the flat (u, v)

grid, with increments of $\Delta u = 1$ mm and $\Delta v = 1$ mm. In the vertical direction (v), steps remain unchanged, since this corresponds directly to motion along the height of the cylinder. In the lateral direction (u), however, the scan points spacing is equal to 1mm arc length on the cylinder but not 1 mm in real space; when viewed in Cartesian X, the effective step size appears smaller near the edges and larger at the centre columns. The computed grid thus acts as a canonical sampling lattice, where any scanning method adheres to the same columns on the mug surface, allowing for a direct comparison of scanned columns and rows.

Since motor movements are in real space, real coordinates must be computed directly from the projection. The scanning order is chosen to start at the top-right corner of the grid and follow a snake-like path; the same path applies to the rotating scan, scanning columns then rotating the equivelant of 1 mm arch length. the motor coordinates for each scanning mode are calculated as follows:

a) Two-dimensional Scan

$$x = x_{\text{ref}} + R\sin\left(\tfrac{u}{R}\right), \qquad y = y_{\text{ref}} + v, \qquad z = z_{\text{ref}}$$

(b) Three-dimensional Scan

$$x = x_{\text{ref}} + R\sin\left(\tfrac{u}{R}\right), \qquad y = y_{\text{ref}} + v, \qquad z = z_{\text{ref}} - \left(R - R\cos\left(\tfrac{u}{R}\right)\right)$$

(c) Rotating Stage Scan

$$x = x_{\text{ref}}, \qquad y = y_{\text{ref}} + v, \qquad z = z_{\text{ref}}, \qquad \theta(u) = \frac{u}{R}$$

with,

$$\Delta\theta = \frac{s}{R} \cdot \frac{180}{\pi},$$

Where (u) is lateral offset (arch length in mm), (v) is vertical offset (in mm), R is the mug radius and x_{ref}, y_{ref}, and z_{ref} correspond to the reference coordinates in Cartesian space. θ is the rotation angle applied by the stage, and s is the step size in the flat grid, set in this code as $\Delta u = \Delta v = s = 1$mm. This code then plugs in the selected scan area as length, L, and height, H, to define the extent of the grid:

$$u \in \left[-\tfrac{L}{2}, +\tfrac{L}{2}\right], \qquad v \in \left[-\tfrac{H}{2}, +\tfrac{H}{2}\right],$$

In the code, once the reference point is loaded and scan paths are processed, indexes of each step count (totalling u x v) are generated, and each motor position is calculated.

Motor Control

A Thorlabs wrapper is used to control the motion of the three-stage motors. Motors, identified by their individual serial numbers, are detected via USB and assigned to X, Y, and Z; then they are homed to their zero positions before the scan begins. To avoid collision with the lead box housing, homing the motors is done in the order of X, Y, and then Z. Once the motors are homed, the scanning begins with movement commands performed as absolute moves in the sequence of the scan path, with short rest times between moves to ensure system stability and sufficient spectral acquisition time. The control code also enforces predefined travel limits to avoid collision with the lead box housing the instrument. The total scan volume allowed by the instrument is:

$$(x, y, z) \in [0,\, 290] \times [0,\, 90] \times [0,\, 150] \text{ mm}$$

The scanning procedure is interrupted if the motion sequence crosses the defined limits. Error handling and resource management are programmed into the script through try/except/finally blocks, ensuring that scan interruptions are handled safely, with all motors and the detector shutting down safely.

Data Collection

Scans are executed point-by-point, with the Amptek detector triggering for a fixed measurement time at each scan point. The acquired spectra are processed and written to disk in CSV format, with indexed spectra filenames according to the scan order. While acquisitions take place, a log is compiled by the software, containing records of step size, total counts, and rest time during acquisitions. Additionally, the log stores detector data related to the detector, such as the measured voltage applied to the detector, the detector crustal temperature, and the electronics board temperature. The code generates a directory of the scan session, containing all the acquired spectra and scan data, providing a complete record of the measurement run. When the Dino-lite microscopy was used to capture images, it was moved by a known fixed offset of 10.2 mm to the right of the X-ray tube in the X-direction during the scan, and the images were saved in a separate directory.

HDF5(.h5) file creation

The collected raw XRF data is processed as a series of individual spectrum files, where each measurement point corresponds to a full spectrum in CSV format.The code reads the scan log of each scan session to determine the grid layout, number of channels, and pixel order, ensuring that spatial order is preserved when creating the hyperspectral cube. The spectra are then loaded into memory and written into three-dimensional arrays to store the data sets (such as channel counts, detector status etc..) in the correct position of the data cube. The complete scan is written in HDF5 format, compacting full spectral information, pixel positions, and associated metadata into a single file. Subsequent fitting and elemental visualisation routines can then be done on the said HDF5 files, accessing spectral data across the scanned area.

4.2. Experimental Procedure

The experimental procedure involved conducting different scan tests on the same three-dimensional object. Experimental scans were done with the instrument on a decorative glazed mug, shown in Figure 4.f, obtained from a second-hand store. The cylindrical shape deems the test sample helpful in testing the different scanning strategies and observing the effect of surface curvature on the XRF acquisitions.

Figure 4.f: Front face of the decorative mug, chosen as the test sample for scans in this project.

4.2.1. Sample Description: A decorative mug

The sample's shape is a standard mug with a handle, and an illustration repeated on opposite sides of the outside surface. The ceramic mug, with a diameter of 50.2 mm and a height of 53.2 mm, features a smooth, glazed exterior surface with a decorative layer applied on top. The mug decoration is made of thin ceramic enamel, depicting a scene of a lady in a dress seated in a garden surrounded by green foliage, and to her left sits a bird on a hanging stick. On the far left, a tree truck with leaves is present, and on the far right, a blue structure is noted. Many colours are present in the illustration: Her dress is painted pink and red with streaks of yellow, while the bench is a combination of blue and brown. A gold-coloured strip is seen under the rim of the mug with pink flowers and green leaves painted on top. A warning label is printed on the bottom of the mug, advising against consuming the contents due to the presence of harmful materials.

Before the start of the project, preliminary 2D XRF scans were conducted on the mug to investigate its composition and build-up. Many features of the mug can be observed from elemental distribution maps, shown in Figure 4.g. For instance, silicon (Si) has a higher presence in areas around the paint, as it is a primary material in clay silicate. Gold (Au) is visible on the mug's rim, interrupted by the paint. And iron (Fe) is used as a colourant for the reds and browns, while cobalt (Co) is used in the hair, and so on. The argon K (Ar-K) signal is due to the excited argon atoms present in the air between the sample and detector. The intensity corre-

sponds to the curvature around the mug, showcasing the effect of varying working distance on the attenuation of this signal. Visual inspection alongside the elemental maps obtained from preliminary tests helps explain the makeup of the ceramic decorative mug. A mug's body is made of clay mixed with silica, which is fired to create a hardened body. A layer of glaze, likely containing silicates, is then applied. Finally, the picture on the mug appears to be decorated with pigment enamel, found in the lady's hair and dress, as well as a metallic overglaze, evident in the cup's rim. The full elemental list is showcased in section 4.3.1.

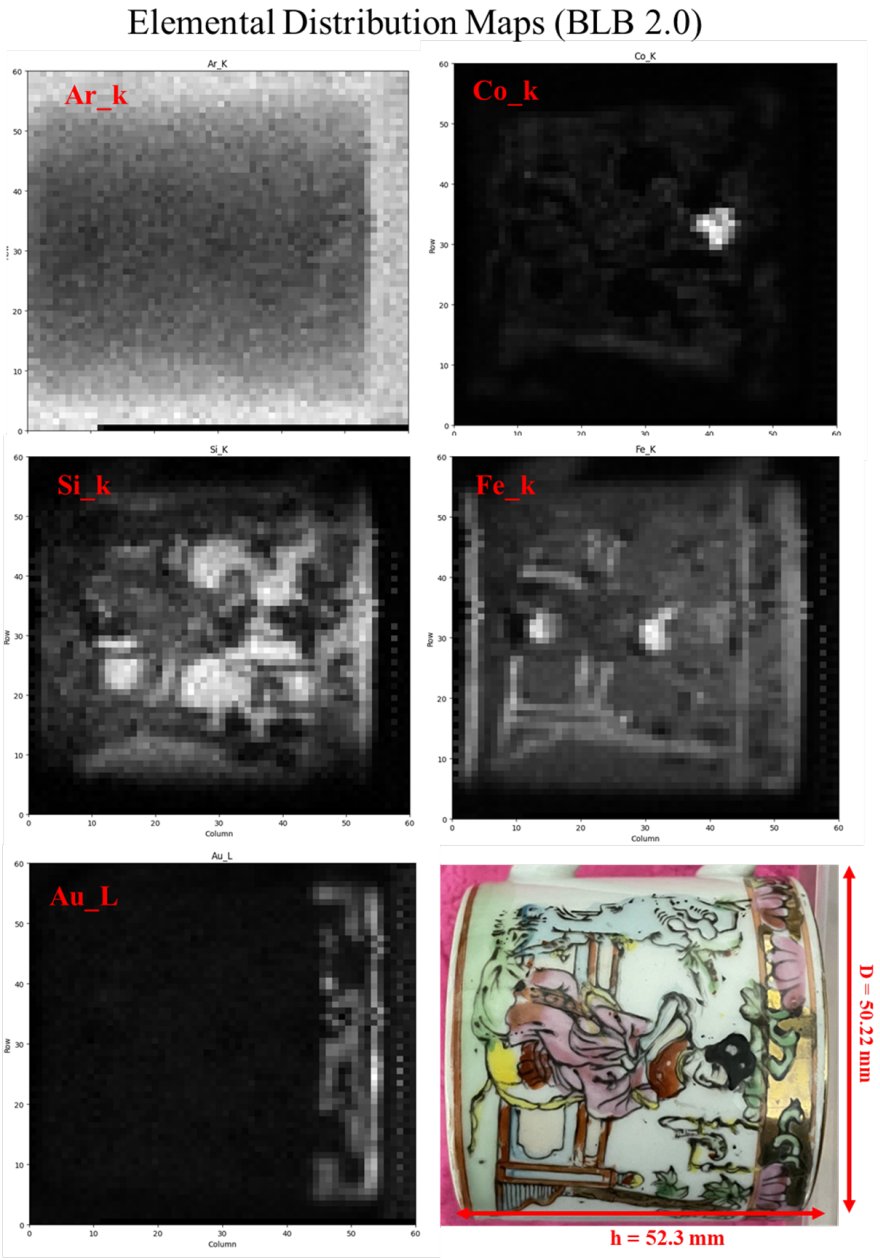

Figure 4.g: Elemental Distribution Maps of Argon, Cobalt, Silicon, Iron, and Au, alongside an image of the mug. The scans were obtained using a raster scan with BLB 2.0 and processed in PyMCA.

4.2.2. Experiments

Four point-by-point XRF scan experiments were conducted using the BLB MK 2.1 on the test mug. Before each scan, the homing procedure described in section 4.2 was followed. The scanning area, measuring 55 x 54 mm^2, was kept constant in all four experiments, but measured with scanning strategies outlined in section 3.2. The scan steps of X were 1 mm in arch length, and the scan steps of Y were 1 mm in the vertical direction, adhering to the projected shape of the cylindrical mug. The X-ray tube was controlled on a separate device, set to 200 kV and 30 A, and the rest time between scan points was 1 s. The following table in Figure 4.h summarises the four experiments:

Scan Type	ID	Working Distance	Motors Used	X-ray Tube Current	X-ray Tube voltage	Scan Area	Total Scan Points	Rest Time (at scan points)	Scan Duration
Two-dimensional	2D Scan	9 ± 0.5 mm at central column. (Varies along rows)	X, Y	200 µA	30 kV	54 x 55 mm (arc length × height)	2970	1 second	1 hr 31 min
Two-dimensional (+3 mm to working distance)	2D Scan (Z +3 mm)	12 ± 0.5 mm at central column. (Varies along rows)	X, Y	200 µA	30 kV	54 x 55 mm (arc length × height)	2970	1 second	1 hr 31 min
Three-dimensional	3D Scan	9 ± 0.5 mm	X, Y, Z	200 µA	30 kV	54 x 55 mm (arc length × height)	2970	1 second	1 hr 42 min
Rotating Stage	Rotating Stage	9± 0.5 mm	Y, Rotation Stage	200 µA	30 kV	54 x 55 mm (arc length × height)	2970	1 second	1 hr 33 min

Figure 4.h: A summary of the experiment parameters for each XRF acquistion conducted with BLB MK 2.1

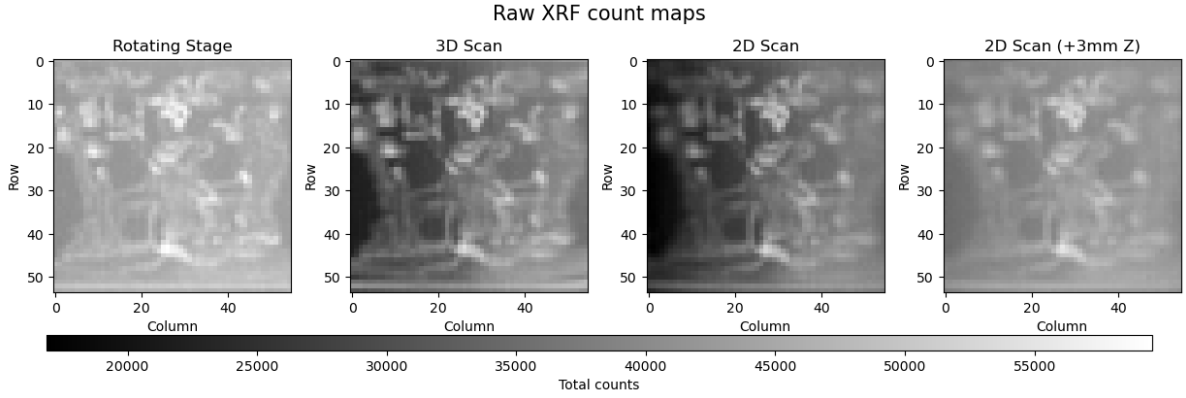

Figure 4.i: Raw XRF total count maps for all the scans.

4.3. Data Handling

After the data were acquired and converted into HDF5 files, the spectra were loaded in PyMCA for quick inspection. When examining the raw stacked count maps, shown in Figure 4.i, it is immediately apparent that the count totals appear to increase throughout the scan (the scan path being a snake path column-wise starting on the top left), more prominently in the 3D scan and the 2D scan. This effect was suspected to be due to variations in the detector's response throughout the scan. After inspecting the detector status data in the spectral cube, a noticeable

drift in detector temperature was observed during the scans, as shown in Figure 4.j. This drift seems to have caused the observed gradient in total counts. It is acknowledged as a detector artefact, and its effects could be a source of bias when interpreting the data.

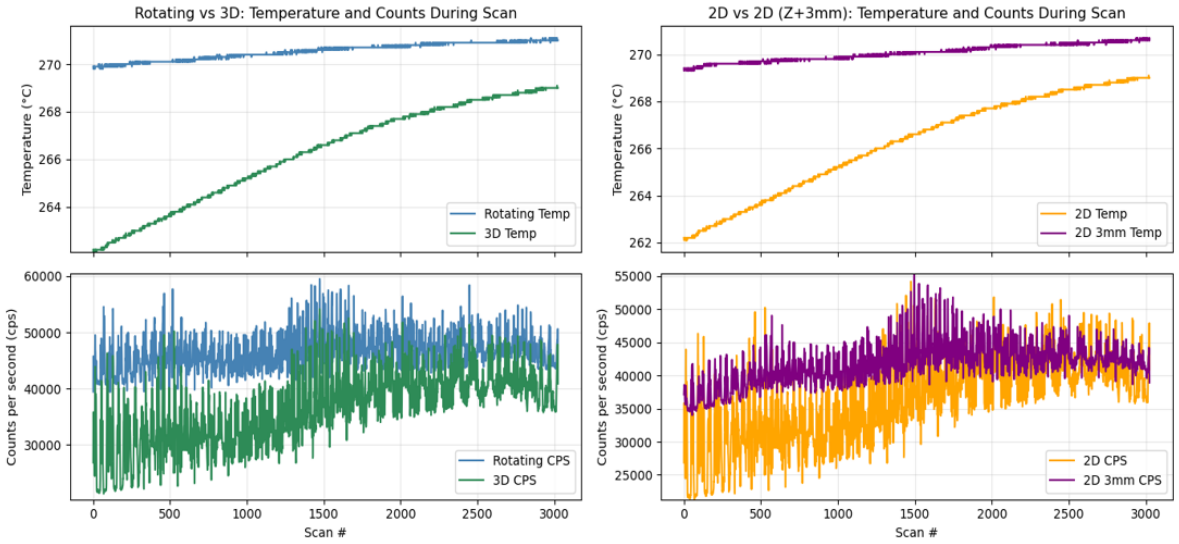

Figure 4.j: Plots of detector temperature and total counts per second for each of the scans, showcasing a drift in detector response. A significant increase in temperature is observed, most prominently in the 3D and 2D scans, which seems to correspond to a gradual rise in count totals.

4.3.1. Data Fitting

The hyperspectral data were stitched together for the purpose of fitting the data and producing comparable elemental maps. Fitting the data involves decomposing the measured spectra into their underlying components. Raw spectra contain characteristic peak elements, background signals, and detector artefacts that must be accounted for when inspecting the data. Additionally, overlapping features must be carefully resolved. This process is done by applying background subtraction, estimating peaks, and correcting for detector responses. Once a good fit is achieved, the data is processed by batch fitting, applying the configured fitting to the whole set of spectra automatically. The fitting was also used in 'Fast Linear Fit' mode using different weighing policies. Finally, net intensities of each present characteristic X-ray line were determined across each pixel on the scan grid of the data cube, and elemental maps were produced.

Fit Configuration

The fitting process begins with creating a fit configuration on PyMCA; for this, the stacked spectrum was chosen as the representative of the data. The stacked spectrum is a quick way of checking peak mismatch and configuring the overall fit. The elemental peaks were identified in the representative spectrum (or stacked spectrum) of the dataset using the Advanced Fit tool. Known elemental peaks are verified by toggling their characteristic X-ray lines in the peak selection window, and the fit is manually checked during the process to confirm the selections. This process is illustrated in Figure 4.k, where chromium and iron, identified by

their signature energy peaks, are toggled. Preliminary scans during characterisation of the mug aided in determining the list of present elements.

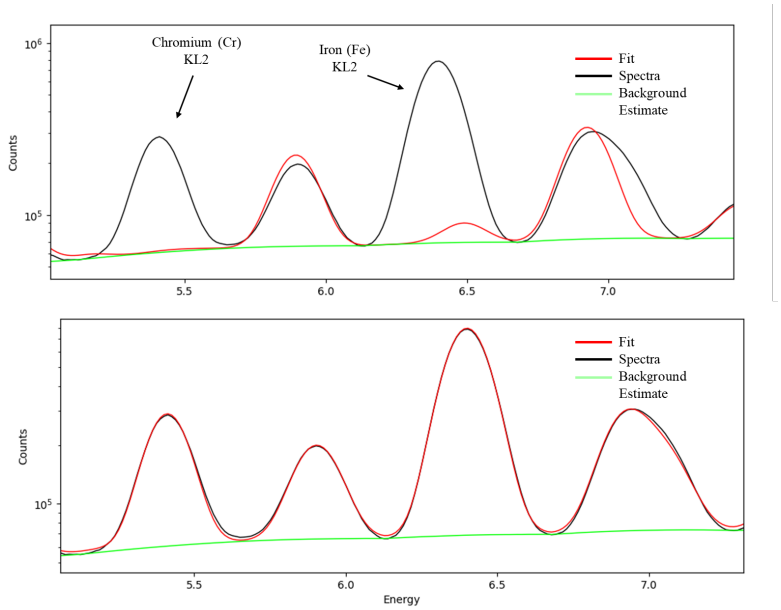

Figure 4.k: Pymca Advanced Fit tool preview. Top: stacked data fit without including Fe and Cr peaks. Bottom: After toggling Fe and Cr peaks.

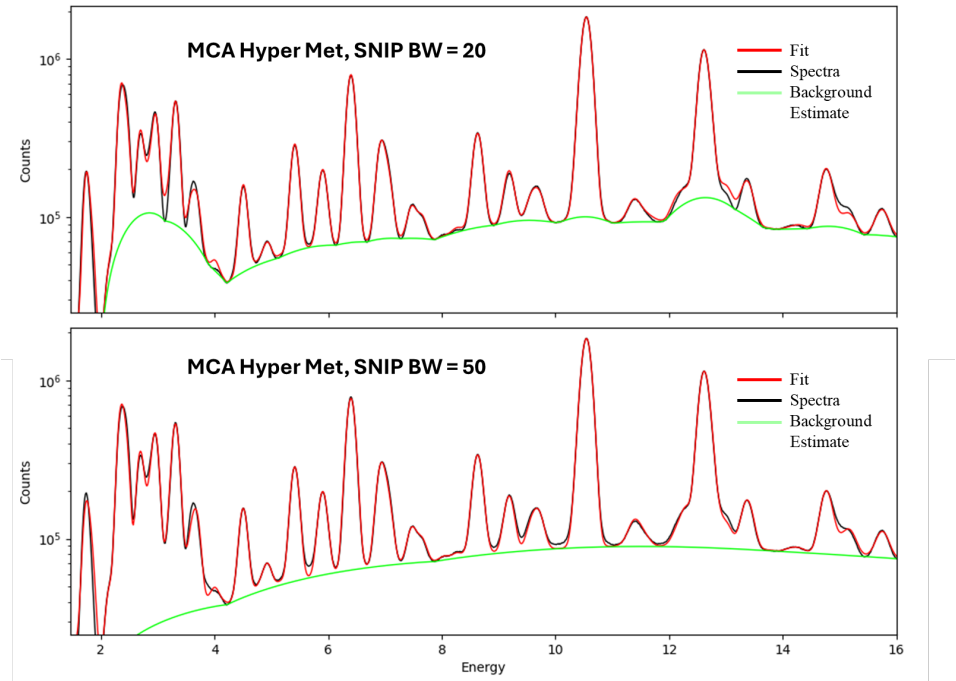

Figure 4.l: Demonstration of MCA Hypermet fits onto the representative spectrum with SNIP algorithm to estimate background. The effect of the SNIP background width (BW) parameter is shown: (top) BW = 20 and (bottom) BW = 50. A narrower BW follows peaks more closely, while a wider BW smooths the continuum.

Once all the elemental peaks were determined, the fit parameters were optimised to match the found peak shapes. The MCA Hypermet function, PyMCA's peak shape model, was chosen as the fit function. Hypermet takes into account both the Gaussian shape expected from

the detector resolution and the low-energy tails that appear due to incomplete charge collection. Figure 4.l illustrates the operation of the Hypermet function on a representative spectrum. The figure also showcases the background estimation; the background was modelled using Sensitive Nonlinear Iterative Peak-clipping (SNIP), where the baseline background was estimated. The SNIP algorithm applies a progressive estimation of a smooth underlying background beneath the peaks by clipping away sharp features. SNIP's background width parameter determines how broad the smoothing window is: if set too narrow, the baseline is too close to the peak, undermining its intensity. If set too wide, this could result in oversmoothing and cutting of peaks. Figure 4.l shows the effect of SNIP background width (BW) on the background continuum. The SNIP background width was iteratively adjusted until the background estimation seemed appropriate, ensuring that the elemental peaks could be accurately separated from the continuum.

Finally, counting statistics were determined using Poisson (1/Y) weighting, with 40 iterations allowed at a stopping criterion of a minimum χ^2 difference of 0.001%. Poisson weighting is set such that channels with higher counts are more statistically significant, and therefore weigh more strongly during the fit. Iterative fitting is governed by , a statistical measure of the quality of the fit, calculated from the difference between the raw data and the model and scaled to match expected statistical uncertainty in each channel. Lower values indicate that a fit resembles the data closely, while larger values suggest a mismatch, unresolved peaks, or inaccurate background estimation.

Table 4.a summarises the fit configuration; the resulting fit can be seen in Figure 4.m, showcasing the elemental peak positions. The listed elements are interpreted to be part of the mug's ceramic body, enamel, and glaze. Argon is the contribution from the air between the scanner and the sample, whilst rhodium comes from the anode.

Parameter	**Value**
Fit function	MCA Hypermet (No continuum)
Background algorithm	SNIP (BW=30)
Statistical weighting	Poisson (1/Y)
Number of iterations	40
Stopping criterion	Minimum χ^2 difference of 0.001%
Fitting region	Channels 123–1284
Corrections included	Stripping, Escape peaks, Short tail
Fitted elements	**Si**_K, **S**_K, **Cl**_K, **Ar**_K, **K**_K, **Ca**_K
	Ti_K, **V**_K, **Cr**_K, **Mn**_K, **Fe**_K, **Co**_K
	Ni_K, **Cu**_K, **Zn**_K, **As**_K, **Se**_K
	Rb_K, **Sr**_K, **Zr**_K, **Rh**_L, **Sn**_L
	Ba_L, **Au**_L, **Au**_M, **Pb**_L, **Pb**_M

Table 4.a: PyMCA fit configuration and fitted elements used in the analysis.

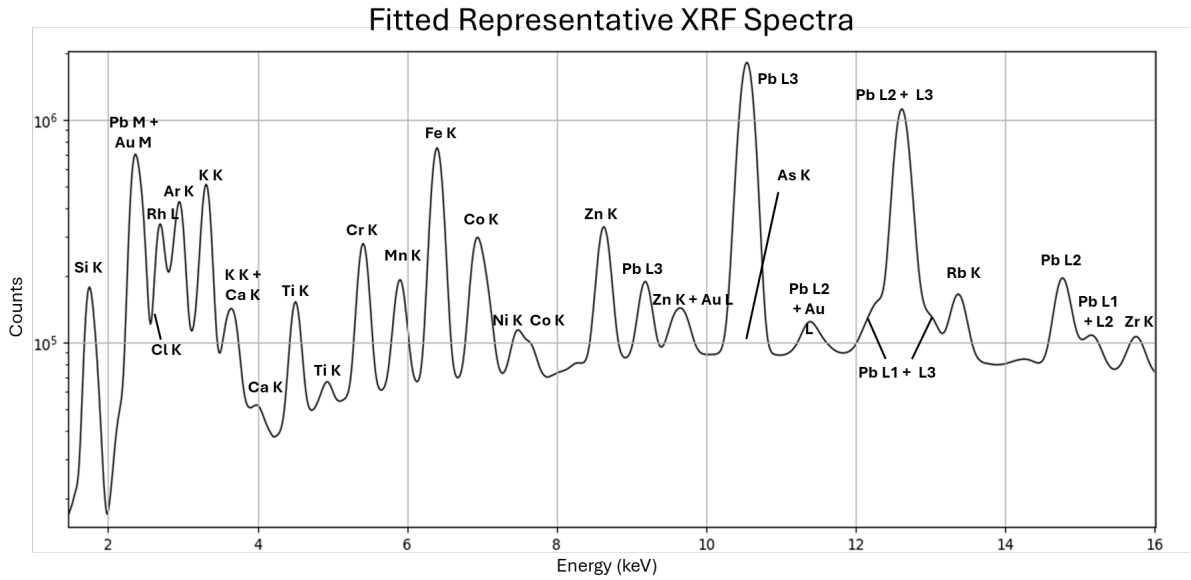

Figure 4.m: The final fit of the representative XRF spectra. Elemental peaks are labelled.

Element	Line(s)	Notes
Si	K	Ceramic/glaze matrix
S	K	Trace element
Cl	K	Impurity
Ar	K	Air path contribution
K	K	Flux in glaze or clay
Ca	K	Flux or stabiliser
Ti	K	Clay impurity
V	K	Trace component
Cr	K	Pigment (hair)
Mn	K	Pigment (brown/purple)
Fe	K	Pigment (dress, bench)
Co	K	Pigment (blue)
Ni	K	Trace in glaze
Cu	K	Trace in glaze
Zn	K	Flux or stabiliser
As	K	Trace in glaze
Se	K	Trace in glaze
Rb	K	Raw material trace
Sr	K	Flux in glaze
Zr	K	Opacifier
Rh	L	Tube anode
Sn	L	Opacifier (tin oxide)
Ba	L	Flux in glaze
Au	L, M	Decoration (rim)
Pb	L, M	Glaze flux / pigment

Table 4.b: Characteristic XRF emission lines and the role of detected elements.

Batch Fitting

Batch fitting is the process of fitting every spectrum in the data with a single fitting model (in this case, the model configured in the previous section). This was done using PyMCA's batch fitting tool, which loops through the entire data set and automatically applies the fitting, extracts peak areas for each element, and saves them in a results file. While this allows for mass fitting of a large amount of data, any errors present in the model will manifest in the entire dataset, resulting in a mismatch.

Once the fitting was applied to the data, the quality of the fit can be checked by examining the residuals (i.e., the differences between the measured spectrum and the fitted model) across all channels. Residual maps show areas of over- or underestimation of the signal, allowing for the identification of poorly fitted regions. Additionally, the variance across the fit is examined by computing the χ^2 statistic, which measures how well the fit matches the data. The residual maps, seen in Figure 4.n, are defined as:

1. RMS Residuals

$$r_i = y_i^{\text{measured}} - y_i^{\text{fit}}, \quad \text{RMS} = \sqrt{\frac{1}{N}\sum_{i=1}^{N} r_i^2}.$$

With r_i being the raw difference between the acquired and fitted counts (y_i^{measured} and y_i^{fit} respectively) across the channels (indexed with i). The root mean square for each pixel is then computed by summing across channels (totalling N). This calculation does not account for statistical noise, thus regions with counts tend to dominate in count.

2. RMS Standardised Residuals

$$z_i = \frac{y_i^{\text{measured}} - y_i^{\text{fit}}}{\sigma_i}, \quad \text{RMS standardized} = \sqrt{\frac{1}{N}\sum_{i=1}^{N} z_i^2}.$$

Here, the residuals are divided by the statistical error, $\sigma_i \approx \sqrt{y_i^{\text{measured}}}$, producing a dimensionless value z_i. The deviations in this case can be compared across pixels, showcasing systematic misfits more clearly.

3. χ^2 Statistic

$$\chi^2 = \sum_{i=1}^{N} \frac{\left(y_i^{\text{measured}} - y_i^{\text{fit}}\right)^2}{\sigma_i^2}.$$

χ^2 is calculated by squaring the raw difference between the measured and fit counts, then dividing by $\sigma_i \approx \sqrt{y_i^{\text{measured}}}$; the sum in this case accounts for the statistical weight of each channel. A reduced ^{2} value near 1 indicates that the fit is well consistent with counting statistics. In contrast, higher values indicate a mismatch or missing model component (for instance, missing elements in the fit configuration).

When observing the raw residual map, it can be observed that the areas with high difference correspond to high count regions (seen on figure 4.i). These regions align with the painted enamel placed on the mug. The result of adhering to counting statistics is evident on the standardised residual map, where the structures seen in the raw maps are less pronounced. After normalising, the values mostly fall within the range of 1-2 across the map, suggesting a good enough fit. The slight mismatch is likely due to peak overlap or background handling.χ^2 distribution across the scan shows no extreme mismatch between the fit and the values. This is confirmed by the histogram of χ^2 distribution across all the scans, shown in Figure 4.o), where the values are narrowly clustered around 1.25 with the mean equal to 1.26, and the median equal to 1.25. The slight increase in value reflects regions of localised mismatches (likely due to overlapping peaks or background effects). Overall, the fit quality is statistically consistent across the majority of pixels, with no widespread or severe misfits in the dataset.

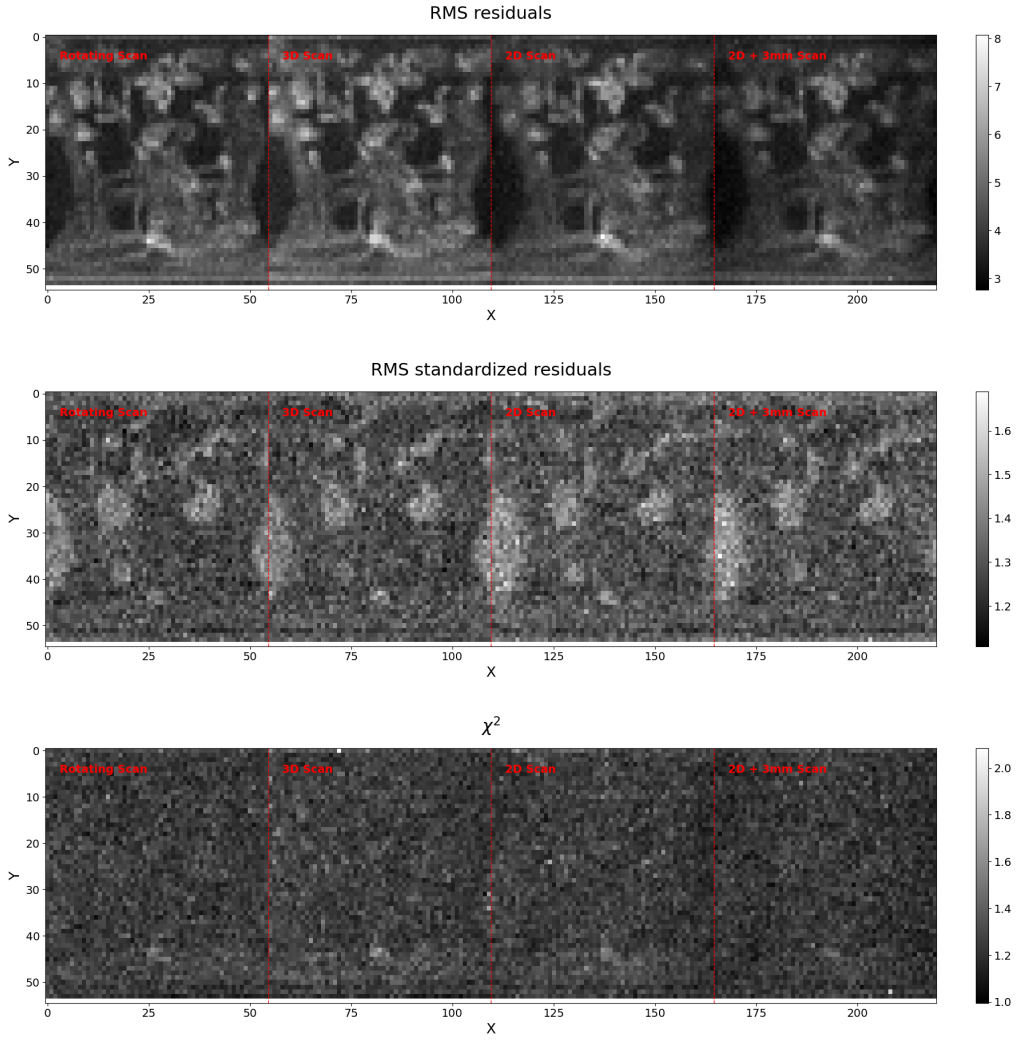

Figure 4.n: Fit quality maps across the four scan modes. Top: RMS residuals; Middle: RMS standardized residuals; Bottom: reduced . Scans are stitched together, with boundaries indicated by the red dashed lines.

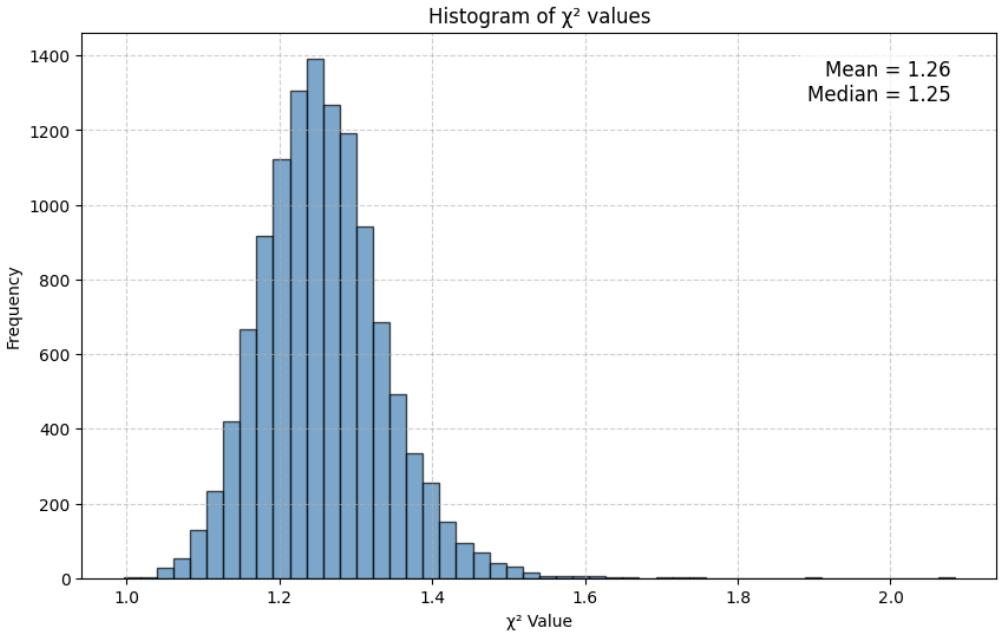

Figure 4.o: Histogram of χ^2 values of the all the pixels across all scans.

5

Results & Discussion

This section reports the results obtained from the four scanning methods (Rotating, 3D, 2D, and 2D +mm), performed on the curved mug. The section covers the spectral images obtained from the experiment, analysing the visual effects and artefacts caused by the different geometric approaches. Elemental maps and profiles are also investigated, showcasing the argon artefact signal as well as elements from the mug's decorative enamel and clay body. What follows is a discussion on the interpretation of results, implications and limitations.

5.1. Spectral Images

The final spectral images are shown in Figure 5.a, where the scan methods are presented for direct comparison with a real image of the mug. The picture design on the mug can be distinguished due to the high-count regions associated with elements in the drawing; the scene of the lady and the garden can be recognised, with her hair containing a strong signal element seen in the middle column, underneath which her dress can be seen. The bird on its hanging stick to her left is also outlined. The counts on the exposed ceramic patches are relatively lower than the coloured design, producing a contrast that helps outline some of the parts of the illustration on the mug's surface. Other aspects of the drawings, such as the leafage and the small bird, are harder to see from the sum spectral image. The result of maintaining the detection geometry throughout the curved surface is the projection of the curved decorative illustration onto a flat plane, producing an ”unwrapped appearance of the mug's design.

It can be observed that the features around the middle columns throughout the scans are identical, which is expected since the scanning methods share the exact working distances at the central column, except for the 2D+3mm scan, which is performed 3mm further away from the other scans, thus appearing less pronounced. An imaging artefact can be directly observed when comparing two-dimensional and three-dimensional scans near the edges: the right and leftmost edges of the spectral images in the two-dimensional scans appear blurrier, obscuring the shapes that remain well-defined in the three-dimensional scans. For instance,

the tree trunk to the far left with its leaves is easier to spot in the three-dimensional scans; the same applies to the blue structure to the far right. Overall, whilst the central features are comparable across all scans, the edge regions are softer and less clear in two-dimensional scans when compared to three-dimensional scans.

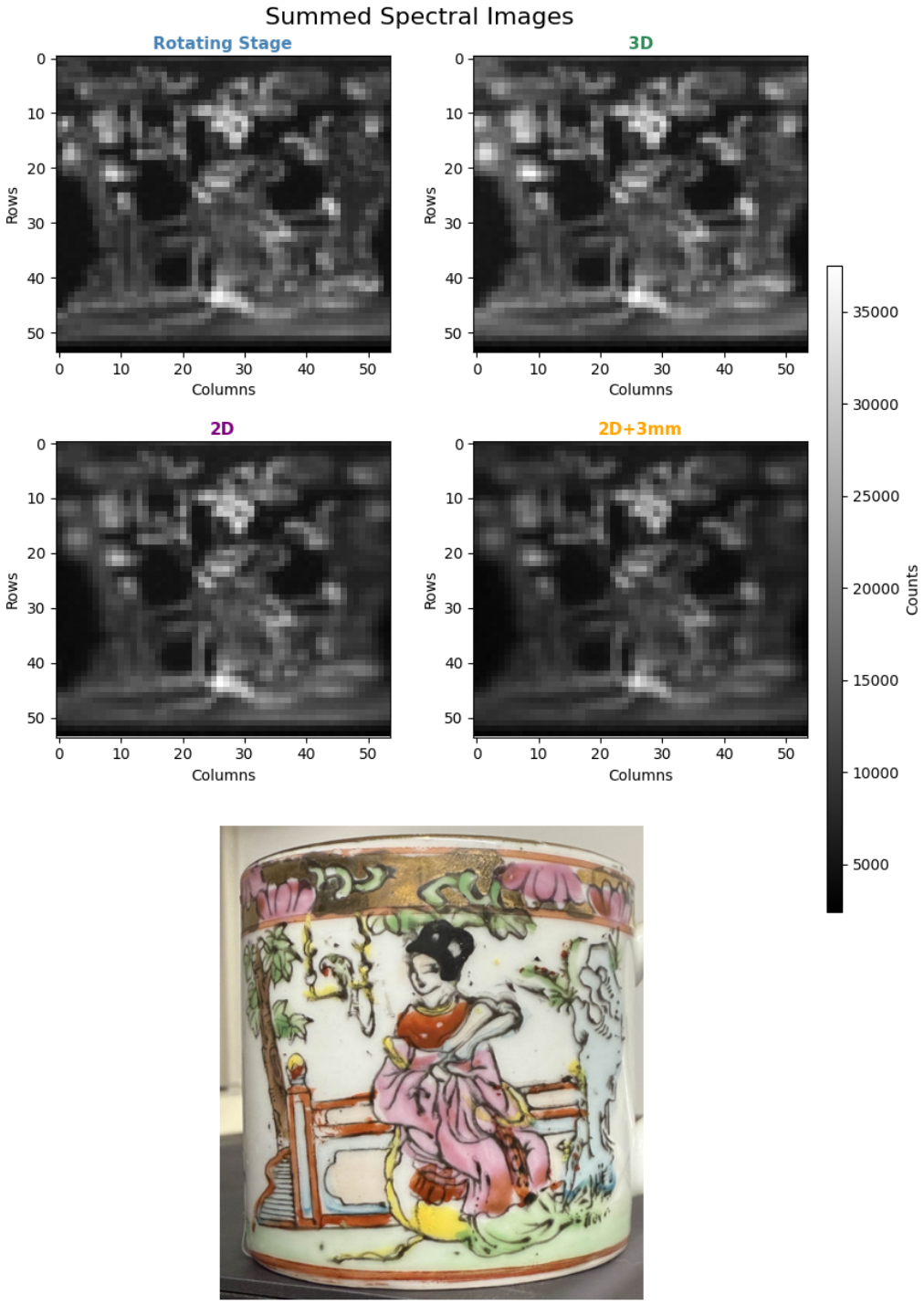

Figure 5.a: A grid of summed Spectral Images for the four scan methods. A photograph of the mug is shown for reference.

The column-summed data points shown in Figure 5.b, compare the count profiles across the columns. The profiles near the central column closely match (with an observed offset for

2D+3mm). The divergence in total count between scan methods becomes apparent for data points closer to the edge columns: Two-dimensional scan counts drop significantly compared to their central column values, while three-dimensional scans achieve higher counts for the same regions.

Another observation made from the plot is that features, such as peaks and valleys, across scan modes are not precisely aligned in lateral position; however, they do roughly match each other in shape, with the distinction appearing in relative amplitudes of the signals. This offset may be due to a human error in referencing or the positioning of the mug, as experiments were conducted on different days, and the stage setup may not have been consistent. This offset is further addressed in the next section when inspecting pixel-wise difference maps.

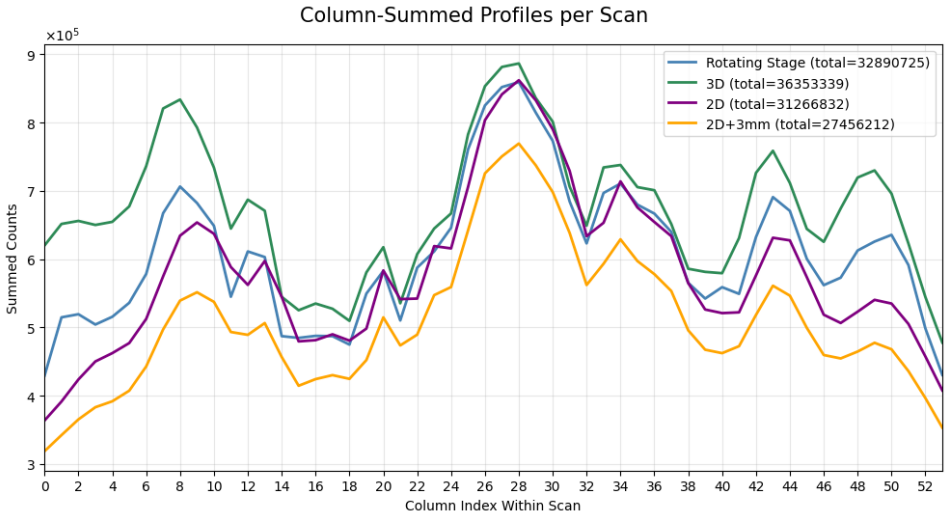

Figure 5.b: Plot of the column-summed count profiles of each scanning method.

5.1.1. Pixel-wise difference maps: 3D & 2D

To inspect each scan category (3D and 2D), pixel-wise difference maps and profiles are plotted (Figure 5.c). The left side of the figure illustrates the difference between the 3D scan and the rotating stage scan, with a plot of their difference below. It can be seen that the residuals near the central column are close to zero, and the two profiles share the same peak/valley positions. However, when inspecting regions closer to the edge, a clear difference in the imaging is evident. The 3D scan appears to distort the features in those regions, shrinking the observed shapes at the edges. This effect is correlated with a mismatch in peak positions in edge regions, suggesting that a shape distortion is taking place.

Additionally, the 3D scan produces more counts in scan areas further from the centre, especially over regions with strong features in the decorative enamel. The count divergence appears higher at the left edge than at the right edge. When plotting the difference value across columns, a constant offset is observed near the middle columns that becomes less stable as the edges are approached for columns with indices less than 15 and greater than 30. That said, the rotating stage counts dominate in a small region near column 50. Overall, the central

areas show close agreement whilst the separation increases towards the sides of the maps, with a lateral offset between peaks increasing as edge scans are approached.

The same map was produced for the two-dimensional scans, shown on the right side of the figure. In this case, there is an almost constant difference between the maps for pixel regions corresponding to the decoration. The line plot across the columns reflects this behaviour, where a stable value is observed across the mug in the lateral direction. However, it is worth noting that regions associated with the exposed ceramics exhibited a lower shift in counts when performing the 2D+3mm experiment, indicating that signal attenuation affects the elements in the mug decoration more strongly.

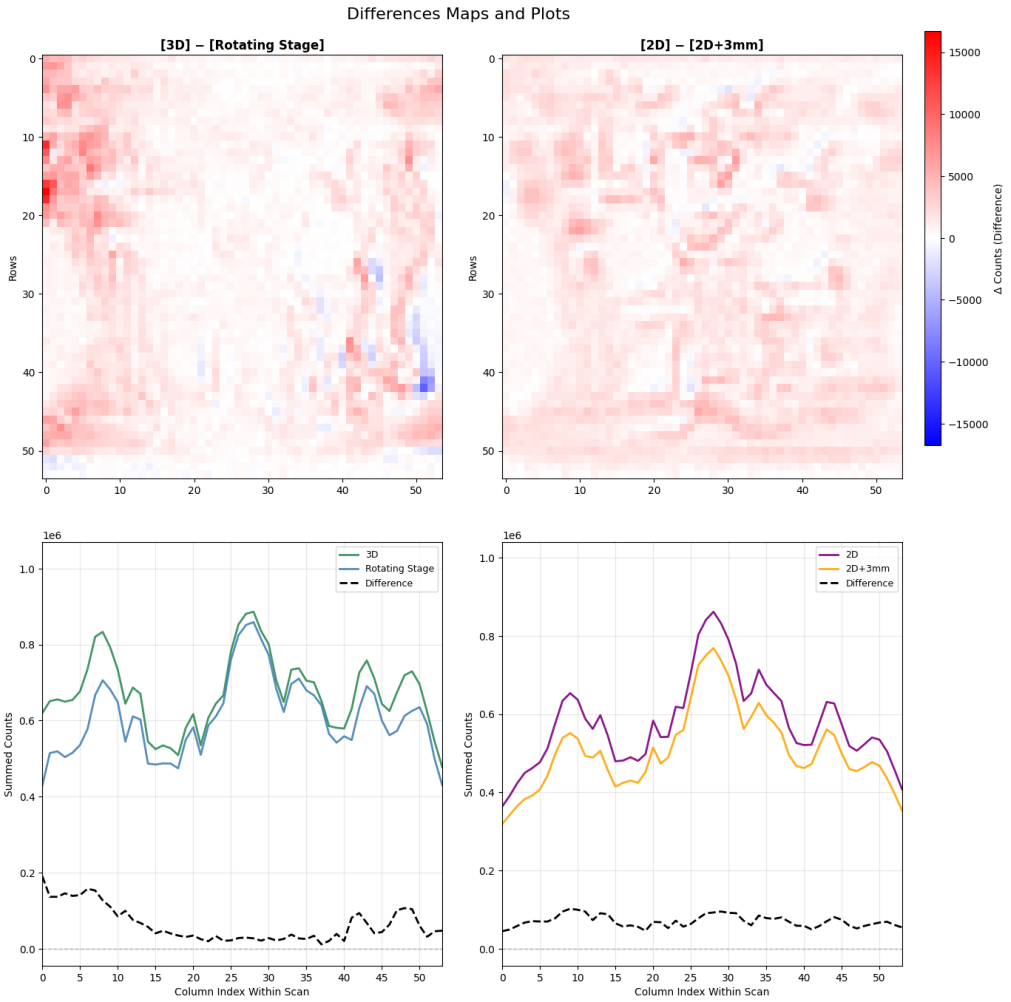

Figure 5.c: Top: Pixel-wise difference maps between 3D and 2D scans. Bottom: Column-summed count profiles plotted with the difference shown as a dashed line.

5.1.2. Pixel-wise difference maps: Rotating Scan as reference

To examine the imaging discrepancies between the rotating scan (taken as the most representative scan) and the two-dimensional scans, the pixel-wise difference maps are plotted in Figure 5.d, as well as the column-summed profiles. What was observed previously in terms of a slight displacement between the peak positions yields misalignment in the difference maps,

more evident on the [Rotating] - [2D] image, where a hysterisis (or lagging) effect obscures what is expected to be a relatively flat residual in the middle area of the scan areas.

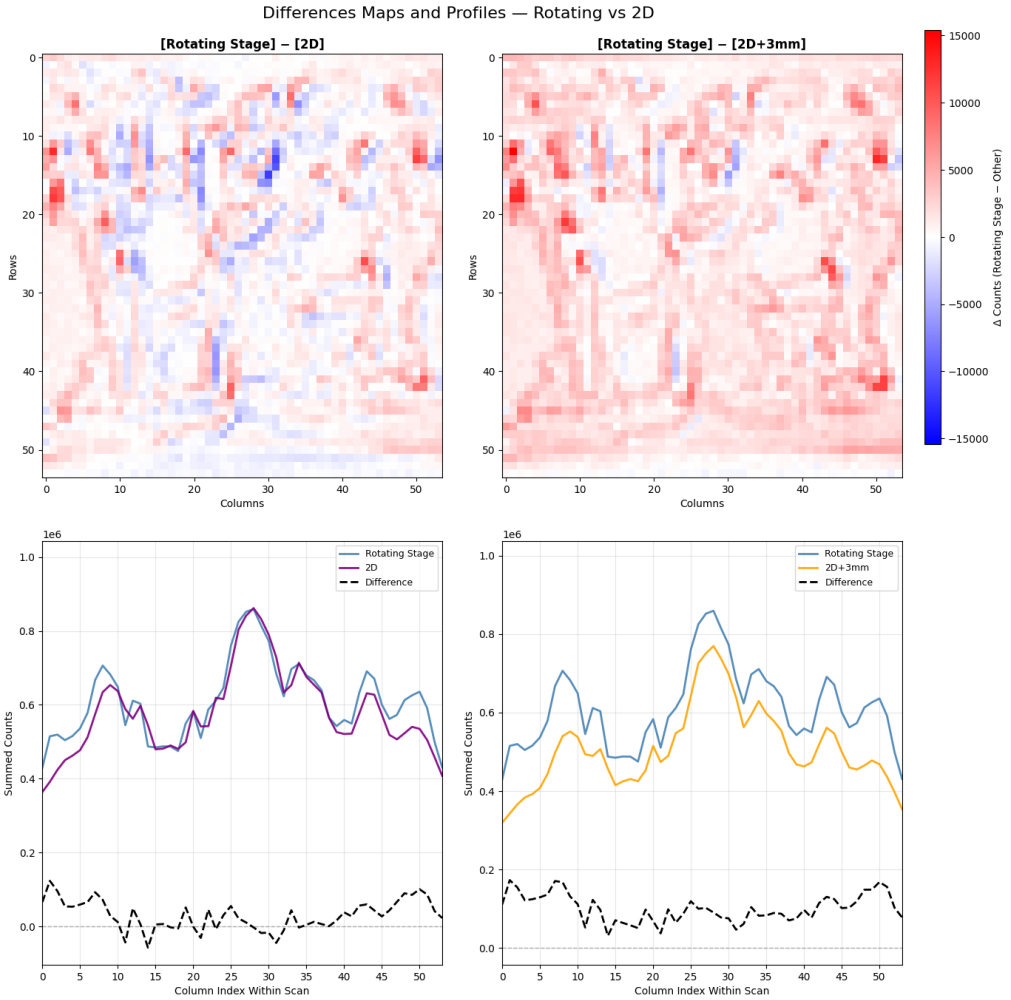

Figure 5.d: Top: Pixel-wise difference maps between the rotating stage scan and both 2D scans. Bottom: Column-summed count profiles plotted with the difference shown as a dashed line.

In an attempt to mitigate this effect, 1-D cubic interpolation was applied along the image rows, and the entire 2D maps were shifted horizontally to match the local dominant sum peak observed in the profiles. A subpixel shift of -0.4px was applied to both two-dimensional scans, resulting in a reduction of lagging effect near the centre of the mug; the difference maps after shifting exhibit reduced hysteresis around the image centre, as shown in Figure 5.e. The interpolated profiles show a more aligned sum peak in the centre, and the difference map yields relatively less noisy features. While the central features appear flatter in residuals, the edge features of the spectral images seem underrepresented during two-dimensional scans. The rotating scan appears to capture sharper images when scanning the curved surface that a traditional 2D scan would miss. That said, some pixels in the 2D scan yield slightly stronger signals than the rotating scan near edge columns, suggesting further misalignment or noise in the signals due to the airpath. This is less prevalent in the 2D+3mm scan, where the introduction of surface tilt appears to improve the surface signals from the decration, especially

on the sides of the scanned area. Overall, while helpful in improving the spectral look of the data, interpolation of the data should be treated with caution, since it reweights intensities and oversmoothes the spectral features, introducing artefacts in the data.

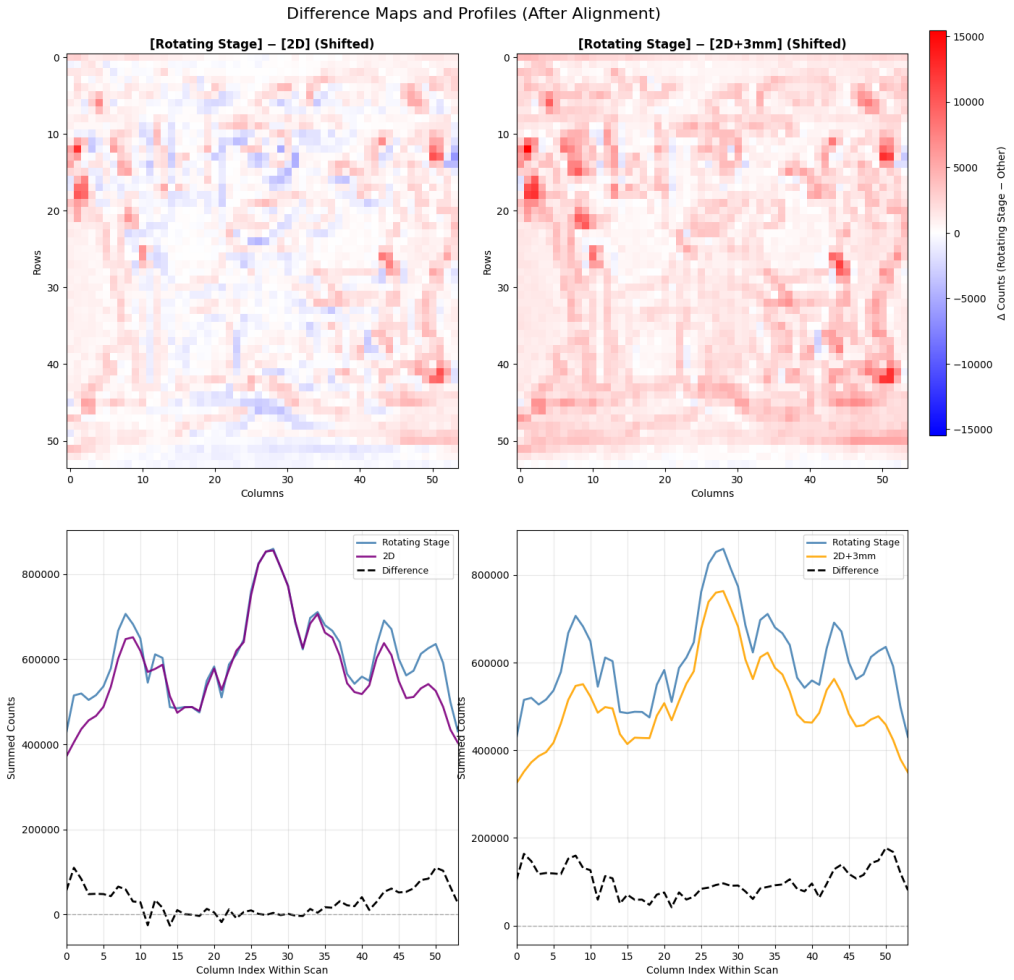

Figure 5.e: Top: Pixel-wise difference maps between the rotating stage scan and both 2D scans (after sub-pixel alignment). Bottom: Column-summed count profiles plotted with the difference shown as a dashed line.

5.2. Elemental Maps

To visualise the effect of geometry on the elemental signals in the sample, elemental maps were produced, visualising their distribution across the scan area. Although 30 spectral channels were fitted for the 25 elements detected in the sample, only a few prevalent ones are shown in this section, which showcases the effect of the proposed scanning methods on material signals associated with the airpath, enamel decoration, and the ceramic body of the mug.

5.2.1. Air absorption: Argon Signal

The argon elemental maps and profiles (shown in Figure 5.f showcase the geometric nature of the respective XRF scans. Three-dimensional scans produce a flatter and almost feature-

less map, yielding more uniform argon signals. The argon line reflects this fact, showcasing relatively stable counts per pixel of 292.1056 ± 0.7151 (σ=38.6150) for the Rotating Scan, and 315.9460 ± 0.7539 (σ=40.7112) for the 3D scan. The two-dimensional scans, on the other hand, showcase a gradient, with a trough corresponding to the middle of the scan, where the acquisition is closest to the mug; this trough minimum for the 2D scan matches closely to the three-dimensional scans (while 2D+3mm shows increased counts). The parabolic curves of two-dimensional scans are roughly symmetric for the 2D+3mm scan, whilst the 2D scan appears skewed, with the left edge value appearing higher than the right edge.

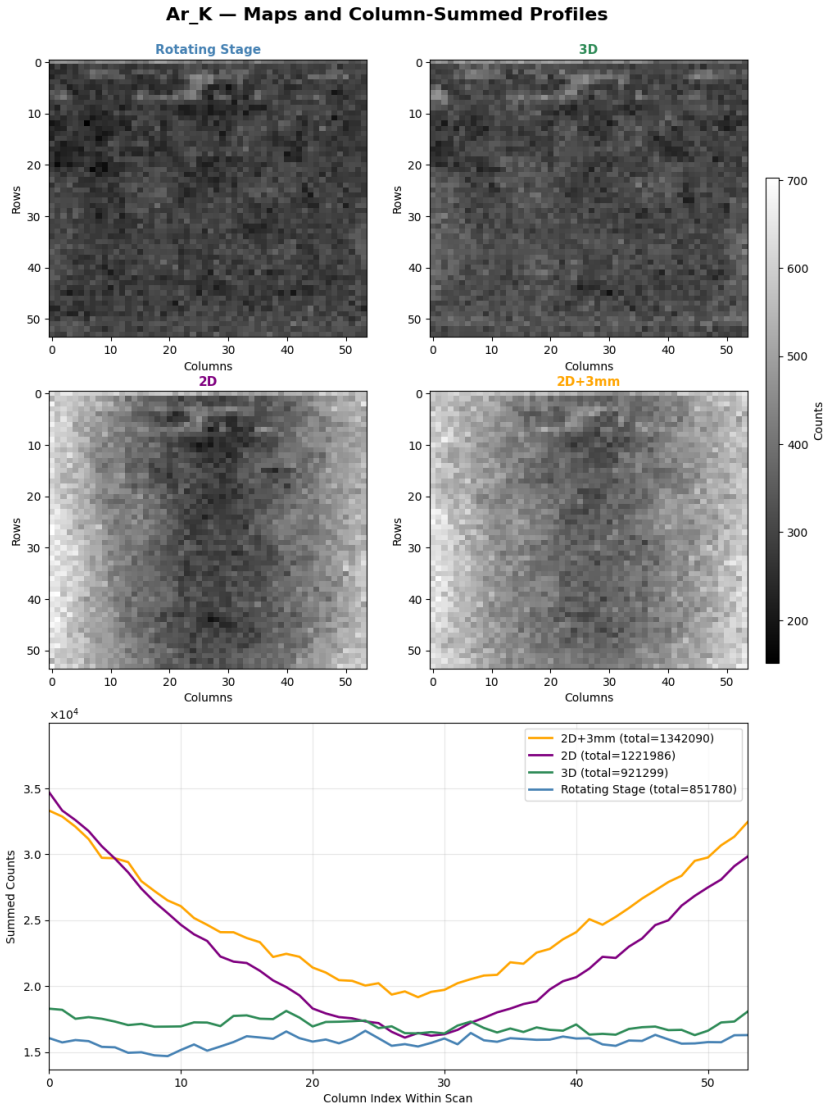

Figure 5.f: Top: Elemental Distribution map of Argon (Ar-K) in the scanned area for each scanning method. Bottom: The column-summed signal profile of argon for each scanning method.

Although the Ar-K signals are consistent (weather gradient or flat), the argon distribution map shows a notable feature, particularly near the top strip of the image. The top band patterns appear across the whole width for the three-dimensional scans, while fading away near the edges for the two-dimensional scans. This feature appears in the same regions and is of similar

shape to the gold signal Au-M along the top strip, as seen in Figure 5.g. This artefact could be due to a scattering impact when striking the golden rim, leading to an enhanced count in the argon signal in those areas.

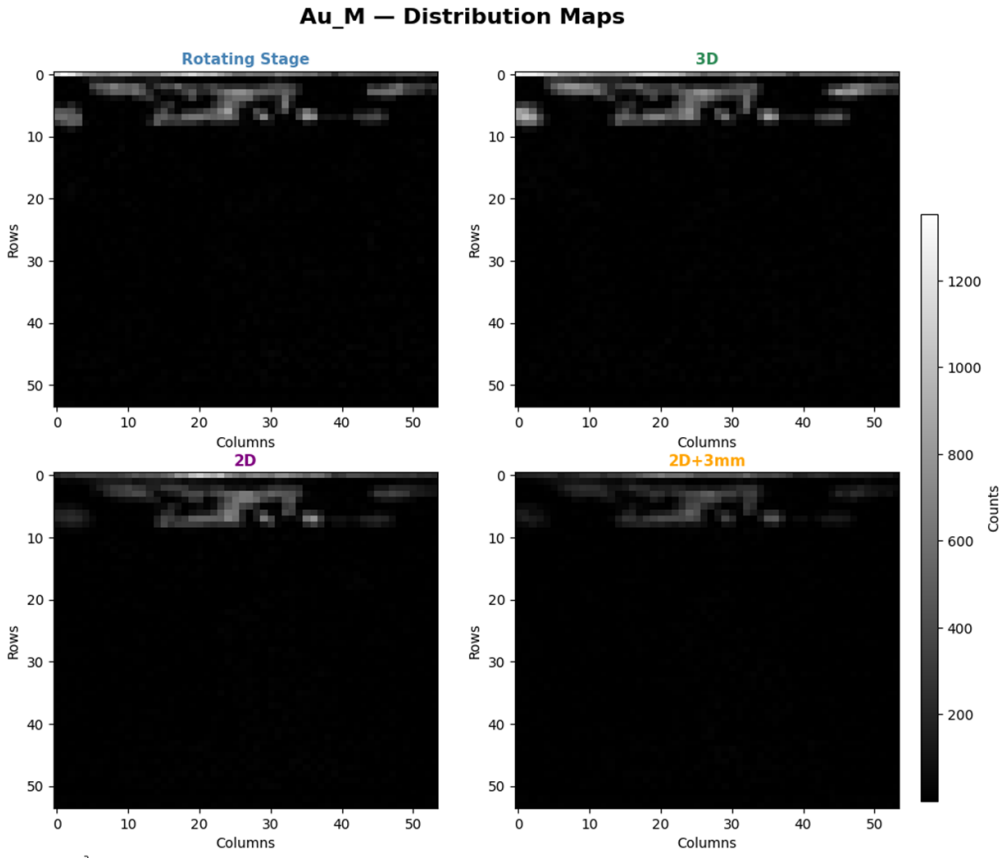

Figure 5.g: Elemental Distribution map of Gold (Au-M) in the scanned area for each scanning method

5.2.2. Decorative Enamel

Some elements in the decorative enamel material are investigated to inspect the geometric distortion observed in the spectral images. Figure 5.h plots the distribution maps of lead (Pb-L3), zinc (Zn-K), and chromium (Cr-K), which seem to be present in the paint on the mug's surface when visually comparing the reference image with the elements above. The lead signals are strong and are emitted from all the painted parts, covering the decoration across the mug except for the exposed gold strip at the top of the mug. Zinc signals can be observed for areas corresponding to the greens and blues, such as the grass and foliage, as well as the blue in the bench and the structure on the far right. Chromium is mainly concentrated in the hair of the lady in the figure; however, traces of it are detected in most of the painted areas.

Although the distributions of these elements are consistent across scan methods, the contrast between the centre of the scan and further edges is not comparable between the three-dimensional scans and the two-dimensional scans. For instance, the lead signals in the 2D and 2D+3mm scans exhibit a blurring effect, which weakens the signal as the sides are approached. The addition of the third dimension enhances the clarity of the zinc elements, partic-

ularly showcasing a sharper outline of the structure on the right and the leaves on the far left. Chromium signals also show the gradual blur effect on the sides, whilst showing comparable signals in the central columns of the scans. It can also be observed across all elements that whilst the 3D scan produces sharper features on the sides of the scan area, it appears both stronger and slightly distorted in shape when compared to the rotating scan. Additionally, the fixed offset in the 2D+3mm scan from the 2D scan seems to produce weaker signals. Overall, the elemental signals correspond to the visual effect observed in the sum spectra image, suggesting that the impact of geometry is prevalent for elements in the enamel.

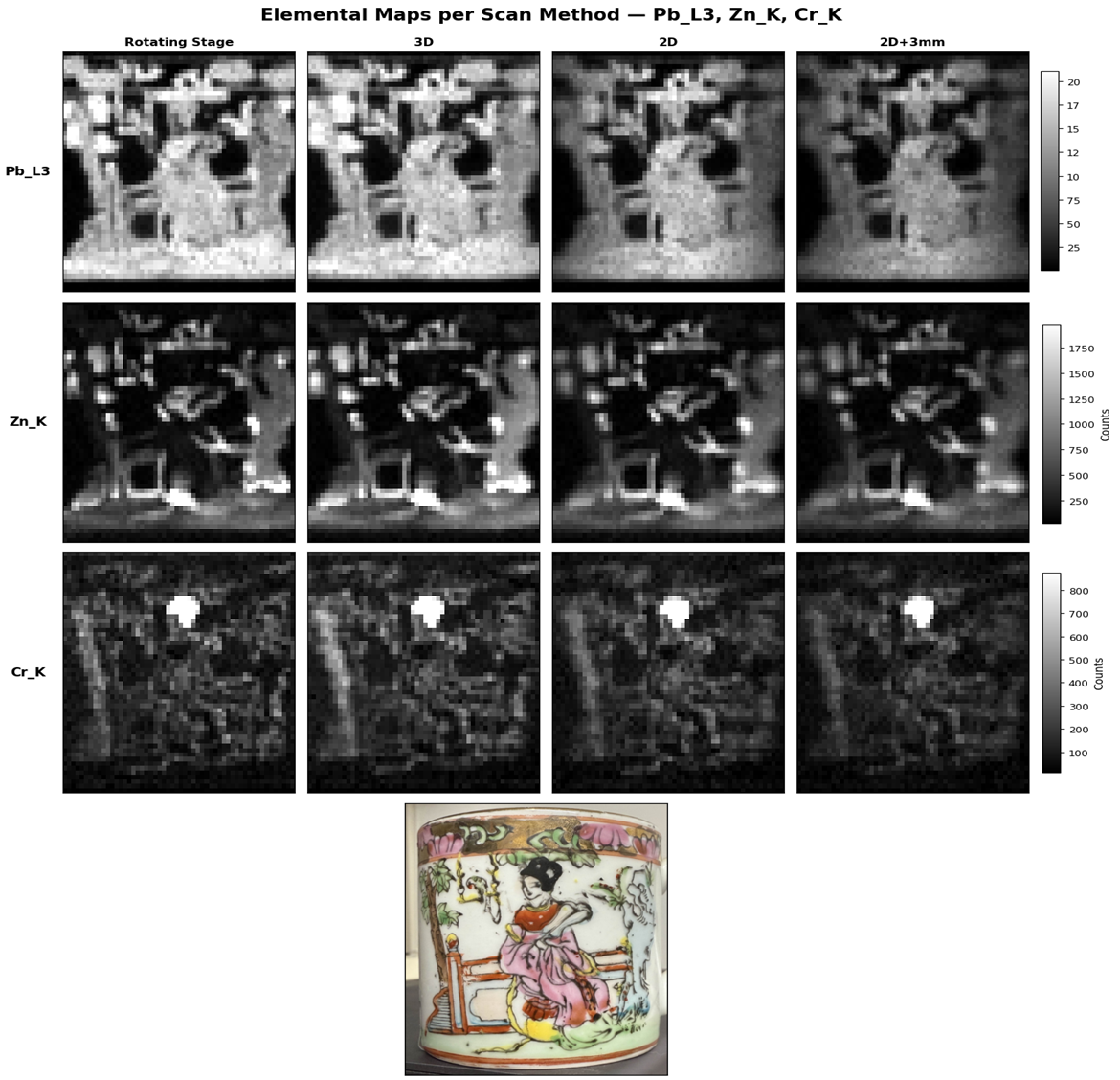

Figure 5.h: Elemental Distribution map of Lead (Pb-L3), Zinc (Zn-K), and Chromium (Cr-K) in the scanned area for each scanning method. A photograph of the mug is shown for reference.

5.2.3. Ceramic Body

Potassium present in the clay ceramic matrix and/or glaze is mapped in Figures 5.i. While the distribution maps suggest that these elements might be partly present in some of the decora-

tive layers of the mug, they appear to be attenuated in these maps, showing contrast between the mug surface and the painted figure on the surface. As with the case of the decorative layer and spectral images, a gradual blur appears in the two-dimensional scans, increasing toward the sides of the scanned area. In the case of the 2D+3mm scan, the added offset results in further fading of the exposed ceramic on the far right, blending the structure with the exposed ceramic on the surface.

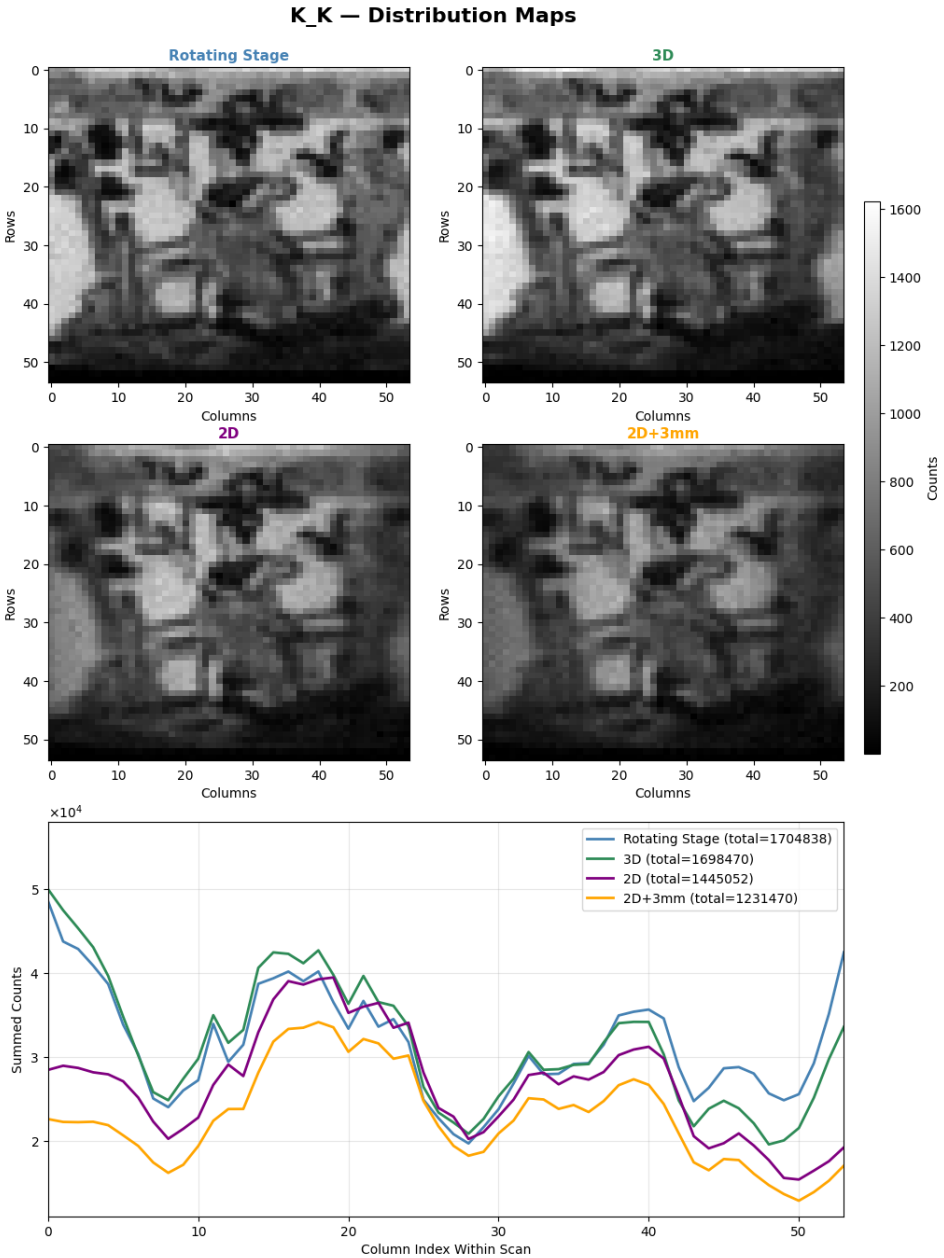

Figure 5.i: Top: Elemental Distribution map of Potassium (K-K) in the scanned area for each scanning method.

5.2.4. Elemental Profiles

The column-summed profiles for Pb, Zn, Cr, and K (Figure 5.j) show broadly aligned features in position, with the slight lateral offset seen previously in the total sum plots. The stacking order tends to be consistent across much of the scan, where the 3D and rotating profiles are typically higher and match closely, whilst the 2D is lower, and 2D+3mm is the lowest. There is general agreement across modes around the middle column. The behaviour at the edge is distinguished, where the rotating stage and 3D scan appear to maintain signal strength whilst 2D and 2D+3mm scans are weakened. That said, the three-dimensional scans exhibit slight differences in edge behaviour between elements, with the 3D scan marginally higher at the sides for Pb/Cr/Zn, and rotating seemingly higher for K.

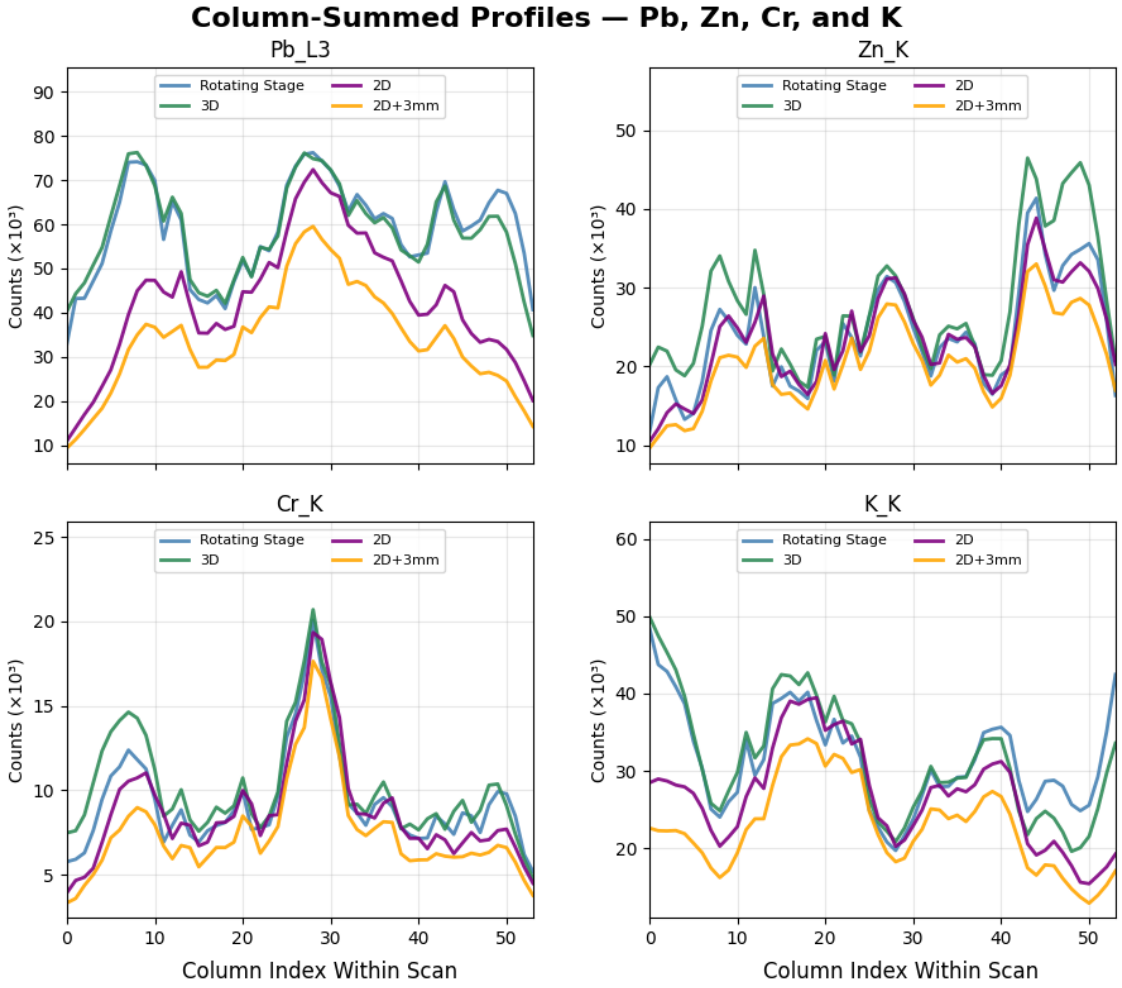

Figure 5.j: The column-summed signal profile of Pb, Zn, Cr, and K for each scanning method.

5.3. Discussion

5.3.1. Summary of Findings

The results from the four scanning methods demonstrate the impact of scanning strategies on XRF acquisition. It is observed that when the scan strategies approximate around the central columns, the image clarity and the count profiles are comparable, matching closely in clarity and in profile features. The main differences emerge towards the lateral edges of the scan area, where the signal from the flat-plane scans (2D and 2D+3 mm) appears weaker, resulting in blurred edges in the spectral images. Non-flat scans (Rotating and 3D), on the other hand, show no blurring maintain focus and clarity. The difference between the three-dimensional scans becomes apparent only when inspecting the pixel-wise difference map, which reveals that the 3D scan produces slightly higher counts of edge features. This geometric effect is reflected in the count profiles across the lateral direction, showcasing a strong distinction between the scan approaches at edge counts. The same qualitative observations carry over in the elemental distribution images of elements in the enamelled decoration and the ceramic matrix, with minor element-dependent signal variations at the edge between the three-dimensional scans.

5.3.2. Lateral Resolution

It is evident from the results that the curved surface of the mug has a direct impact on the scanning geometry of the scans, governing the resolution and clarity of the obtained spectra. The variation in apparent intensity and edge sharpness between scans (seen in Figures 5.k) indicates an effect related to the scanning geometry. Scanning methods which maintain the working distance between the scanner and the curved sample surface produce a more consistent and focused image across the scan area, whilst flat-plane scans produce inconsistent images, where the clarity is directly affected by the change in scan geometry due to the object's curved surface. The dissimilarity in the acquired counts correlates with the discrepancy in real detection geometry across the scan area, where the counts at the edges of the scan areas for flat scans reduce significantly compared to the non-flat scans.

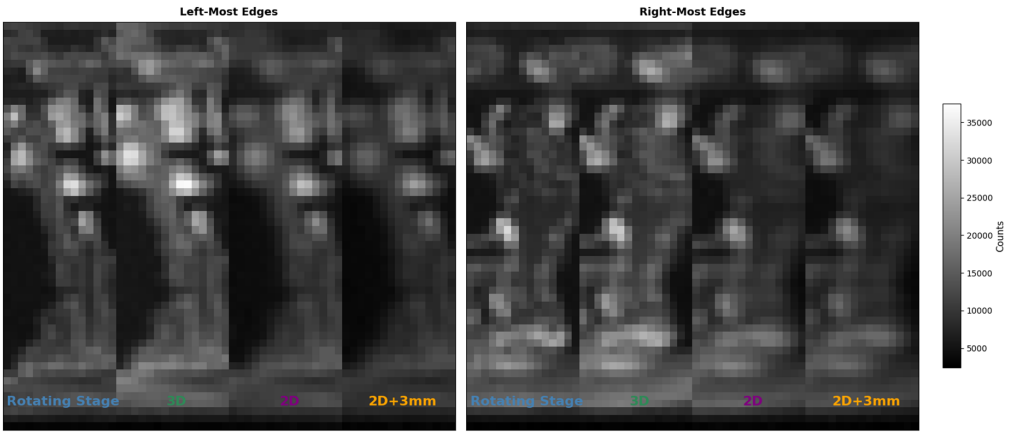

Figure 5.k: Left and Right edge regions stitched together from the different scan methods, showcasing a blurring artefact in the data.

5.3.3. Working Distance

The cylindrical geometry of the sample results in a progressive increase in signal attenuation and airpath when scanning further from the central columns closest to the scan head. The same impact is observed in elemental scans, where edge features are blurred in flat-plane scans. Scanned areas where the working distances match at the central columns appear comparable between all scan modes, suggesting that the working distance is an unassuming driver of the apparent intensity and feature sharpness of the curved surface. The effect of offsetting the two-dimensional scan in the 2D+3mm scan results in a non-uniform reduction in the count rate, further evident in the difference map between the flat scans; instead of a constant residual across the map, the difference map produces the pattern of the mug, showcasing the areas with decorative enamel. This suggests that working distance does not influence the present elements evenly.

Analysis of the total counts across the scanned columns reflects the effects of working distance on the acquisitions. All scanning modes exhibit features (such as peaks and valleys) in their column sum profiles, albeit with slightly different relative amplitudes depending on their position in the scanned area (therefore, the effective working distance). It is difficult to comment on the absolute differences in counts across the columns or rows between scans, as the instrument is not well-calibrated and has been shown to fluctuate in count rate due to detector temperature drift (as observed in section 4.3, Figure 4.j). However, the results show that the rate follows the order: 3D > Rotating Stage > 2D > 2D + 3 mm. When comparing local sum spectra (Figure 5.l), the energy gaps between each scan at the elemental peaks reflect the hierarchy in count rate. However, it can also be seen that the Argon peaks do not follow this order, where the flat scans produce higher argon counts; the contribution from the Rhodium tube appears equivalent throughout the scans. Altogether, an increase in working distance seems to reduce the total counts, which is observed in the visual map, the column-summed plots and the local summed spectra.

5.3.4. Surface Tilt

Surface tilt is the only physical distinction between the three-dimensional scan modes. It is expected that the increase in detection volume in the 3D scan, as the apparent mug sidewall thickness increases on the sides, would produce higher counts and slightly distort the spectral image. This effect, however, is harder to observe from the summed spectra and elemental maps. The distinction can only be qualitatively observed on the pixel-wise difference map between the rotating and 3D scan, highlighting a fundamental difference in the count of edge features, where the 3D scan appears to exceed in total counts. Although the total spectra suggest that the 3D scan produces higher counts for edge features, this is not always reflected in the elemental maps, particularly in those of elements found in the ceramic matrix. The interpretations regarding tilt, therefore, are treated with uncertainty, given the observed residual misalignment, limited calibration, and detector drift.

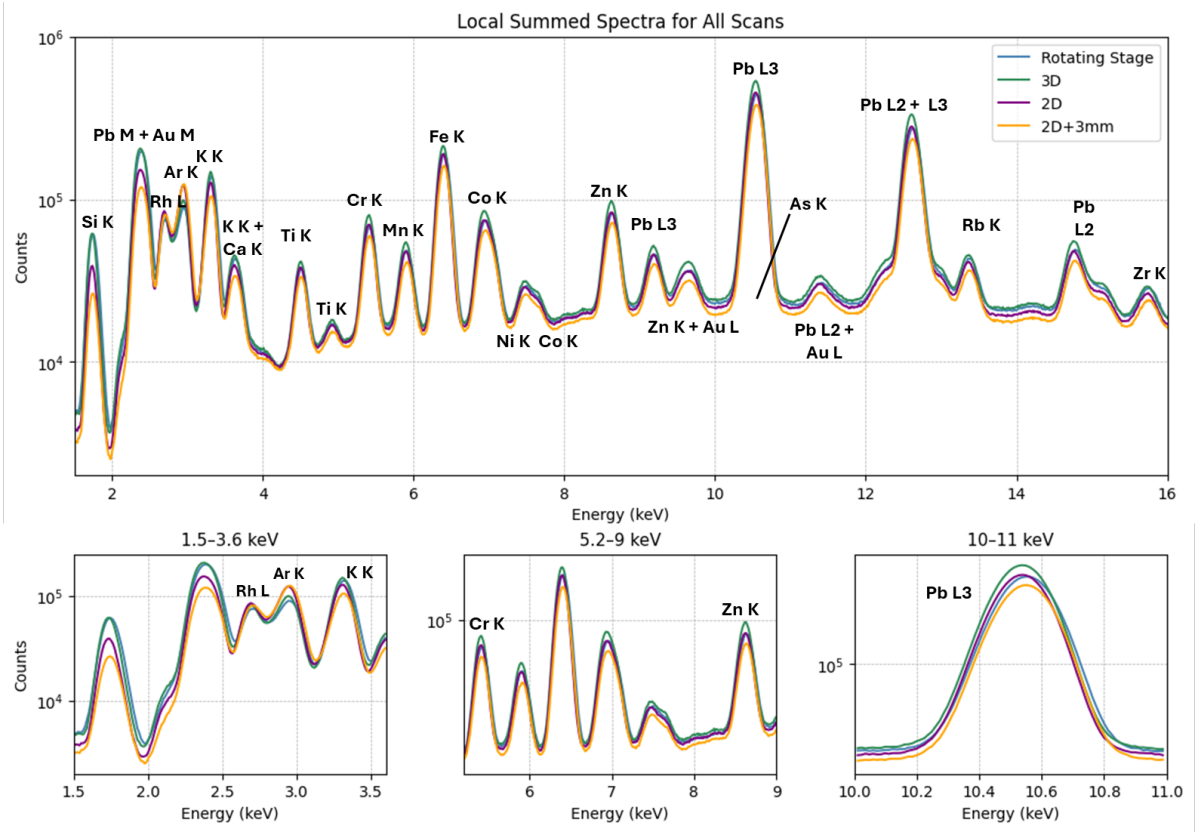

Figure 5.I: Local summed XRF spectra for all scans. The top panel shows the full 1.5–16 keV range with major elemental peaks labeled, while the bottom panels highlight selected regions.

5.3.5. Limitations

Although some conclusive statements can be drawn from the data, limitations exist that inhibit further interpretation. Upon inspection of the instrument response, the Argon signal shape reasonably reflects the geometric nature of the approaches. However, there is a notable residual in the distribution map which appears across scan mods in the top strip. This indicates the misfit or noisy regions of the data that were not resolved during batch fitting.

Another shortcoming of these experiments is the lack of characterisation and calibration of the instrument, which questions the reliability of the scans and prohibits numerical analysis. Furthermore, the effect of detector temperature drift has influenced the detector response, producing inconsistent count rates between scan experiments. This is evident, for example, in the inconsistent patterns between the three-dimensional scans' elemental profiles, suggesting that the detector response artefact may bias the results.

The noted misalignment of central features between scans adds a layer of uncertainty to the data set. The source of misalignment can be due to inconsistent referencing of scan setup between the experiments, for example, due to human error in mispositioning the mug. This is further suggested by the skewness observed for the 2D scan in the argon signal. That said, this was easily addressed using 1-D cubic interpolation of the data in the lateral direction, which mitigated the effects of misalignment. That said, reweighting of intensities using interpolation, if not done carefully, can result in oversmoothing in the data and may introduce artificial fea-

tures in the results. Although not precise, interpolation-based aligned difference maps have improved the qualitative inspection of the pixel-wise differences.

Overall, these results must be taken with a level of uncertainty due to limitations emerging from the lack of instrument characterisation, poor referencing, detector response drift, and slight fitting residuals. Despite all these limitations, the geometric effect is directly visible in the spectral and elemental distribution and corroborated by trends in the column-summed profiles. Within these limits, the qualitative observations made in this project remain valid.

6

Conclusions & Recommendations

Conclusions

The field of cultural heritage relies on macro X-ray fluorescence imaging (MA-XRF) for the study of objects of various shapes. This thesis examines the effect of geometry when scanning the surface of a curved object with MA-XRF. Curved surfaces can complicate XRF acquisition when done in two dimensions due to variation in working distance and surface tilt across the scanned area, which alters the acquired signals and spatial fidelity. To address this problem, the project aims to demonstrate the effects of varying scan geometries on the MA-XRF acquisitions while also showcasing scanning strategies which improve acquisitions by adhering to the curved surface of three-dimensional objects.

A methodology was developed to scan a cylindrical test object in 2D, 3D, and 3D again while adhering to surface tilt. These methods were tested using a straightforward benchtop MA-XRF instrument that was built for this project. The instrument consists of three motorised linear stages, a scanhead, and a rotating stage to rotate the tested sample. Software was developed to control motor positioning, acquisition, and process data into H5 files. A decorative glazed ceramic mug from a secondhand store, featuring enamelled decorations, was scanned in the different geometric modes. The scans were conducted on the same 55x54 mm^2 area on the face of the mug, twice in flat scans at different offsets, and then twice using three-dimensional approaches (with and without the rotating stage). The data were batch fitted using PyMCA, and elemental and spectral distribution maps were produced.

The resulting spectral images show agreement near the central scanned area, where the working distance and tilt are matched, and then diverge towards the sides of the scanned area, correlating with the curvature of the mug. The flat plane scans reflect the effect of varying working distance as the sides of the mug are scanned, showcasing a progressive softening in the apparent image at the edges as the signals attenuate. The three-dimensional scans, on the other hand, retain clearer details across the image, showcasing relatively stronger signals at the edges. This trend carries over across multiple elements, both in the enamel and the

ceramic body. Column summed profiles of the total and elemental counts reflect these patterns, showing higher edge counts for the geometrically-aware scanning experiments. Pixel-wise difference maps further showcase these effects, revealing substantial divergence in the data at the edges.

The dataset's limitations introduce uncertainties regarding the extent of these geometric effects in the spectral and elemental data. Notable shortcomings of the experiments include slight misfitting shown in the argon signal and a varying detector response influenced by a change in temperature throughout the scan. Furthermore, subpixel misalignment between the two-dimensional and three-dimensional scans limits pixel comparisons unless the data is interpolated.

Despite these limitations, the qualitative analysis of the results remains valid and provides valuable insight into the effect of geometry in MA-XRF imaging. Altogether, the results support the conclusion that adhering to the curved surface of objects when conducting MA-XRF acquisitions extensively improves image and signal accuracy. The approach of maintaining working distance and/or surface tilt preserves spectral fidelity and yields accurate representations of a curved sample surface. The solution presented in this thesis offers a valid and straightforward approach to capturing accurate representations of the surface of a cylindrical object.

Recommendations

For future work, improving the current instrument is recommended by characterising its response and detection geometry with a known reference sample. This will further validate acquisitions which investigate geometric effects, allowing for more reliable qualitative (and even quantitative) analysis, and avoiding the use of post-hoc data interpolation. Further improvements can be made by developing adaptive scan paths to follow more complex three-dimensional shapes. This could be done using well-referenced laser or imaging positioning. Alternatively, 3D imaging using photogrammetry or other capturing techniques could be adopted to generate scan paths of any three-dimensional objects.

Bibliography

[1] Kelsey E. Young, Cynthia A. Evans, Kip V. Hodges, Jacob E. Bleacher, and Trevor G. Graff. A review of the handheld X-ray fluorescence spectrometer as a tool for field geologic investigations on Earth and in planetary surface exploration. *Applied Geochemistry*, 72:77–87, 9 2016.

[2] H. Z. Shan, S. J. Zhuo, R. X. Shen, and C. Sheng. Mineralogical effect correction in wavelength dispersive X-ray florescence analysis of pressed powder pellets. *Spectrochimica Acta Part B: Atomic Spectroscopy*, 63(5):612–616, 5 2008.

[3] Roozbeh Ravansari, Susan C. Wilson, and Matthew Tighe. Portable X-ray fluorescence for environmental assessment of soils: Not just a point and shoot method. *Environment International*, 134:105250, 1 2020.

[4] Hervé Rebiere, Audrey Kermaïdic, Céline Ghyselinck, and Charlotte Brenier. Inorganic analysis of falsified medical products using X-ray fluorescence spectroscopy and chemometrics. *Talanta*, 195:490–496, 4 2019.

[5] Riccardo Fedeli, Luigi Antonello Di Lella, and Stefano Loppi. Suitability of XRF for Routine Analysis of Multi-Elemental Composition: A Multi-Standard Verification. *Methods and Protocols*, 7(4):53, 8 2024.

[6] A. van Loon, P. Noble, D. de Man, M. Alfeld, T. Callewaert, G. Van der Snickt, K. Janssens, and J. Dik. The role of smalt in complex pigment mixtures in Rembrandt's Homer 1663: combining MA-XRF imaging, microanalysis, paint reconstructions and OCT. *Heritage Science*, 8(1):1–19, 12 2020.

[7] Anna Mazzinghi, Chiara Ruberto, Lisa Castelli, Paola Ricciardi, Caroline Czelusniak, Lorenzo Giuntini, Pier Andrea Mandò, Marco Manetti, Lara Palla, and Francesco Taccetti. The importance of being little: MA-XRF on manuscripts on a Venetian island. *X-Ray Spectrometry*, 50(4):272–278, 8 2021.

[8] Philippe Colomban, Mareike Gerken, Michele Gironda, and Viviane Mesqui. On-site micro-XRF mapping of enameled porcelain paintings and sculpture. First demonstration. *Journal of the European Ceramic Society*, 45(1):116849, 1 2025.

[9] Anikó. Bezur, Lynn. Lee, Maggi. Loubser, and Karen. Trentelman. *Handheld XRF in cultural heritage : a practical workbook for conservators*. The Getty Conservation Institute, 2020.

[10] B. Beckhoff, B. Kanngießer, N. Langhoff, R.Wedell, and H.Wolff. *Handbook of Practical X-ray Fluorescence Analysis*. Springer, Berlin-Heidelberg, 1st edition, 2006.

[11] Peter. Brouwer. *Theory of XEF : getting acquainted with the principles*. PANalytical BV, 2003.

[12] Richard M. Rousseau. Corrections for matrix effects in X-ray fluorescence analysis—A tutorial. *Spectrochimica Acta Part B: Atomic Spectroscopy*, 61(7):759–777, 7 2006.

[13] Ladislav Musílek, Radek Prokeš, and Tomáš Trojek. Overview of methods for determining the depth distribution of elements in X-ray fluorescence analysis. *Radiation Physics and Chemistry*, 200:110388, 11 2022.

[14] Tomáš Trojek, Tomáš Čechák, and Ladislav Musílek. Recognition of pigment layers in illuminated manuscripts by means of Kα/Kβ and Lα/Lβ ratios of characteristic X-rays. *Applied Radiation and Isotopes*, 68(4-5):871–874, 4 2010.

[15] Kazuhiko Nakano, Atsushi Tabe, Susumu Shimoyama, and Kouichi Tsuji. Visualizing a black cat drawing hidden inside the painting by confocal micro-XRF analysis. *Microchemical Journal*, 126:496–500, 5 2016.

[16] T. Trojek and M. Hložek. Confocal XRF imaging for determination of arsenic distribution in a sample of historic plaster. *Radiation Physics and Chemistry*, 200:110201, 11 2022.

[17] R. Šefců, Chlumská, A. Třeštíková, T. Trojek, and L. Dragounová. Investigation of the panel painting of St Anne with the Virgin Mary and the Child Jesus using analytical and imaging methods. *Applied Radiation and Isotopes*, 95:8–12, 1 2015.

[18] Demet Yılmaz and Elif Boydaş. The use of scattering peaks for matrix effect correction in WDXRF analysis. *Radiation Physics and Chemistry*, 153:17–20, 12 2018.

[19] Andrzej. Markowicz, D.. Wegrzynek, and K.. Will. *In situ applications of X ray fluorescence techniques : final report of a coordinated research project, 2000-2003*. IAEA, International Atomic Energy Agency, 2005.

[20] W. Weyrich. B. K. Agarwal: X-Ray Spectroscopy, An Introduction. Springer-Verlag, Berlin, Heidelberg, New York 1979. 418 Seiten, Preis: DM 74,—. *Berichte der Bunsengesellschaft für physikalische Chemie*, 87(4):371–372, 4 1983.

[21] V. Arkadiev, H. Bräuninger, W. Burkert, A. Bzhaumikhov, H. E. Gorny, N. Langhoff, A. Oppitz, and J. Rabe. Monochromatic X-ray source for calibrating X-ray telescopes. *Nuclear Instruments and Methods in Physics Research, Section A: Accelerators, Spectrometers, Detectors and Associated Equipment*, 455(3):589–595, 12 2000.

[22] Microfocus technology | Innovative Microfocus X-ray Tubes from X-RAY WorX.

[23] R. Birch. The spectrum and intensity of extra-focal (off-focus) radiation. *British Journal of Radiology*, 49(587):951–955, 11 1976.

[24] Matthieu N. Boone, Jelle Vlassenbroeck, Steven Peetermans, Denis Van Loo, Manuel Dierick, and Luc Van Hoorebeke. Secondary radiation in transmission-type X-ray tubes: Simulation, practical issues and solution in the context of X-ray microtomography. *Nuclear Instruments and Methods in Physics Research Section A: Accelerators, Spectrometers, Detectors and Associated Equipment*, 661(1):7–12, 1 2012.

[25] Elisa Toto, Lucia Lambertini, Susanna Laurenzi, and Maria Gabriella Santonicola. Recent Advances and Challenges in Polymer-Based Materials for Space Radiation Shielding. *Polymers 2024, Vol. 16, Page 382*, 16(3):382, 1 2024.

[26] Irina Stenina, Tatiana Kulova, and Andrey Yaroslavtsev. Evolution of Mn-doped LiFePO4 during cycling: Fast synchrotron operando Mössbauer studies. *Materials Today Chemistry*, 39:102160, 7 2024.

[27] Arwen R. Pearson and Pedram Mehrabi. Serial synchrotron crystallography for time-resolved structural biology. *Current Opinion in Structural Biology*, 65:168–174, 12 2020.

[28] Fengcheng Li, Runze Liu, Wenjun Li, Mingyuan Xie, and Song Qin. Synchrotron Radiation: A Key Tool for Drug Discovery. *Bioorganic & Medicinal Chemistry Letters*, 114:129990, 12 2024.

[29] Gianluca Geloni, Vitali Kocharyan, and Evgeni Saldin. Brightness of synchrotron radiation from wigglers. *Nuclear Instruments and Methods in Physics Research Section A: Accelerators, Spectrometers, Detectors and Associated Equipment*, 807:13–29, 1 2016.

[30] Marie Jacquet. Potential of compact Compton sources in the medical field. *Physica Medica*, 32(12):1790–1794, 12 2016.

[31] M.J. Berger and J.H. Hubbell. XCOM: Photon cross sections on a personal computer. *U.S Department of Commerce*, (NBSIR 87-3597), 7 1987.

[32] T.M. Tritt. Thermoelectric Materials: Principles, Structure, Properties, and Applications. *Encyclopedia of Materials: Science and Technology*, pages 1–11, 1 2002.

[33] Kouichi Tsuji and Filip Delalieux. Feasibility study of three-dimensional XRF spectrometry using μ-X-ray beams under grazing-exit conditions. *Spectrochimica Acta Part B: Atomic Spectroscopy*, 58(12):2233–2238, 12 2003.

[34] D. Hampai, V. Guglielmotti, A. Marcelli, G. Cappuccio, and S. B. Dabagov. Shaped X-ray beams by channeling in polycapillary optics. *Radiation Physics and Chemistry*, 174:108965, 9 2020.

[35] J. B. Ullrich, V. Kovantsev, and C. A. MacDonald. Measurements of polycapillary x-ray optics. *Journal of Applied Physics*, 74(10):5933–5939, 1993.

[36] Carolyn A. MacDonald. Focusing Polycapillary Optics and Their Applications. *X-Ray Optics and Instrumentation*, 2010(1):867049, 1 2010.

[37] James E. Penner-Hahn. Handbook of X-ray Spectrometry, 2nd ed., Revised and Expanded Edited by René E. Van Grieken (University of Antwerp) and Andrzej A. Markowicz (Vienna, Austria). Marcel Dekker, Inc: New York and Basel. 2002. xvi + 984 pp. $250.00. ISBN 0-8247-0600-5. *Journal of the American Chemical Society*, 124(42):12627–12627, 10 2002.

[38] S. X. Kang, X. Sun, X. Ju, Y. Y. Huang, K. Yao, Z. Q. Wu, and D. C. Xian. Measurement and calculation of escape peak intensities in synchrotron radiation X-ray fluorescence analysis. *Nuclear Instruments and Methods in Physics Research Section B: Beam Interactions with Materials and Atoms*, 192(4):365–369, 6 2002.

[39] Lin Tang, Jie Yu, Jianbin Zhou, Fang Fang, Wenjie Wan, Jianfeng Yao, Songke Yu, and Xianli Liao. A new method for removing false peaks to obtain a precise X-ray spectrum. *Applied Radiation and Isotopes*, 135:171–176, 5 2018.

[40] Francesco Paolo Romano, Claudia Caliri, Paolo Nicotra, Sandra Di Martino, Lighea Pappalardo, Francesca Rizzo, and Hellen Cristine Santos. Real-time elemental imaging of large dimension paintings with a novel mobile macro X-ray fluorescence (MA-XRF) scanning technique. *Journal of Analytical Atomic Spectrometry*, 32(4):773–781, 4 2017.

[41] Bartłomiej Łach, Tomasz Fiutowski, Julio M. del Hoyo-Meléndez, Stefan Koperny, Paulina Krupska-Wolas, Bartosz Mindur, Piotr Wiącek, Paweł M. Wróbel, and Władysław Dąbrowski. Application of a Full-Field macro-XRF imaging spectrometer to non-invasive investigation of elemental composition in three-dimensional artworks. *npj Heritage Science 2025 13:1*, 13(1):1–10, 3 2025.

[42] Matthias Alfeld and Koen Janssens. Strategies for processing mega-pixel X-ray fluorescence hyperspectral data: a case study on a version of Caravaggio's painting Supper at Emmaus. *Journal of Analytical Atomic Spectrometry*, 30(3):777–789, 2 2015.

[43] Matthias Alfeld, Silvia Pedetti, Philippe Martinez, and Philippe Walter. Joint data treatment for Vis–NIR reflectance imaging spectroscopy and XRF imaging acquired in the Theban Necropolis in Egypt by data fusion and t-SNE. *Comptes Rendus Physique*, 19(7):625–635, 11 2018.

[44] V.A. Solé, E. Papillon, M. Cotte, Ph. Walter, and J. Susini. A multiplatform code for the analysis of energy-dispersive X-ray fluorescence spectra. *Spectrochimica Acta Part B: Atomic Spectroscopy*, 62(1):63–68, 1 2007.

[45] C. G. Ryan, J. S. Laird, L. A. Fisher, R. Kirkham, and G. F. Moorhead. Improved Dynamic Analysis method for quantitative PIXE and SXRF element imaging of complex materials. *Nuclear Instruments and Methods in Physics Research Section B: Beam Interactions with Materials and Atoms*, 363:42–47, 11 2015.

[46] E. Clayton and C. G. Ryan. Weighting measures in fitting PIXE spectra. *Nuclear Instruments and Methods in Physics Research Section B: Beam Interactions with Materials and Atoms*, 49(1-4):161–165, 4 1990.

[47] C. G. Ryan and D. N. Jamieson. Dynamic analysis: on-line quantitative PIXE microanalysis and its use in overlap-resolved elemental mapping. *Nuclear Instruments and Methods in Physics Research Section B: Beam Interactions with Materials and Atoms*, 77(1-4):203–214, 5 1993.

[48] Joris Dik, Koen Janssens, Geert Van Der Snickt, Luuk Van Der Loeff, Karen Rickers, and Marine Cotte. Visualization of a lost painting by vincent van gogh using synchrotron radiation based X-ray fluorescence elemental mapping. *Analytical Chemistry*, 80(16):6436–6442, 8 2008.

[49] Paola Ricciardi, Stijn Legrand, Giulia Bertolotti, and Koen Janssens. Macro X-ray fluorescence (MA-XRF) scanning of illuminated manuscript fragments: Potentialities and challenges. *Microchemical Journal*, 124:785–791, 1 2016.

[50] Douglas MacLennan, Laura Llewellyn, John K. Delaney, Kathryn A. Dooley, Catherine Schmidt Patterson, Yvonne Szafran, and Karen Trentelman. Visualizing and measuring gold leaf in fourteenth- and fifteenth-century Italian gold ground paintings using scanning macro X-ray fluorescence spectroscopy: a new tool for advancing art historical research. *Heritage Science*, 7(1):1–9, 12 2019.

[51] Matthias Alfeld, Cecilia Baraldi, Maria Cristina Gamberini, and Philippe Walter. Investigation of the pigment use in the Tomb of the Reliefs and other tombs in the Etruscan Banditaccia Necropolis. *X-Ray Spectrometry*, 48(4):262–273, 7 2019.

[52] David Thurrowgood, David Paterson, Martin D. De Jonge, Robin Kirkham, Saul Thurrowgood, and Daryl L. Howard. A Hidden Portrait by Edgar Degas. *Scientific Reports*, 6(1):1–10, 8 2016.

[53] Matthias Alfeld, Joana Vaz Pedroso, Margriet Van Eikema Hommes, Geert Van Der Snickt, Gwen Tauber, Jorik Blaas, Michael Haschke, Klaus Erler, Joris Dik, and Koen Janssens. A mobile instrument for in situ scanning macro-XRF investigation of historical paintings. *Journal of Analytical Atomic Spectrometry*, 28(5):760–767, 4 2013.

[54] Nica Gutman Rieppi, Beth A. Price, Ken Sutherland, Andrew P. Lins, Richard Newman, Peng Wang, Ting Wang, and Thomas J. Tague. Salvator Mundi: an investigation of the painting's materials and techniques. *Heritage Science*, 8(1):1–12, 12 2020.

[55] Matthias Alfeld, Maud Mulliez, Philippe Martinez, Kevin Cain, Philippe Jockey, and Philippe Walter. The Eye of the Medusa: XRF Imaging Reveals Unknown Traces of Antique Polychromy. *Analytical Chemistry*, 89(3):1493–1500, 2 2017.

[56] Matthias Alfeld, Victor Gonzalez, and Annelies van Loon. Data intrinsic correction for working distance variations in MA-XRF of historical paintings based on the Ar signal. *X-Ray Spectrometry*, 50(4):351–357, 8 2021.

[57] Matthias Alfeld, Philipp Tempel, and Volkert van der Wijk. Cable Robots as Conventional Linear Stage Alternatives for the Investigation of Complex-Shaped Objects via Macroscopic X-ray Fluorescence Imaging. *Quantum Beam Science*, 7(4), 12 2023.

[58] Jacopo Orsilli and Anna Galli. Angle-Dependent XRF Analyses: Pros and Cons of a Novel Technique in the Field of Cultural Heritage. *Sustainability 2024, Vol. 16, Page 1460*, 16(4):1460, 2 2024.

[59] Qiong Xu, Yifan Wang, Xu Zhou, Peiquan Duan, Yong Liu, Jiangtao Gao, Long Wei, Cunfeng Wei, and Liang Qu. Applications of surface adaptive micro X-ray fluorescence scanner in cultural relics. *npj Heritage Science*, 13(1):1–10, 12 2025.